



POLITECNICO
DI TORINO

POLITECNICO DI TORINO

Master Degree course in Nanotechnologies for ICTs

Master Degree Thesis

**Development of hybrid suspended
microchannel resonators for mass sensing in
liquid**

Supervisors

Prof. Carlo RICCIARDI

Dr. Tomás MANZANEQUE GARCIA

Dr. Murali Krishna GHATKESAR

Candidate

Lucia CROCETTO

ACADEMIC YEAR 2022-2023

Acknowledgements

First and foremost, I would like to express my deepest gratitude to my supervisors, Dr. Tomás Manzaneque and Dr. Murali Ghatkesar, for granting me the opportunity to carry out my thesis in their great laboratories. I appreciated their guidance and the time they dedicated to my research. Thanks for creating an environment that promotes scientific growth.

Additionally, I would like to thank my supervisor, Prof. Carlo Ricciardi, who provided insightful suggestions and critiques that were extremely helpful in refining my research methodology and ensuring to follow the right path during this period.

I want to thank Roberto for being a real and incredible friend, who, despite the distance, has always been there for laughter and deep discussions.

I thank my boyfriend, Jacopo, who have stood by me through thick and thin. His belief in me and his constant reassurance during moments of doubt and stress have been crucial in giving me the strength to face the problems.

Most of all, I am eternally grateful to my parents for their unwavering support and love. To my father, thanks for instilling me the value of hard work and perseverance, his work and sacrifices have been my pillar of strength. To my mother, thanks for being my most sincere confidant and my source of inspiration. To my sister, Angela, the funniest person I know, to be my foothold and my point of reference. She showed that in life it is not "the ocean" that matters, but "the fishbowl". To my dog, Tecla, who taught me patience and dedication and gave me unconditional love.

Last but not least, I want to thank my relatives for always supporting me from afar. Thanks for the video calls and the distance workouts.

In conclusion, I am thankful for this learning journey and the people who have been a part of it. This thesis does not stand as a testament to my individual effort, but rather as a symbol of the collective support, encouragement, and belief of the many individuals who have contributed to my journey.

Abstract

Suspended microchannel resonators have proved to be the best candidates for a variety of technological applications requiring accurate measurements in liquid. These devices eliminate the viscous damping by placing the solution inside a hollow resonator surrounded by vacuum, thus reaching sub-femtogram resolution. The main fabrication method of suspended microchannel resonators is standard cleanroom fabrication, which allows to create resonators with excellent mass sensitivity. However, fabrication steps are expensive and complex, and inherently planar, thus limiting three-dimensional design. In this scenario, polymeric resonators printed by two-photon polymerization (TPP) emerged as a valid solution to increase the low prototyping speed and accessibility of silicon-based resonators, but low quality factor and mass sensitivity limit their performance. In this work, a novel fabrication technique based on a hybrid structure has been developed. A single mask cleanroom fabrication process was carried out to create silicon nitride supporting beams. Then, 3D printing by TPP was used to fabricate microfluidic lids. The final silicon chip can be plugged into a stereolithographic microfluidic interface for handling and connecting to the external world. Fabricated devices were mechanically characterised in vacuum by laser Doppler vibrometry before and after the printing process. Damping analysis was conducted to define the main dissipation sources in hybrid devices. Intrinsic losses in the polymer layer were defined as dominant damping sources. A quality factor of 510 at 341 kHz was reached with a $350\ \mu\text{m} \times 50\ \mu\text{m}$ hybrid double-clamped beam. The theoretical mass responsivity and maximum mass resolution of this device were estimated to be 1.84 Hz/pg and 14.75 ag, respectively, which still compete with conventional fabricated SMRs.

Contents

1 Preface	7
2 Literature review: suspended microchannel resonators	9
2.1 Introduction	10
2.2 Resonant beams for mass sensing	11
2.2.1 Fundamentals of nanomechanical resonators	11
2.2.2 Allan deviation	12
2.2.3 Damping forces	12
2.3 Suspended micro/nanochannel resonators	14
2.3.1 Energy dissipation: effect of the buried liquid	14
2.4 Fabrication methods of SMR	16
2.4.1 Bulk micro-machining	17
2.4.2 Two-photon polymerization	18
2.5 Hybrid suspended microchannel resonator	19
2.5.1 Material analysis for the polymeric layer	20
2.5.2 Experiments	20
2.6 Research aim	20
2.6.1 Research questions	20
2.6.2 Approach	20
2.6.3 Project organization	20
Bibliography	23
3 Hybrid suspended microchannel resonator for mass detection in liquid	27
3.1 Introduction	28
3.2 Materials and methods	29
3.2.1 Cleanroom microfabrication	29
3.2.2 Two photon polymerization	30
3.2.3 Stereolithography	31
3.2.4 Pillar fabrication for Young's modulus and adhesion force measurements	32
3.2.5 Resonant frequency measurements	32
3.3 Results	33
3.3.1 Cleanroom fabricated devices	33
3.3.2 TPP-printed hollowed structure	33

3.3.3	Mechanical characterization of IP-Dip pillars	35
3.3.4	Resonant frequency measurements	36
3.3.5	Estimated mass responsivity and sensitivity	39
3.4	Discussion	40
3.4.1	Origins of multiple resonance peaks after metal coating	40
3.4.2	Energy dissipation in hybrid devices	40
3.4.3	Effects of UV-light exposure	42
3.4.4	Comparison with the state of the art	42
3.5	Conclusion	42
	Bibliography	43
4	Energy dissipation analysis in hybrid multilayer double-clamped microbeams	47
4.1	Introduction	48
4.2	Fabrication	49
4.3	Experimental setup	49
4.4	Results and discussion	49
4.4.1	Metal coated SiN beams	49
4.4.2	Beams with IP-Dip layer	50
4.5	Conclusions	52
	Bibliography	54
5	Conclusion	57
A	FEM simulation of the hybrid device	59
A.1	Stiffness of the silicon nitride cantilever	59
A.2	Resonant frequency of the hybrid device	61
A.2.1	Frequency study of multilayered clamped beams	61
A.2.2	Frequency study of hollowed structures	62
A.3	Mass responsivity of empty beams in vacuum	64
A.4	Flow-induced deformation	65
A.5	Resonant frequency dependence on liquid density	68
A.6	Energy dissipation in water-filled resonators	69
A.6.1	Theoretical analysis: incompressible and compressible flow	69
A.6.2	FEM simulations	71
A.7	Intrinsic dissipation in multilayer resonators	72
B	Fabrication process	75
B.1	Photolithographic masks	75
B.2	Cleanroom steps for silicon nitride structures	77
B.2.1	Low-stress LPCVD of silicon nitride	78
B.2.2	Reactive ion etching of silicon nitride	81
B.2.3	KOH etching for beam release	81
B.2.4	Aluminum-Silicon(1%) sputtering and wafer cleaving	82
B.3	3D printing of IP-Dip channels via two-photon polymerization	82
B.3.1	TPP-printing on SiN beams	83

C	Characterisation	85
C.1	Mechanical characterization	85
C.1.1	Young's modulus of IP-Dip	85
C.1.2	Adhesion force between polymer and AlSi(1%) surface	86
C.2	Frequency study: resonant frequency and Q-factor measurements	86
	Bibliography	91

Acronyms

DLW	Direct Laser Writing
EKL	Else Kooi Lab
FEM	Finite Element Method
LPCVD	Low-Pressure Chemical Vapor Deposition
PME	Precision and Microsystem Engineering
PR	Photoresist
RIE	Reactive Ion Etching
SLA	Stereolithography
SMR	Suspended Microchannel Resonator
SNR	Suspended Nanochannel Resonator
TPA	Two-Photon Absorption
TPP	Two-Photon Polymerization
UV	Ultraviolet

Chapter 1

Preface

The MSc thesis project was carried out in the department of Electronic Instrumentation (EI) in collaboration with the department of Precision and Microsystems Engineering (PME) at the Delft University of Technology, The Netherlands. The work consisted of the fabrication and study of suspended microchannel resonators (SNR) for weighting nanoparticles in liquid realised as hybrid structures made of silicon nitride and polymer. Device simulation, fabrication, and characterisation were preceded by a literature review. It was indeed necessary to understand the working principle of the SNRs, the state of the art of this technology and the issues of systems previously developed by the laboratory to design and realise a new device.

In this regard, a literature survey report is presented in chapter 2. It contains a study about resonant cantilevers for mass sensing in liquid and, in particular, suspended micro- and nano-channel resonators (SM/NR), and an analysis of quality factor and measurement noise (Allan deviation). Added to this is the review of the main fabrication methods previously used by the laboratory to realise SMRs, i.e., surface micromachining and two-photon polymerization (TPP). The chapter ends with a description of the hybrid resonating structure developed during this project (sec. 2.5), highlighting its advantages over previous fabricated devices and its possible limitations.

Chapters 3 and 4 deal with the materials and methods involved in manufacturing, performed experiments and achievements.

Details about the mechanical properties of the new device and its static and dynamic behaviour are covered in annex A, where FEM simulations are presented. In particular, the annex includes: the study of microbeam stiffness and resonant frequency with and without the IP-Dip layer; the derivation of the mass responsivity without liquid inside the channel through the analysis of the resonant frequency with a variable proof mass; and, finally, the impact of flow rate, liquid density and viscosity on the device in both static and dynamic case.

In annex B the fabrication process carried out in Else Kooi Lab (EKL) and Precision and Microsystems Engineering (PME) laboratory is presented. It includes the realisation of supporting silicon nitride U-shaped cantilevers and bridges with typical semiconductor processes and the 3D printing of polymeric layers via TPP.

To conclude, the mechanical characterization and the frequency study of the devices are presented in annex C.1. It contains an analysis of the mechanical properties of the IP-Dip polymer, i.e., Young's modulus, and adhesion to the substrate, and the measurement of resonant frequency

and quality factor of the beams with and without the polymer lid.

Chapter 2

Literature review: suspended microchannel resonators

Literature review: suspended microchannel resonators

Suspended microchannel resonators (SMRs) are innovative resonant structures with integrated fluidic channels, enabling highly sensitive mass detection in liquid environments. A key concept related to SMRs is the challenge associated with the fabrication of such a kind of micro/nanomechanical resonators. The presence of a microfluidic channel inside the resonating structure complicates the manufacture of the device, and standard Si-based fabrication processes become too complex and expensive. In this scenario, hybrid SMRs combining silicon nitride support beams with polymeric lids offer a promising solution to enhance performance and simplify fabrication processes. A comprehensive review of microbeam resonators focusing on fabrication methods and performance is presented in this work. The impact of mechanical parameters of materials and fluid dynamics on energy dissipation is analysed to address crucial questions about the dominant damping sources in hybrid resonators. The paper outlines a systematic approach, including simulations, fabrication, and characterization, providing valuable insights into the design and optimization of SMRs for diverse applications in mass sensing and biosensing.

Index terms – Suspended microchannel resonator, Resonant frequency, Damping, Quality factor, Allan deviation, Two-photon polymerization, Bulk micro-machining.

2.1 Introduction

Cell mechanical properties, such as mass or stiffness, and their significant variations during the onset or progression of a disease proved to be a useful biomarker for diagnostic and diagnosis of several pathologies [1, 2]. These findings have enabled an increase in interest in micro- and nano-electromechanical systems (M/NEMS) for life-science applications over the past two decades [3]. Continuous advances in the field of micro- and nano-technologies allow to fabricate extremely small sensors (of the size of some biomolecules) that guarantee remarkable mass resolution and highly sensitive mechanical response [4, 5].

Regarding the mass sensing of cells, this is commonly performed with resonant cantilevers or bridges [6, 7, 8], which are dynamic mechanical devices that vibrate close to their resonance frequency. These sensors achieve excellent performances in gaseous environments, where they can reach extremely high quality factors. Nevertheless, the same is not true in liquid,

where they exhibit over-damped responses limiting their mass resolution [9]. A solution to overcome the drawbacks of these resonant cantilevers was developed by Burg and Manalis in 2003: a hollow resonant structure with an embedded microfluidic channel, the suspended microchannel resonator (SMR) [10]. Since the analysed liquid flows inside the resonator, viscous damping is eliminated, and mass loading is reduced. Furthermore, real-time analysis is made possible while the entire apparatus can be kept dry, preserving its mechanical performance. High quality factors (up to 15000) and excellent mass sensitivities (1 attogram) in 1 kHz bandwidth have been demonstrated [11].

Fundamentals of cantilever-like mass sensing methods will be covered in section 2.2 along with the basis and the effects of damping phenomena. Characteristics of the suspended microchannel resonators will be reviewed in section 2.3, while section 2.4 will discuss different fabrication methods of the SMRs. Finally, the novel hybrid structure will be presented in section 2.5.

2.2 Resonant beams for mass sensing

As transducers, microcantilevers and microbridges (fig. 2.1) exploit their flexibility or elasticity to produce a quantifiable change in response to external stimuli. The reaction of the cantilever to the stimulus is expressed in terms of mechanical stress, which generates a variation of one of its mechanical or electrical properties. The most typical metrics for this change are the cantilever's resistivity, angular deflection, or natural resonant frequency. In order to measure one of these properties, the cantilever can be operated in either static mode or dynamic mode.

When operated statically, the cantilever is in stationary state. Any displacement of the cantilever due to a load or intrinsic stress generated on or within the cantilever is measured. Generally, the transducer's surface is functionalised with a probe coating, chemically sensitive to specific molecules. As the molecules to be analysed are adsorbed by the coating, the surface stress or an overall mass variation in the transducer leads to cantilever displacement. This displacement is quantified to obtain the unknown mass of the analyte. The bending of the cantilever is measured primarily by means of a change in the angular deflection or a change in resistance using a piezoresistive material embedded as a structured layer within the cantilever.

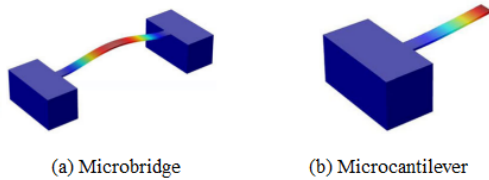


Figure 2.1. Double (a) and single (b) clamped resonator microstructures.

In dynamic mode, the measurement is performed by monitoring any change in the natural resonant frequency. The structure is externally excited at its resonant frequency by piezoelectric, magnetic, or electrostatic actuation. Any change in the physical characteristics of the cantilever - such as its stiffness or mass - changes its natural frequency. The displacement of the structure is measured with optical or electrical detection techniques.

The dynamic mass sensing method will be the main focus of this study.

2.2.1 Fundamentals of nanomechanical resonators

The resonance frequency $f_{R,n}$ of an oscillating cantilever at an arbitrary mode number n in vacuum is given by the equation 2.1 [12].

$$f_{R,n} = \frac{\alpha_n^2}{2\pi} \sqrt{\frac{YI}{ml^3}} \quad (2.1)$$

where Y is the elastic modulus of the material, I is the moment of inertia of the cantilever, l is its length, b its width, h its thickness, m its mass and α is a constant with values: $\alpha_1 = 1.875$, $\alpha_2 = 4.694$, $\alpha_n = \pi(n - 0.5)$ [13]. The constant n refers to the mode number, and, in particular, $n = 1$ in the case of the fundamental frequency.

By differentiating $f_{R,n}$ of equation 2.1 with respect to m , it is possible to derive the relation between a change in mass Δm and a change in resonance frequency $\Delta f_{R,n}$ [14, 15]. A linear approximation for added mass is obtained by assuming $m \gg \Delta m$ (equation 2.2).

$$\Delta m \approx -2m_{eff} \frac{\Delta f_{R,n}}{f_{R,n}} \quad (2.2)$$

where m_{eff} is the effective mass of the resonating beam, defined as $m/4$ and $0.3864m$ for the fundamental mode of single- and double-clamped beams, respectively [16].

The mass responsivity R can be derived from equation 2.2. It represents the change of resonance frequency $\Delta f_{R,n}$ as a result of

changes in mass Δm and is an indicator of the resonator sensitivity. Equation 2.3 describes the mass responsivity as a function of the resonant frequency [14].

$$R = \frac{\partial f_{R,n}}{\partial m} \approx -\frac{f_{R,n}}{2m_{eff}} \quad (2.3)$$

Assuming a constant stiffness of the cantilever, it can be observed that the higher the frequency the better the mass sensitivity.

Another important parameter is the mass resolution δm , which indicates the minimum mass that can be detected by the sensor. This parameter is given by the ratio between the frequency noise δf (standard deviation of frequency fluctuations) and the responsivity R (equation 2.4) [17].

$$\delta m \approx -2m_{eff} \frac{\delta f}{f_{R,n}} \approx -2m_{eff} \frac{1}{Q} \frac{Noise}{Signal} \quad (2.4)$$

From equation 2.4 it is evident that, in order to maximise sensing performances, a large quality factor Q and signal-to-noise ratio are needed.

The quality factor Q is a fundamental performance indicator for resonators. It is obtained by the sharpness of the amplitude peak at a resonance frequency in Bode plots and can be defined as the ratio between energy stored E and energy dissipated ΔE by the system within one operating cycle at resonance. Its general definition is shown in equation 2.5.

$$Q = 2\pi \frac{E}{\Delta E} \quad (2.5)$$

The dissipation phenomenon is dominated by damping. As clear from the equation 2.5, the lower the damping the higher the quality factor of the system.

2.2.2 Allan deviation

An important indicator of the potential sensitivity that the resonator can have as a sensor is

the frequency stability. It can be investigated by the measure of the Allan deviation $\sigma_y(\tau)$. Allan deviation is a function of the sample period τ , and it is generally defined by the equation 2.6 [18].

$$\sigma_y(\tau) = \sqrt{\sigma_y^2(\tau)} \approx \sqrt{\frac{1}{2(N-1)} \sum_{k=2}^N \left(\frac{f_k - f_{k-1}}{f_0}\right)^2} \quad (2.6)$$

where f_k is the average measured frequency in the k -time interval τ within a total of N intervals, and f_0 is the mean oscillation frequency calculated over the entire duration of the noise measurement. A system with good stability over the measured period τ is characterised by a low Allan deviation.

Mass resolution also depends on the frequency noise δf , which is typically quantified by the Allan deviation. So the equation 2.4 can be simplified into equation 2.7 by substituting $\frac{\delta f}{f_{R,n}}$ with the Allan deviation.

$$\delta m \approx -2m_{eff} \frac{\delta f}{f_{R,n}} \approx -2m_{eff} \sigma_y(\tau) \quad (2.7)$$

2.2.3 Damping forces

The quality factor Q of a resonator is inversely proportional to the energy dissipated by damping. It can be theoretically estimated using equation 2.8 [19], where each term of the sum is the inverted quality factors of a specific damping source.

$$\frac{1}{Q} = \frac{1}{Q_{medium}} + \frac{1}{Q_{sup}} + \frac{1}{Q_{TED}} + \frac{1}{Q_{others}} \quad (2.8)$$

where Q_{medium} is the air damping Q-factor, Q_{sup} is the support loss Q-factor, and Q_{TED} is the thermoelastic dissipation (TED) Q-factor. Q-factor of other energy losses (e.g. bulk loss, surface loss, PZT loss) is denoted by Q_{others} .

Medium interaction damping is related to the gaseous or fluidic media surrounding the oscillating beam. Support damping is caused

by the energy dissipated at the junction between the beam and the substrate. Thermoelastic loss originates from the thermal energy dissipated by the mechanical resonator, through irreversible heat conduction accompanying its elastic vibrations. Other damping sources are caused by internal friction, electrostatic charges, and magnetic fields.

The damping component due to the interaction of the cantilever with the medium is different when operating in a liquid or gaseous environment. When the cantilever oscillates in a viscous medium, a hydrodynamic force generated by the squeezed fluid opposes the motion of the cantilever [20]. This force is critical in liquid, where the performance of the beam in dynamic mode strongly depends on its size and shape, but it is heavily reduced in gas. In liquid conditions, quality factors close to unity have been reported at the fundamental resonant mode of microcantilevers, while higher quality factors (up to 30) have been measured for increasing resonant modes [21, 22]. The effects of the medium damping also depend on the pressure. In particular, vacuum pressure allows the resonator to be operated with minimal gas damping.

Support or clamping damping arises from the frictional interaction at the beam-clamp interface. The transfer of vibrational kinetic energy from the beam to the supporting substrate generates energy loss, which is strongly dependent on the type of beam-support contact. In particular, the greater the freedom of movement of the cantilever at the anchors, the lower the effects of the support loss [23]. It can be estimated using two-dimensional elastic wave theory with the assumption that cantilever thickness t is much smaller than the wavelength of the elastic wave propagation [24] (see equation 2.9).

$$Q_{sup} = C \cdot \frac{L^3}{t^3} \quad (2.9)$$

where L is the cantilever length and C is a constant that ranges from 2.081 to near 0, depending on resonant mode and increasing with the mode number.

Thermoeleastic damping is due to the temperature gradient generated by the repeated state of tension and compression in a vibrating beam [25], and it can be expressed approximately by equation 2.10 [19].

$$Q_{TED} = \frac{C_V}{Y\alpha^2 T_0} \frac{1 + (\omega\tau)^2}{\omega\tau} \quad (2.10)$$

where Y is the elastic modulus of the material, α is the thermal expansion coefficient, T_0 is the nominal equilibrium temperature, C_V is the heat capacity at constant volume, ω is the angular resonant frequency, and τ is the relaxation time.

The principal loss mechanism in a resonant cantilever included in other damping sources is intrinsic or material damping. Material damping arises from the atomic arrangement of the beam as well as its impurities, and it is linked to material properties, fabrication processes, and temperature. As material damping occurs at the molecular level, it is a type of microscopic damping. There are two different loss mechanisms falling within the intrinsic damping: friction losses and phonon-phonon interaction losses. Phonon-phonon interactions only affect crystalline materials, and are due to atomic interactions with the strain field; friction losses originate from irreversible atomic motions during vibration. The sources of this atomic motion can be defect dislocations in crystalline materials, grain boundary slipping in metals, phase boundary slipping in bilayer structures, or molecular chain movement in amorphous materials [15]. The internal friction Q_{int} can be analytically expressed by equation 2.11 [15].

$$Q_{int} = \frac{\sqrt{Y_u Y_r}}{\Delta Y} \frac{1 + (\omega\tau_{int})^2}{\omega\tau_{int}} = \Delta \frac{1 + (\omega\tau_{int})^2}{\omega\tau_{int}} \quad (2.11)$$

where Δ is the so-called relaxation strength and depends on the relaxed Young's modulus Y_r and the unrelaxed Young's modulus $Y_u=Y_r+\Delta Y$, ω is the angular frequency and τ_{int} is the relaxation rate of the material, which is a temperature-dependent parameter. The value of τ_{int} can be obtained by means of the geometrical average of the relaxation time at constant strain τ_ϵ and the relaxation time at constant stress τ_σ (see equation 2.12) [15].

$$\tau_{int} = \sqrt{\tau_\epsilon \tau_\sigma} \quad (2.12)$$

Significant damping occurs when the angular frequency and the inverse of the relaxation rate are in the same order of magnitude.

2.3 Suspended micro/nanochannel resonators

Micro- and nanomechanical resonators are characterised by great mass sensitivity when operating in vacuum thanks to low damping mechanisms in gaseous environments. In these conditions, their quality factor achieves values up to 100'000, enabling the detection of individual analytes down to single molecules. However, their performances are drastically reduced in liquid environment due to the overdamped response caused by viscous loss.

In 2003 Scott Manalis' group developed a new promising device for mass sensing in liquid: a mechanical suspended resonant structure with an integrated fluidic channel [10], shown in figure 2.2(a). The device, called suspended microchannel resonator (SMR) is oscillated at its resonant frequency in a dry environment by electrostatic forces or by a piezoelectric actuator integrated into the chip. Since the fluid to be analyzed flows inside the resonator, viscous damping is almost completely eliminated and mass loading is reduced [17]. The buoyant mass of the particle temporarily modifies the cantilever's resonant frequency as it passes

through the embedded channel (fig. 2.2(b) and (c)) and this change is measured to determine the particle mass.

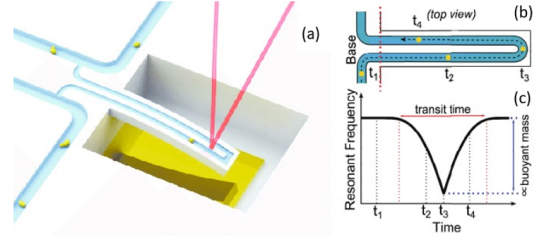


Figure 2.2. (a) Schematic of a cantilever-shaped SMR [26]. (b) Top view of the SMR with a particle at four different positions in the device. (c) Time-variation of the resonant frequency with the position of the particle through the channel. The signal amplitude is proportional to the buoyant mass of the particle [26].

The last advances in SMR technology opened up the unique possibility to weigh single cells, e.g. bacteria, yeast or mammalian cells with femtogram precision in solution [26]. This brings the advantage of studying characteristics and changes of biological components at the single particle level, creating new perspectives on how to explore and resolve biological and clinical issues.

2.3.1 Energy dissipation: effect of the buried liquid

The presence of an embedded microfluidic channel inside the resonating device strongly impacts its behaviour as a function of liquid density, fluid viscosity, and mode number. In addition, the positioning of the fluidic channel in the beam cross-section influences the flow dynamics and hence the energy dissipation.

In general, although the device can be operated in vacuum, it still experiences moderate damping due to the liquid flowing inside the integrated channel. This damping typically rises with increasing mode number, as opposed to traditional cantilevers operated in liquid [27].

The damping mechanism due to the presence of the fluid in the channel can be expressed as a quality factor, which can be derived under the following geometrical assumptions:

- Cantilever length is much larger than its width and thickness;
- Channel thickness is much smaller than the channel width and its length is equal to the length of the cantilever;
- The amplitude of oscillation is much smaller than the cantilever length so that linear motion and flow are ensured.

With these assumptions the Q-factor can be obtained by the equation 2.13 [27].

$$Q_{liquid,n} = F_Q(\beta_n) \frac{\rho_{average}}{\rho_{liquid}} \frac{h}{h_c} \frac{w}{w_c} \frac{l^2}{h_c^2} \quad (2.13)$$

where n is the resonant mode number, $\rho_{average}$ is the average mass density of the whole cantilever with the liquid, ρ_{liquid} is the mass density of the fluid, h is the height, w the width and l the length. These quantities are related to the internal channel when indicated with the subscript c . The parameter F_Q is the normalised quality factor and β_n is commonly referred to as Reynold's number, indicating the fluid inertia. Its behaviour not only depends on the type of fluid flowing in the SMR, but it is also closely related to the relative position of the embedded channel with respect to the neutral axis of the beam.

On-axis channel placement

As a first analysis, the simplest case of on-axis channel placement should be considered.

For the first three resonant modes, the behaviour of $F_Q(\beta_n)$ as a function of the Reynold's number β_n is shown in fig. 2.3. The functional $F_Q(\beta_n)$ is described in details by the equation 2.14 [15].

$$F_Q(\beta_n) \approx \frac{38.73}{\beta_n} + 0.1521\sqrt{\beta_n} \quad (2.14)$$

where β_n can be expressed by equation 2.15 [15].

$$\beta_n = \frac{\rho_{liquid} h_c^2}{\mu} \omega \quad (2.15)$$

where ω is the angular velocity of the cantilever vibration and μ is the fluid viscosity.

From figure 2.3 it is clear that the quality factor due to the presence of the liquid inside the embedded channel is not a monotonic function of the Reynold's number, and hence of the fluid density and viscosity.

For large Reynold's numbers, the fluidic behaviour is governed by its inertia, and the behaviour of the beam is more logical: viscous boundary layers produced by this inertial flow cause energy loss [27]. Hence, a small quality factor is produced by increasing the fluid viscosity or reducing the liquid density (decreasing the Reynold's number). An opposite behaviour is observed for small Reynold's numbers: the influence of fluid inertia vanishes and the fluid behaves like a rigid-body that does not produce any viscous boundary layer [27]. This means that an increasing fluid viscosity or a decreasing density (decreasing Reynold's number) results in a higher quality factor.

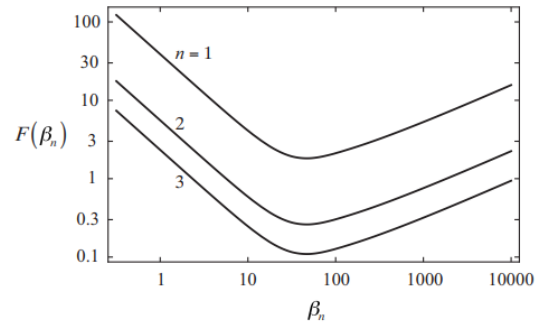


Figure 2.3. Plot of normalized quality factor $F_Q(\beta_n)$ as a function of β_n for the first three modes of vibration, $n=1, 2, 3$ [27].

Off-axis channel placement

In the case of off-axis channel placement, the relationship is more complicated: the beam vibrations cause an axial strain in the channel, which in turn yields a pumping mechanism of the fluid into and out of the reservoir. As a consequence, the energy dissipation increases, thus reducing the quality factor. The latter also shows a striking non-monotonic dependence on Reynold's number and varies dramatically with mode number and distance of the channel from the neutral axis [27]. This dependence is shown in fig. 2.4, representing the behaviour of $F_Q(\beta_n)$ as a function of the Reynold's number β_n for different off-axis displacements.

From the graph (fig. 2.4) it is evident that an increase in the channel distance from the neutral axis of the beam causes a significant decrease of the normalized Q-factor, especially in the range $\beta < 10$. This means that tuning the off-axis channel placement will cause a change of orders of magnitude in $Q_{liquid,n}$.

Another parameter that affects the Q-factor in case of off-axis placement is the Poisson's ratio ν of the beam [28]. The dependence of $F_Q(\beta_n)$ on ν can be seen in fig. 2.5, where it is

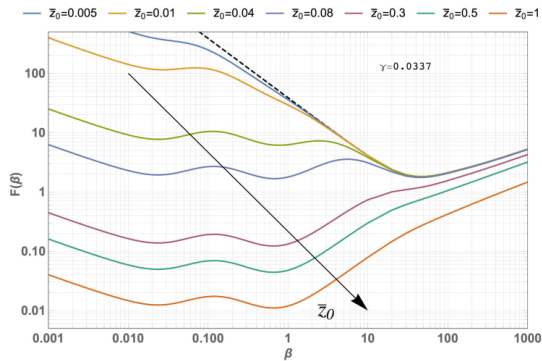


Figure 2.4. Quality factor $F_Q(\beta_n)$ for several \bar{z}_0 , with normalized acoustic wavenumber $\gamma=0.0337$; black dashed line is the on-axis case [29]. The off-axis placements \bar{z}_0 is defined as the displacement of the channel with respect to the neutral axis normalized to the channel height.

clear that increasing the Poisson's ratio produces an improvement of the quality factor.

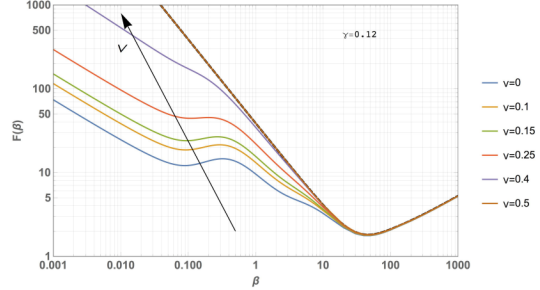


Figure 2.5. Quality factor $F_Q(\beta_n)$ for several Poisson's ratio ν , with normalized acoustic wavenumber $\gamma=0.12$ and $\bar{z}_0=0.06$; black dashed line is the on-axis case [29].

The effect of Poisson's ratio can be translated into an equivalent off-axis channel placement: $Z_{eff} \approx (1 - 2\sigma)Z_{off-axis}$.

Furthermore, it provides an additional degree of freedom that can be used to modify the energy dissipation in SMRs. Since decreasing Z_{eff} reduces the effects of any off-axis flow, the use of materials with high ν is highly recommended to improve the Q-factor, and thus the sensitivity of frequency shift measurements.

2.4 Fabrication methods of SMR

SMR fabrication can be a complex and expensive process, since the device must meet the requirements of mechanics, microfluidics and, in the case of integrated transduction, electronics [17]. Materials and geometrical dimensions must be suitable for both sensor functionality and manufacture. Moreover, the choice of the resonator material should take into account factors like thermal constraints, residual stress, and fabrication cost along with features like biocompatibility, chemical stability, and hydrophilicity [17].

Typically, SMRs are made with silicon-based materials using semiconductor manufacturing processes. In this case, the main approaches can be classified in two categories:

- **Process requiring sacrificial materials:** the fabrication involves the deposition of a sacrificial material for microchannel definition that enables precise control over channel geometry and size [30]. However, this approach is costly and extremely complex.
- **Process not requiring a sacrificial material:** the embedded channel is obtained without sacrificial layers, by means of alternative techniques. Examples might be fusion bonding of two SOI wafers [31, 32], previously etched to define the microfluidic channel cavity, or silicon resonator with self-assembled buried cavities [33]. This technique can be less complex than the process involving sacrificial layers, but equally expensive.

In both cases, the definition of the microfluidic channel within the resonator represents one of the most challenging steps of the fabrication, which remains difficult and costly. In addition, semiconductor manufacturing processes limit geometrical freedom, material choice and prototyping speed.

A viable alternative could be to realise a 3D printed cantilever by using two-photon polymerisation (TPP) [34, 35]. This technique allows rapid prototyping in a 3D design space and reduces fabrication costs. However, polymer cantilevers are characterised by higher intrinsic damping and lower Young's modulus compared to silicon-based materials (below 5 GP), resulting in lower sensitivity.

Both bulk micro-machining and two-photon polymerization were used for prototypes previously developed by the MNE and EI group of TUDelft. With the first technique, a

silicon dioxide hollowed cantilever has been realised. It was able to measure a mass of 21.2 fg, equivalent to a gold nanoparticle of 130 nm diameter [36]. A second device was made by two-photon polymerization (TPP), reaching a theoretical mass sensitivity of 175 fg, which corresponds to the dimensions of an E.Coli bacterium [37]. However, although the first solution allows to reach excellent mass sensitivity, it turned out to be too expensive and complex. The second one, instead, guarantees low cost and high accessibility, but to the detriment of quality factor and mass sensitivity.

A detailed analysis of the two fabrication processes and the obtained results will be covered in the following two sections.

2.4.1 Bulk micro-machining

The device realised by bulk micro-machining is a silicon dioxide U-shaped suspended microfluidic channel (fig. 2.6).

The fabrication process relies on the bonding of two silicon wafers, previously etched to create the microfluidic channel in one wafer and the inlet and outlet reservoirs in the other. Thermal oxidation of the internal cavities defines the final device. Then the SiO₂ cantilever is released by etching the external Si substrate in KOH. In order to connect the channel to the outside world, the inlet and the outlet of the device are connected to a 3D-printed interface.

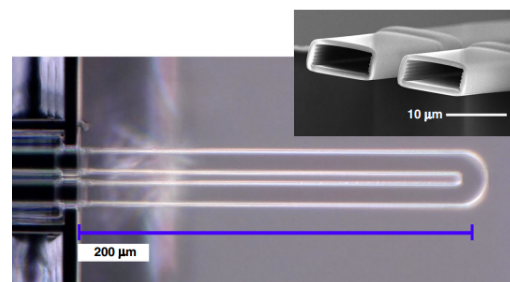


Figure 2.6. *Optical microscope top-view image of the U-shaped silicon dioxide SMR. A scanning electron microscope image of the cantilever cross-section is shown in the inset [36].*

The flow chart of the fabrication process is shown in fig. 2.7.

All experiments to determine frequency stability and mass detection limit were carried out in vacuum. A minimum mass of 377 ag, equivalent to a 34 nm diameter gold nanoparticle, was measured in water-filled cantilever [36], thus demonstrating the device's capability of detecting attograms of buoyant mass.

Although this SiO₂ SMR proved to reach excellent mass resolution and detection limit, performing continuous measurements with high throughput, the fabrication process is time-consuming and costly. Creating the embedded channel requires extra steps with sacrificial material, and makes the whole fabrication process challenging. Moreover, the device is developed in a 2.5D design space with low prototyping speed, due to the design-specific masks.

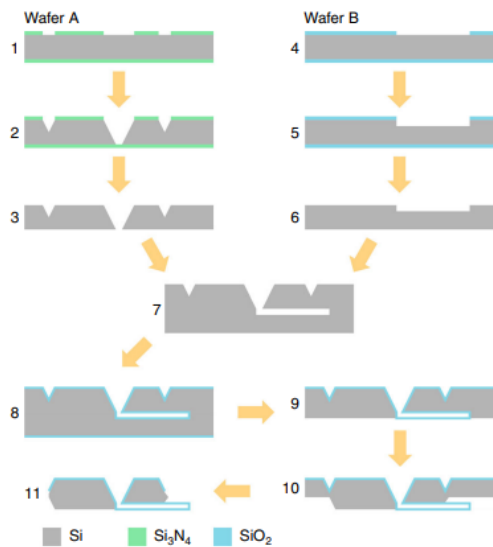


Figure 2.7. Flowchart of the fabrication process [36]. (1) LPCVD of silicon nitride and patterning by RIE. (2) Wet etching of Si to create the fluid reservoirs and release trenches. (3) Removal of silicon nitride. (4) Thermal oxidation of Si and patterning by RIE. (5) Etching of Si by RIE to create the channel. (6) Removal of silicon dioxide. (7) Wafer bonding. (8) Thermal oxidation of the channel cavity. (9) Backside RIE. (10) Release of the cantilever by KOH etching. (11) Manual release of the chips.

2.4.2 Two-photon polymerization

A second device was made with two-photon polymerization. This technique allows to simplify the fabrication of the device, eliminating the complex steps to create the channel. Furthermore, rapid prototyping is possible thanks to the 3D design space.

TPP is a nonlinear optical process based on two-photon absorption (TPA). In TPA, a molecule is excited from its ground state to a higher energy level by the simultaneous absorption of two photons with different or equal frequencies [38]. This molecular excitation is exploited in TPP, where a focused high-energy laser triggers the two-photon absorption in a highly localized region of the photosensitive material. Free radicals are released in the resin and 3D microstructures are created via photochemical reactions by moving the focal point of the laser. The photosensitive resin is a transparent material, highly absorptive in the UV range and normally transparent in the IR region.

TPP has several advantages over other conventional microfabrication techniques: the nonlinear response of the photoresists guarantees high resolution (up to tens of nanometers), the method creates complex 3D structures directly from a CAD drawing and allows the fabrication of high-aspect-ratio microstructures. However, the number of commercially available materials is limited, and they are also characterised by low Young's modulus and high friction damping. This makes them unsuitable for applications that require high quality factor and frequency stability.

The resonator realised by TPP is a double-clamped beam with an embedded channel made of IP-S polymer, shown in fig.2.8. The structures were printed on 3DM fluidic interfaces for easy fluidic connection. SMRs were suspended by domes, providing a microfluidic connection between the fluidic interface and the hollow bridge.

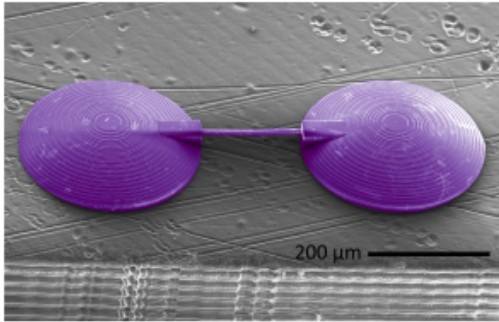


Figure 2.8. Electron microscopy image of suspended microchannel resonator with domes (purple) for microfluidic connection to the interface [37].

In terms of mass resolution, the device is able to reach a theoretical mass sensitivity of 175 fg. This value is limited by its low quality factor ($Q \sim 1000$). Moreover, due to the leaking and clogging problems, the mass sensing capabilities of the water-filled device have not been proved.

The mass density of IP-S is significantly lower than that of the materials typically used for SMRs, e.g., silicon, silicon dioxide and silicon nitride, giving the devices a significant improvement in mass resolution when operating in lower quality factor conditions dominated by medium interaction damping.

2.5 Hybrid suspended microchannel resonator

The limitations and the advantages of SiO_2 cantilever and polymeric beams realised in the laboratory were taken into account to develop a new resonating structure. This SMR consists of two separate parts: a supporting silicon nitride beam realised by bulk micro-machining and a polymer lid with a patterned channel fabricated by TPP. A schematic view of the device is shown in fig. 2.9.

The hybrid structure allows to reduce and simplify the fabrication steps in cleanroom, since the channel, which is the most challenging part of the device, is fabricated via TPP. At

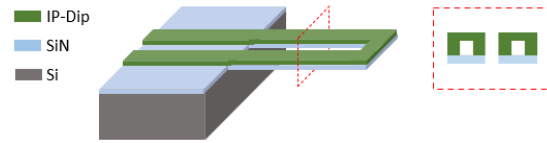


Figure 2.9. Schematic of the hybrid cantilever-shaped suspended microchannel resonator.

the same time, it guarantees a higher quality factor than that of the polymeric resonator, thanks to the presence of the SiN beam. Choosing silicon nitride as supporting material also reduces the possibility of cracks due to intrinsic stress with respect to the SiO_2 formerly used and limits the dissipation effect due to the off-axis flow thanks to its higher Poisson's ratio ($\nu = 0.27$ [39]).

However, the polymeric lid also has drawbacks. First of all, the polymer is a damping source for the device, and this entails a reduction of the quality factor. In the second place, the position of the fluid, and thus of the buoyant mass to be detected, does not coincide with the neutral axis of the silicon nitride beam, hence affecting the device's sensitivity. Added to this is the problem of the adhesion between the two layers, which has to be guaranteed when a liquid flows inside the channel. On this premise, an analysis of Young's modulus and adhesion to the substrate of the different available polymers will be carried out in order to choose the most promising resin. Then, the adhesion forces to the pristine and treated substrate will be measured for the chosen material.

Further analyses will be carried out to study the frequency behaviour of the hybrid device. In fact, one of the effects produced by the polymeric layer on the silicon nitride beam is the resonant frequency variation. The distributed mass and the additional stress due to the lid change the resonant frequency and the mass responsivity of the device. These variations will be analysed by means of theoretical calculations and FEM simulations (see annex A).

2.5.1 Material analysis for the polymeric layer

Resins considered for creating the polymeric lid with the channels are listed in table 2.1. Here are also indicated some material parameters such as Young's modulus, mass density, resolution, and adhesion to silicon or silicon-based materials.

The adhesion to the substrate is a qualitative parameter and can be improved by means of silianization of the surface before TPP in the case of IP-Dip and IP-S resin [40, 41, 42].

The resin must ensure low damping, which translates into a high resonator quality factor, and a good resolution, in order to reduce the channel cross-section. This results in high Young's modulus, low mass density and small minimum features. Based on this, the most suitable material is IP-Dip.

2.5.2 Experiments

Once the realisation of the hybrid resonator is completed, a series of experiments will be conducted to investigate its performance. These experiments will take place within a temperature-controlled vacuum chamber, providing an ideal testing environment. A piezoelectric actuator will be utilized to excite the resonator, and the deflection of the beam will be optically detected using a laser Doppler vibrometer. Amplitude and frequency data will be processed to derive eigenfrequencies and quality factor for cantilevers of different sizes.

All experiments will be performed in high vacuum (5×10^{-4} mbar) to eliminate the effect of the medium damping on the Q-factor.

2.6 Research aim

2.6.1 Research questions

Considering the laboratory's previous achievements with IP-S and SiO₂ SMRs, the aim of this

project is expressed by the following question:

- **What is the performance of the hybrid SMR in terms of mass limit detection and resolution?**

2.6.2 Approach

In order to answer the research question, two experiments and COMSOL simulations must be performed.

A first experiment will be conducted to achieve a baseline and compare the performance of two types of devices, i.e., cantilever and bridge, with those of the polymer and SiO₂ resonators. The performance will be evaluated by means of the quality factor, measured at room temperature and without fluid inside the channel.

A second experiment will be carried out to study the damping sources. In particular, the damping effects caused by the introduction of the IP-Dip lid will be considered.

In order to determine the effect of fluid inside the integrated channel on the resonance frequency and quality factor of the device, COMSOL simulations will be performed. Several liquids will be injected into the channel, and the quality factor will be calculated for different resonant modes.

Finally, the mass limit and resolution will be determined by combining the results obtained from simulations and experiments.

2.6.3 Project organization

The following four milestones are established to monitor development and results during the research project:

- **Simulations on hybrid SMRs:** study of the resonant frequency and mass responsiveness in clamped and clamped-clamped resonating beams with and without liquid inside the embedded channel; analysis of

the dissipation caused by polymer lid and off-axis channel placement.

- **Fabrication of SiN microcantilevers and bridges:** fabrication of two different devices: clamped beams (bridges) and clamped-clamped beams (cantilevers), and measurement of the internal stress of silicon nitride films by substrate bending.
- **Fabrication of the polymeric patterned lid:** measurement of the maximum applicable shear force before the polymer detaches from the silicon nitride substrate without adhesion promoter, and fabrication of the polymer lids with channels for bridges and cantilevers.
- **Characterisation:** Measurement of the resonant frequency of both devices without liquid, evaluation of the mass sensitivity and analysis of the damping components.

A Gantt chart is used to have a planned approach in executing the research project (fig. 2.10). The project starts in mid-February with the literature review on resonant structures and the design and simulations with COMSOL. Fabrication starts in April and can take up until August with design improvements gained from experiments. Finally, the results and conclusions will be presented at the beginning of November.

Polymer	Young's modulus [GPa]	Mass density [kg/m ³]	Lateral/axial resolution [nm]	Adhesion to silicon [μm]
IP-S	4.6 [43]	1110 [43]	595/3313 [44]	moderate [40]
IP-Dip	0.75 - 2.9 [43]	1170 [43]	340/826 [44]	moderate [41]
OrmoComp	1 [45]	7000 [43]	100 [45]	good [41]
SZ2080	0.6 - 1.1 [46]	1200 [46]	150 [41]	poor [41]

Table 2.1. Materials parameters for different polymers.

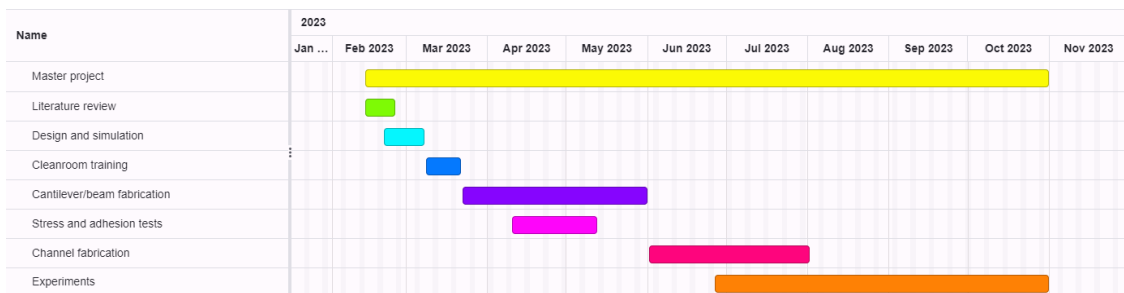


Figure 2.10. Gantt chart of the research project.

Bibliography

- [1] Yasaman Nematbakhsh and C.T. Lim. “Cell biomechanics and its applications in human disease diagnosis”. In: *Acta Mechanica Sinica* 31 (May 2015). DOI: [10.1007/s10409-015-0412-y](https://doi.org/10.1007/s10409-015-0412-y) (cit. on p. 10).
- [2] Giovanna Tomaiuolo. “Biomechanical properties of red blood cells in health and disease towards microfluidics”. In: *Biomicrofluidics* 8 (Sept. 2014). DOI: [10.1063/1.4895755](https://doi.org/10.1063/1.4895755) (cit. on p. 10).
- [3] Javier Tamayo, Priscila Kosaka, Jose Ruz, Alvaro Paulo, and Montserrat Calleja. “Biosensors based on nanomechanical systems”. In: *Chemical Society reviews* 42 (Nov. 2012). DOI: [10.1039/c2cs35293a](https://doi.org/10.1039/c2cs35293a) (cit. on p. 10).
- [4] Demir Akin and Rashid Bashir. “Single virus particle detection using microresonators with nanoscale thickness”. In: *Applied Physics Letters - APPL PHYS LETT* 84 (Mar. 2004). DOI: [10.1063/1.1667011](https://doi.org/10.1063/1.1667011) (cit. on p. 10).
- [5] Luis Guillermo Villanueva, Jose Plaza, J. Montserrat, Francesc Pérez-Murano, and Joan Bausells. “Crystalline silicon cantilevers for piezoresistive detection of biomolecular forces”. In: *Microelectronic Engineering* 85 (Feb. 2008). DOI: [10.1016/j.mee.2008.01.082](https://doi.org/10.1016/j.mee.2008.01.082) (cit. on p. 10).
- [6] In-Bok Baek et al. “Attogram mass sensing based on silicon microbeam resonators”. In: *Scientific Reports* 7 (Apr. 2017). DOI: [10.1038/srep46660](https://doi.org/10.1038/srep46660) (cit. on p. 10).
- [7] Y. Kasai, Hiroshi Yabuno, T. Ishine, Y. Yamamoto, and S. Matsumoto. “Mass sensing using a virtual cantilever virtually coupled with a real cantilever”. In: *Applied Physics Letters* 115 (Aug. 2019). DOI: [10.1063/1.5111202](https://doi.org/10.1063/1.5111202) (cit. on p. 10).
- [8] Joao Mouro, Bruno Tiribilli, and Paolo Paoletti. “A Versatile Mass-Sensing Platform With Tunable Nonlinear Self-Excited Microcantilevers”. In: *IEEE Transactions on Nanotechnology* PP (Apr. 2018). DOI: [10.1109/TNANO.2018.2829404](https://doi.org/10.1109/TNANO.2018.2829404) (cit. on p. 10).
- [9] Thomas Burg, Amir Mirza, Nebojsa Milovic, Christine Tsau, George Popescu, John Foster, and Scott Manalis. “Vacuum-Packaged Suspended Microchannel Resonant Mass Sensor for Biomolecular Detection”. In: *Microelectromechanical Systems, Journal of* 15 (Jan. 2007). DOI: [10.1109/JMEMS.2006.883568](https://doi.org/10.1109/JMEMS.2006.883568) (cit. on p. 10).
- [10] Scott Manalis. “Suspended microchannel resonators for biomolecular detection”. In: (Mar. 2005), pp. 7004– (cit. on pp. 10, 14).
- [11] Thomas Burg, Michel Godin, Scott Knudsen, Wenjiang Shen, Greg Carlson, John Foster, Ken Babcock, and Scott Manalis. “Weighing of biomolecules, single cells and single nanoparticles in fluid”. In: *Nature* 446 (May 2007). DOI: [10.1038/nature05741](https://doi.org/10.1038/nature05741) (cit. on p. 10).
- [12] Murali Ghatkesar et al. “Higher modes of vibration increase mass sensitivity in nanomechanical microcantilevers”. In: *Nanotechnology* 18 (Oct. 2007). DOI:

- [10.1088/0957-4484/18/44/445502](https://doi.org/10.1088/0957-4484/18/44/445502) (cit. on p. 11).
- [13] Robert Felgar and Dana Young. “Tables of Characteristic Functions Representing Normal Modes of Vibration of a Beam”. In: (Jan. 1949) (cit. on p. 11).
- [14] Thomas Braun, Viola Barwich, Murali Ghatkesar, Adriaan Bredekamp, Christoph Gerber, Martin Hegner, and Hans Lang. “Micromechanical mass sensors for biomolecular detection in a physiological environment”. In: *Physical review. E, Statistical, nonlinear, and soft matter physics* 72 (Oct. 2005). DOI: [10.1103/PhysRevE.72.031907](https://doi.org/10.1103/PhysRevE.72.031907) (cit. on pp. 11, 12).
- [15] Silvan Schmid, Luis Guillermo Villanueva, and Michael Roukes. *Fundamentals of Nanomechanical Resonators*. Jan. 2016. DOI: [10.1007/978-3-319-28691-4](https://doi.org/10.1007/978-3-319-28691-4) (cit. on pp. 11, 13–15).
- [16] B.D. Hauer, Cailin Doolin, K. Beach, and John Davis. “A general procedure for thermomechanical calibration of nano/micro-mechanical resonators”. In: *Annals of Physics* 339 (May 2013). DOI: [10.1016/j.aop.2013.08.003](https://doi.org/10.1016/j.aop.2013.08.003) (cit. on p. 11).
- [17] Annalisa De Pastina and Luis Guillermo Villanueva. “Suspended micro/nano channel resonators: a review”. In: *Journal of Micromechanics and Microengineering* 30 (Jan. 2020). DOI: [10.1088/1361-6439/ab6df1](https://doi.org/10.1088/1361-6439/ab6df1) (cit. on pp. 12, 14, 16).
- [18] Selim Olcum et al. “Weighing nanoparticles in solution at the attogram scale”. In: *Proceedings of the National Academy of Sciences of the United States of America* 111 (Jan. 2014). DOI: [10.1073/pnas.1318602111](https://doi.org/10.1073/pnas.1318602111) (cit. on p. 12).
- [19] Jame lu, T. Ikehara, Yuanya Zhang, Takashi Mihara, T. Itoh, and Ryutaro Maeda. “High quality factor silicon cantilever driven by PZT actuator for resonant based mass detection”. In: May 2008. DOI: [10.1109/DTIP.2008.4752953](https://doi.org/10.1109/DTIP.2008.4752953) (cit. on pp. 12, 13).
- [20] Abdelhamid Maali, Touria Cohen-Bouhacina, Cedric Hurth, Cédric Jai, R. Boisgard, and Jean-Pierre Aimé. “Dynamic AFM in Liquids: Viscous Damping and Applications to the Study of Confined Liquids”. In: *Applied Scanning Probe Methods XII: Characterization*. Ed. by Bharat Bhushan and Harald Fuchs. Berlin, Heidelberg: Springer Berlin Heidelberg, 2009, pp. 149–164. DOI: [10.1007/978-3-540-85039-7_7](https://doi.org/10.1007/978-3-540-85039-7_7) (cit. on p. 13).
- [21] Murali Ghatkesar, Thomas Braun, Viola Barwich, Jean-Pierre Ramseyer, Christoph Gerber, Martin Hegner, and Hans Lang. “Resonating modes of vibrating microcantilevers in liquid”. In: *Applied Physics Letters* 92 (Jan. 2008). DOI: [10.1063/1.2838295](https://doi.org/10.1063/1.2838295) (cit. on p. 13).
- [22] John Sadera. “Frequency response of cantilever beams immersed in viscous fluids with applications to the atomic force microscope”. In: *Journal of Applied Physics* 84 (July 1998). DOI: [10.1063/1.368002](https://doi.org/10.1063/1.368002) (cit. on p. 13).
- [23] Siavash Pourkamali, Akinori Hashimura, Reza Abdolvand, Gavin Ho, Ahmet Erbil, and Farrokh Ayazi. “High-Q single crystal silicon HARPSS capacitive beam resonators with self-aligned sub-100-nm transduction gaps”. In: *Microelectromechanical Systems, Journal of* 12 (Sept. 2003). DOI: [10.1109/JMEMS.2003.811726](https://doi.org/10.1109/JMEMS.2003.811726) (cit. on p. 13).

- [24] Julie Hao, Ahmet Erbil, and Farrokh Ayazi. “An analytical model for support loss in micromachined beam resonators with in-plane flexural vibrations”. In: *Sensors and Actuators A: Physical* 109 (Dec. 2003). DOI: [10.1016/j.sna.2003.09.037](https://doi.org/10.1016/j.sna.2003.09.037) (cit. on p. 13).
- [25] Faruq Foong and Chung Ket Thein. “On mechanical damping of cantilever beam-based electromagnetic resonators”. In: *Mechanical Systems and Signal Processing* 119 (Mar. 2019). DOI: [10.1016/j.ymsp.2018.09.023](https://doi.org/10.1016/j.ymsp.2018.09.023) (cit. on p. 13).
- [26] Selim Olcum, Nathan Cermak, and Scott Manalis. “Precision mass measurements in solution reveal properties of single cells and bioparticles”. In: Dec. 2015. DOI: [10.1109/IEDM.2015.7409691](https://doi.org/10.1109/IEDM.2015.7409691) (cit. on p. 14).
- [27] John Sader, Jungchul Lee, and Scott Manalis. “Energy dissipation in microfluidic beam resonators: Dependence on mode number”. In: *Journal of applied physics* 108 (Dec. 2010). DOI: [10.1063/1.3514100](https://doi.org/10.1063/1.3514100) (cit. on pp. 14–16).
- [28] John Sader, Thomas Burg, Jungchul Lee, and Scott Manalis. “Energy dissipation in microfluidic beam resonators: Effect of Poisson’s ratio”. In: *Physical review. E, Statistical, nonlinear, and soft matter physics* 84 (Aug. 2011). DOI: [10.1103/PhysRevE.84.026304](https://doi.org/10.1103/PhysRevE.84.026304) (cit. on p. 16).
- [29] Andrea Gerbino. “Energy Dissipation in Suspended Microchannel Resonators: theoretical, numerical and experimental validation”. MA thesis. Sapienza Università di Roma, 2018 (cit. on p. 16).
- [30] Faheem Khan, Silvan Schmid, Zachary Davis, S. Dohn, and Anja Boisen. “Fabrication of resonant micro cantilevers with integrated transparent fluidic channel”. In: *Microelectronic Engineering* (Aug. 2011). DOI: [10.1016/j.mee.2011.02.096](https://doi.org/10.1016/j.mee.2011.02.096) (cit. on p. 17).
- [31] Thomas Burg, Michel Godin, Scott Knudsen, Wenjiang Shen, Greg Carlson, John Foster, Ken Babcock, and Scott Manalis. “Weighing of biomolecules, single cells and single nanoparticles in fluid”. In: *Nature* 446 (May 2007). DOI: [10.1038/nature05741](https://doi.org/10.1038/nature05741) (cit. on p. 17).
- [32] Celine Hadji, Clement Berthet, Francois Baléras, Martine Cochet, Béatrice Icard, and Vincent Agache. “Hollow MEMS mass sensors for real-time particles weighing and sizing from a few 10 nm to the μm scale”. In: vol. 2015. Feb. 2015. DOI: [10.1109/MEMSYS.2015.7050916](https://doi.org/10.1109/MEMSYS.2015.7050916) (cit. on p. 17).
- [33] Joohyun Kim et al. “Hollow Microtube Resonators via Silicon Self-Assembly toward Subattogram Mass Sensing Applications”. In: *Nano letters* 16 (Jan. 2016). DOI: [10.1021/acs.nanolett.5b03703](https://doi.org/10.1021/acs.nanolett.5b03703) (cit. on p. 17).
- [34] Robert Kramer, Eleonoor Verlinden, Livia Angeloni, Anita Heuvel, Lidy Fratila-Apachitei, Silvére Maarel, and Murali Ghatkesar. “Multiscale 3D-printing of Microfluidic AFM Cantilevers”. In: *Lab on a Chip* 20 (Nov. 2019). DOI: [10.1039/C9LC00668K](https://doi.org/10.1039/C9LC00668K) (cit. on p. 17).
- [35] Alexander K. Nguyen and Roger J. Narayan. “Two-photon polymerization for biological applications”. In: *Materials Today* 20.6 (2017), pp. 314–322. DOI: <https://doi.org/10.1016/j.mattod.2017.06.004> (cit. on p. 17).
- [36] Mehdi Daryani, Tomás Manzaneque, Jia Wei, and Murali Ghatkesar. “Measuring nanoparticles in liquid with attogram resolution using a microfabricated glass suspended microchannel resonator”. In: *Microsystems and Nanoengineering* 8

- (Aug. 2022). DOI: [10 . 1038 / s41378 - 022-00425-8](https://doi.org/10.1038/s41378-022-00425-8) (cit. on pp. 17, 18).
- [37] Jikke de Winter. “Toward 3D printed suspended microchannel resonators: A study on damping and mass resolution of 3D printed microbeam resonators”. MA thesis. Delft University of Technology, 2022 (cit. on pp. 17, 19).
- [38] Z. Faraji Rad, P.D. Prewett, and G.J. Davies. “High-resolution two-photon polymerization: the most versatile technique for the fabrication of microneedle arrays”. In: *Microsystems and Nano-engineering* 71 (Sept. 2021). DOI: [10 . 1038 / s41378 - 021 - 00298 - 3](https://doi.org/10.1038/s41378-021-00298-3) (cit. on p. 18).
- [39] URL: https://www.mit.edu/~6.777/matprops/lpcvd_sin.htm (cit. on p. 19).
- [40] Saisneha Koppaka, Kevin Zhang, Myra Kurosu Jalil, Lucas Blauch, and Sindy Tang. “Fabrication of 3D Micro-Blades for the Cutting of Biological Structures in a Microfluidic Guillotine”. In: (July 2021). DOI: [10 . 20944 / preprints202107 . 0597 . v1](https://doi.org/10.20944/preprints202107.0597.v1) (cit. on pp. 20, 22).
- [41] Margarita Sharipova et al. “Effect of pyrolysis on microstructures made of various photoresists by two-photon polymerization: comparative study”. In: *Optical Materials Express* 11 (Feb. 2021). DOI: [10 . 1364 / OME . 416457](https://doi.org/10.1364/OME.416457) (cit. on pp. 20, 22).
- [42] Anna Guell Izard, E. Garcia, Matthew Dixon, E. Potma, T. Baldacchini, and Lorenzo Valdevit. “Enhanced adhesion in two-photon polymerization direct laser writing”. In: *AIP Advances* 10 (Apr. 2020). DOI: [10 . 1063 / 5 . 0005548](https://doi.org/10.1063/5.0005548) (cit. on p. 20).
- [43] Enrico Domenico Lemma, Francesco Rizzi, Tommaso Dattoma, Barbara Spagnolo, Leonardo Sileo, Antonio Quattieri, Massimo de Vittorio, and Ferruccio Pisanello. “Mechanical Properties Tunability of Three-Dimensional Polymeric Structures in Two-Photon Lithography”. In: *IEEE Transactions on Nanotechnology* 16 (2017) (cit. on p. 22).
- [44] URL: <https://www.nanoscribe.com/en/products/ip-photoresins/> (cit. on p. 22).
- [45] URL: <https://www.microresist.de/en/produkt/ormocomp/> (cit. on p. 22).
- [46] L. Pertoldi, Valentina Zega, Claudia Comi, and R. Osellame. “Dynamic mechanical characterization of two-photon-polymerized SZ2080 photoresist”. In: *Journal of Applied Physics* 128 (Nov. 2020). DOI: [10 . 1063 / 5 . 0022367](https://doi.org/10.1063/5.0022367) (cit. on p. 22).

Chapter 3

Hybrid suspended microchannel resonator for mass detection in liquid

Hybrid suspended microchannel resonator for mass detection in liquid

Suspended microchannel resonators are the best candidates for a variety of technological applications requiring accurate measurements in liquid. These devices eliminate the viscous damping by placing the solution inside a hollow resonator surrounded by vacuum, thus reaching sub-femtogram resolution. In the last few years, TPP-printed polymeric resonators emerged as a valid solution to increase the low prototyping speed and accessibility of silicon-based resonators, but showed a low quality factor and mass sensitivity. In this work, a novel fabrication technique based on a hybrid structure has been developed. A single-mask cleanroom fabrication process was carried out to create silicon nitride supporting beams. Then, 3D printing by two-photon polymerization (TPP) was used to fabricate microfluidic lids. Fabricated devices were mechanically characterised in vacuum by laser Doppler vibrometry before and after the printing process. A quality factor of 510 at 341 kHz was reached with a 350 μm x 50 μm hybrid double-clamped beam. The theoretical mass responsivity and maximum mass resolution of this device were estimated to be 1.84 Hz/pg and 14.75 ag, respectively, which still compete with conventional fabricated SMRs.

Index terms – Suspended microchannel resonator, 3D printing, Two-photon polymerization, Silicon nitride microbeam resonator, Damping, Quality factor, Mass sensing, Mass resolution.

3.1 Introduction

Resonant cantilevers or bridges have long been employed as dynamic mechanical devices for cell mass sensing [1, 2, 3]. These sensors exhibit exceptional performance in gaseous environments, achieving high quality factors and precise mass measurements. However, their effectiveness is compromised in liquid environments due to over-damped responses, limiting their mass resolution capabilities [4].

To overcome these challenges, a groundbreaking solution was introduced in 2003 by Burg and Manalis: the suspended microchannel resonator (SMR) [5]. The SMR presents a unique hollow resonant structure with an embedded microfluidic channel, which allows the analyzed liquid to flow inside the resonator. This design eliminates the effects of viscous damping, reducing mass loading and enhancing the sensitivity of the device.

When particles suspended in a solution flow

through a resonating hollow cantilever, changes in mass inside the channel translate into shifts in resonant frequency. This shift can be determined from equation 3.1 [6]:

$$f = \frac{1}{2\pi} \sqrt{\frac{k}{m^* + \alpha \Delta m}} \quad (3.1)$$

Where the spring constant of the resonator is denoted by k , m^* is the effective mass, and α is a numerical constant that depends on the geometric localization of the added mass Δm .

Sub-femtogram accurate mass measurements in vacuum [6] have been performed by using suspended microchannel resonators fabricated by standard cleanroom micro/nanofabrication techniques. These manufacturing methods enable the realization of micrometer-sized structures with nanometric precision by means of repeated steps of deposition, photolithography, and etching. Multiple nearly identical devices are realised simultaneously on the same substrate, with precise control over

the process parameters. To proceed with each stage, a patterning mask is necessary, and any modifications in the design necessitate the creation of a new mask, resulting in increased prototyping costs. Furthermore, the height of the cantilever designs is limited to a few micrometers height due to the reduced thickness of the deposited materials.

A fabrication technique that overcomes these limitations and provides enhanced flexibility is 3D printing. This method facilitates rapid and cost-effective prototyping, reduces equipment costs, and streamlines the process into a single step. By leveraging 3D printing, the design space gains an additional degree of freedom, enabling the creation of out-of-plane designs that would otherwise be impractical using conventional micro/nano-fabrication techniques.

However, 3D-printed structures are usually made of polymeric materials. This entails the fabrication of resonators with low Young's modulus, and thus low Q-factors [7, 8].

A technique that allows for greater flexibility and more rapid prototyping than cleanroom fabrication alone, and ensures higher Young's modulus than 3D-printed structures consists of combining the 3D printing and the silicon-based processes.

In this work, the limitations and the advantages of standard cleanroom fabricated cantilevers and polymeric beams were taken into account to develop a new hybrid resonating structure. The resulting suspended microchannel resonator consists of two separated parts: a supporting silicon nitride beam realised by bulk micro-machining and a polymer lid with a patterned channel fabricated by two-photon polymerization (TPP). The final silicon chip with the polymeric channel can be connected to external tubing through a 3D-printed microfluidic interface. A schematic view of the device is shown in figure 3.1.

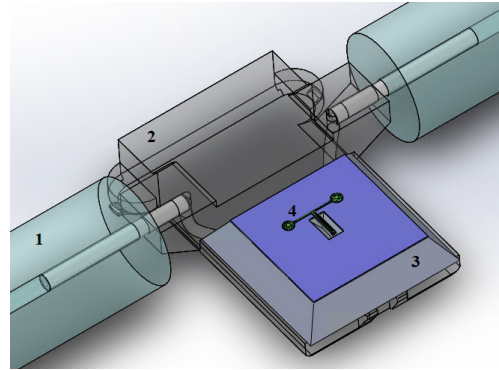


Figure 3.1. *Schematic picture of the concept. The connected external tubing is labelled as 1, the fluidic interface as 2, the TPP-printed channel as 3, and the silicon chip with the silicon nitride supporting beam as 4.*

Two 3D printing techniques have been used for realisation of the complete device: stereolithography, to produce the microfluidic interface, and TPP, to print the hollowed layer with micrometer resolution.

The materials used for the two fabrication steps are different, i.e., Si-rich silicon nitride for the supporting beam, and IP-Dip resin for the polymeric lid, and therefore adhesion between the cleanroom fabricated structure and TPP-printed layer was investigated. The cantilever was mechanically characterized with and without the TPP-printed lid to evaluate the impact of the polymeric layer on resonant frequency and Q-factor. Its fluidic functionality was analysed, and its limits in terms of resolution and mass sensitivity were defined.

3.2 Materials and methods

3.2.1 Cleanroom microfabrication

Supporting cantilevers and bridges in silicon nitride have been realised simultaneously using a single-mask fabrication process. Schematic of the manufacturing steps is shown in fig. 3.2.

A silicon nitride layer was deposited by LPCVD on the silicon substrate and then patterned by RIE. A subsequent KOH etching step

enabled the release of the suspended structures. Aluminum–silicon(1%) was sputtered on the whole wafer to create a thin reflecting layer for the 3D printing step. The two holes connecting the channel to the outside world were realised by laser drilling after the wafer dicing. Further details of the fabrication process can be found in annex B.2. Table 3.1 shows the relevant dimensions of the devices.

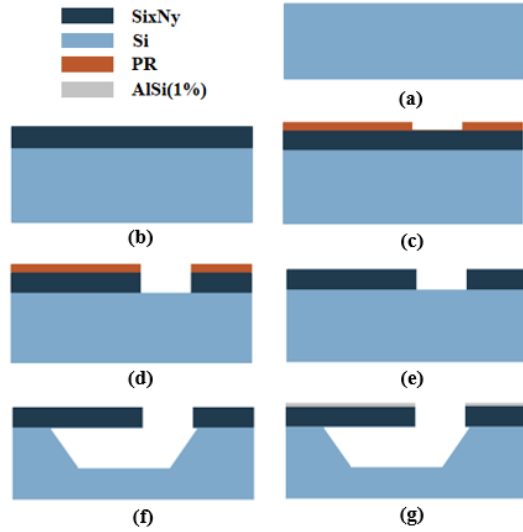


Figure 3.2. Flowchart of the cleanroom fabrication process: (a) cleaning of Si<100> substrate, (b) deposition of low-stress SiN by LPCVD, (c) photoresist (PR) spin coating and photolithography, (d) RIE of SiN to create the suspended structures and scribelines, (e) PR removal, (f) release of the bridges and cantilevers by KOH etching and wafer cleaning, and (g) AlSi(1%) sputtering

Parameter	Value [μm]
Beam thickness	2
Beam width	30 - 50
Beam length	250 - 500
Bridge channel length (suspended)	250 - 500
Cantilever channel length (suspended)	515 - 1025
Cantilever gap	15 - 25

Table 3.1. Dimensions of the devices.

3.2.2 Two photon polymerization

A TPP-printer (Nanoscribe GmbH, photonic professional GT) with sub-micron resolution was used for printing the lid with the embedded channel on bridges and cantilevers. The same printer was employed to create the microfluidic connection from the inlet/outlet to the suspended channel.

The computer-aided design (CAD) of the microfluidic channel is shown in fig. 3.3. The polymeric structure was designed to reduce the printing time, and to maximize the attached surface area, thus increasing the adhesion to the substrate. The rectangular slits at the base of the domes (see fig. 3.3(b)) were added to help

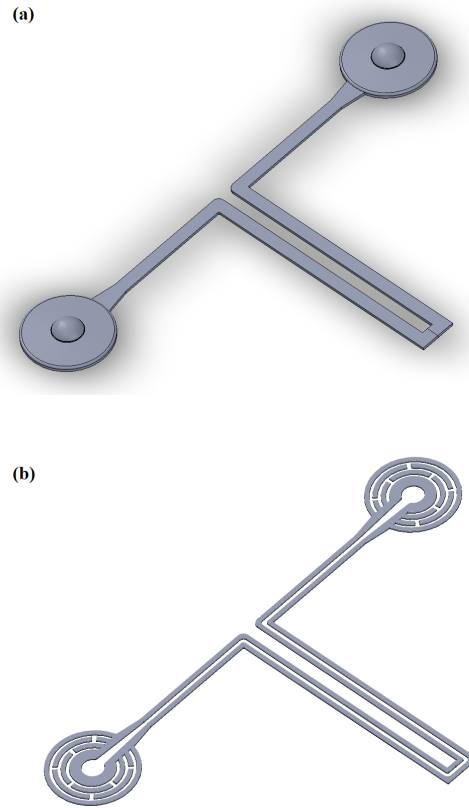


Figure 3.3. (a) Schematic of the IP-Dip structure with the two domes connecting the suspended channel to the external fluidic interface; (b) section showing the base of the IP-Dip structure.

with the issue of bubble formation when printing on metals. These bubbles are generated when the femtosecond laser locally changes the methacrylate/acrylate-based material into a gaseous plasma, which reforms into gaseous carbon compounds. The slits can stop the small, originally generated bubbles from consolidating and shielding the laser.

IP-Dip photoresist (Nanoscribe GmbH & Co. KG, Germany) with a carbamate/methacrylate base was utilised. This resin allows to reach the lowest resolution and obtain a channel with the smallest section.

The polymeric structure was printed on the AlSi sputtered surface using the "Dip-in laser lithography" (DiLL) or "dip-in" configuration, shown in fig. 3.4.

In this configuration, the surface is covered with a drop of liquid resin and turned upside down. The resin serves both as a polymer precursor and an immersion medium for the microscope objective. The laser beam is directed through the liquid resin after passing through the microscope objective. Printing starts on the interface between the resin and the substrate and proceeds downwards [9].

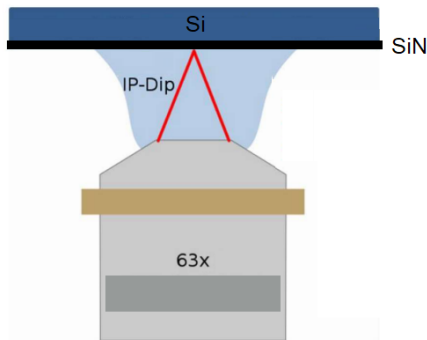


Figure 3.4. Schematic of the DiLL configuration.

Printing settings are shown in table 3.2 and further details of the TPP-printing step can be found in annex B.3.

Parameter	Value
Solid laser power	28.5 mW
Base laser power	17.1 mW
Scanning speed	10 mm/s
Objective	63x NA 1.4
Slicing distance	0.3 μm
Hatching distance	0.2 μm
Base count	10

Table 3.2. TPP-printing parameters.

3.2.3 Stereolithography

The fluidic interface for the connection of the chip to the external world has been realised by stereolithography (SLA). It is a printing technique based on the photochemical solidification of a liquid photopolymer resin: a UV laser illuminates a thin layer of resin at a time to create the 3D object layer-by-layer.

The commercial desktop stereolithography printer (EnvisionTEC GmbH. Micro R Plus Hi-Res) used for the interface fabrication has a minimum xy-resolution of 30 μm and a z-resolution of 25 μm . The printed material was a methacrylate/acrylate-based resin (HTM140V2M, EnvisionTec GmbH.).

The resolution limit is low enough to create channels that can be connected to the holes drilled into the silicon die, and high enough to obtain a device that can still be handled by tweezers and connected by hand to the tubing.

The CAD of the interface is shown in fig. 3.5. Its shape allows for mounting the fluidic interface on the AFM Nanosurf holder that is located in the vacuum chamber for frequency measurements.

The same technique has been employed to fabricate a holder for the TPP printing.

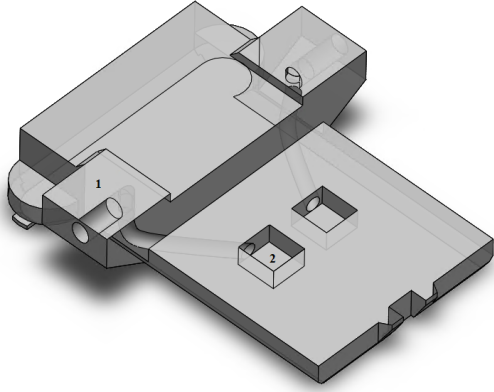


Figure 3.5. CAD design of the fluidic interface. The channels for the connection to external tubing are labelled as 1, and the holes for the connection to the inlet and the outlet of the SMR as 2.

3.2.4 Pillar fabrication for Young's modulus and adhesion force measurements

In order to measure the Young's modulus of the TPP-printed IP-Dip layer, an array of twelve square pillars with a cross-sectional area of $35\ \mu\text{m} \times 35\ \mu\text{m}$ and a height of $45\ \mu\text{m}$ was designed. The structures were printed on a Si substrate, on which a $2\ \mu\text{m}$ thick Si-rich SiN layer was deposited by LPCVD and then a $30\ \text{nm}$ thick AlSi layer was sputtered. Compression test was performed using FTNMT03 Nanomechanical Testing System (FemtoTools AG, Switzerland) to obtain the force-displacement curve and derive the mechanical parameter (see fig.3.6(a)). Size and cross-section of the pillars were designed so as to match the tip shape and dimensions, and not to exceed the force-displacement limits of the measurement system.

After a first measurement to determine the initial Young's modulus, the pillars were exposed to ultraviolet (UV) light. The effect of the post-development treatment has been an increase in the elastic modulus of the polymer due to homogenization of the cross-linking of

the printed resin [10]. The treatment lasted 40 minutes and was performed with the PHOTOPOL light (Dentalfarm SRL, Italy) with a UV wavelength ranging from 320 to 550 nm.

Pillars with different cross-sections were printed on the same substrate to study the adhesion force to the substrate. Two square pillars of $70\ \mu\text{m} \times 70\ \mu\text{m} \times 250\ \mu\text{m}$ and $80\ \mu\text{m} \times 80\ \mu\text{m} \times 250\ \mu\text{m}$ volume were designed to perform a compression test and obtain a share force-displacement curve.

The experiment was performed with an FTNMT03 Nanomechanical Testing System (FemtoTools AG, Switzerland) using a 15° tip. The experimental setup is shown in fig.3.6(b): the tip exerts a share force against the lateral side of the pillar until the structure detaches from the substrate. A load range from zero to 11 mN in steps of $10\ \mu\text{N}$ was applied on each cube. Further details on the printed structures and compression tests are illustrated in annex C.1.

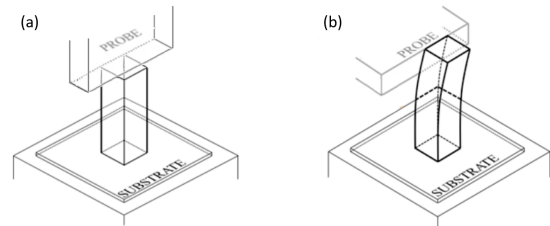


Figure 3.6. Schematic view of the experimental setup used for compression tests: (a) the tip is pushed against the top side of the pillar to vertically deform the structure, (b) the tip is pushed against the lateral side of the pillar to detach it from the surface.

3.2.5 Resonant frequency measurements

An MSA-400-PM2-D Laser Doppler vibrometer (Polytec GmbH, Germany) equipped with the MSA-A-M20X lens was used to characterise the resonators. Resonant frequency and Q-factor of both bridges and cantilevers were obtained with and without the IP-Dip lid. The

presence of the AlSi(1%) sputtered layer allowed the resonators to be enough reflective for both measurements.

To study the effect on the Q-factor of the metal layer sputtered on top of the beams, frequency measurements were also performed for bare SiN resonators. Furthermore, a comparative frequency analysis was carried out on beams before and after sputtering a 30 nm thick gold layer.

The velocity peaks at the resonant frequencies and their quality factor were derived from single-point and multi-point data. The samples were placed inside a home-built vacuum chamber and mounted on an AFM Nanosurf holder connected to a piezoelectric actuator made of PIC255 (PI Ceramic GmbH, Germany) with a resonance frequency of roughly 4MHz. All the measurements were made at a vacuum pressure of 5×10^{-5} mbar and room temperature (20°C). The piezo was actuated by a pseudo-random signal with an amplitude of 3 V and a frequency range from 0 Hz to 2 MHz.

3.3 Results

3.3.1 Cleanroom fabricated devices

Suspended beams obtained by standard micro-fabrication process are shown in fig. 3.7.

The cavities were completely etched and the measured lateral over-etching is 4.3 μm . Both bridges and cantilevers appeared straight, thus proving the uniformity of the residual stress in the SiN layer.

3.3.2 TPP-printed hollowed structure

In order to study the impact of the polymeric lid on resonant frequency and Q-factor, structures with different shapes and printing parameters were printed on top of the supporting beams.

As the printing direction has an impact on Young's modulus and mass density of the IP-Dip layer [11], two different printing directions

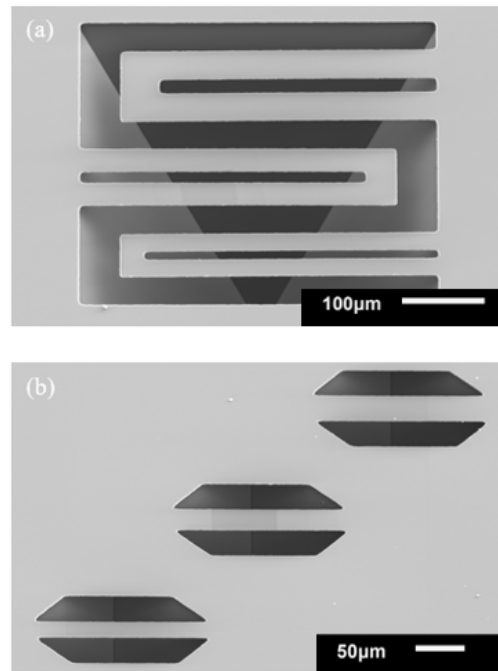


Figure 3.7. SEM picture of (a) 400 μm long cantilevers and (b) 250 μm long bridges after AlSi(1%) sputtering with a tilting angle of 50°.

have been selected: a first direction parallel to the length of the beam (see fig. 3.8(a)), and a second direction perpendicular to the length of the beam (see fig. 3.8(b)).

As a first step, a continuous 5 μm thick IP-Dip layer was printed on both bridges and cantilever, in order to observe the impact of the polymeric layer on Q-factor and resonant frequency. The results of the printing test are shown in fig. 3.9. The thickness of the layer was measured around 4.6 μm , which is slightly less than expected.

As can be seen from the image, in the case of cantilevers the interface to be printed on was not found correctly. Cantilevers bent when printing due to the surface stress induced by the polymeric coat, thus precluding proper adhesion between the two layers. In the case of bridges, instead, the double clamping of the beam prevented the bridge from bending and the adhesion between the layers was better. Moreover, only the layers on 50 μm width

beams were printed along the whole length and without discontinuity. In the other cases, i.e., beams with 30 μm and 40 μm width, the interface was not always found and the printing results were not consistent. On these premises, the following structures were printed only on bridges with variable length and fixed width of 50 μm .

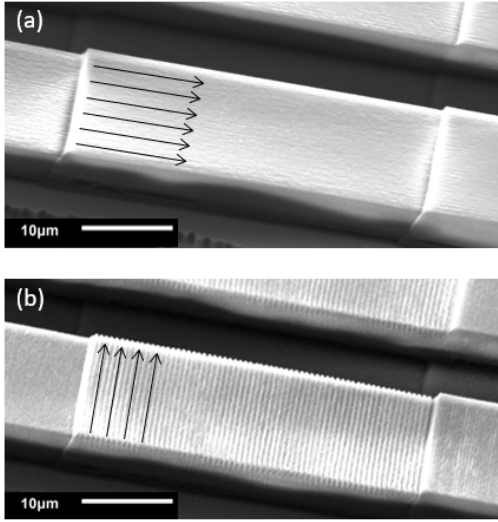


Figure 3.8. SEM pictures of IP-Dip layers printed on top of bridges with (a) parallel printing direction, and (b) perpendicular printing direction.

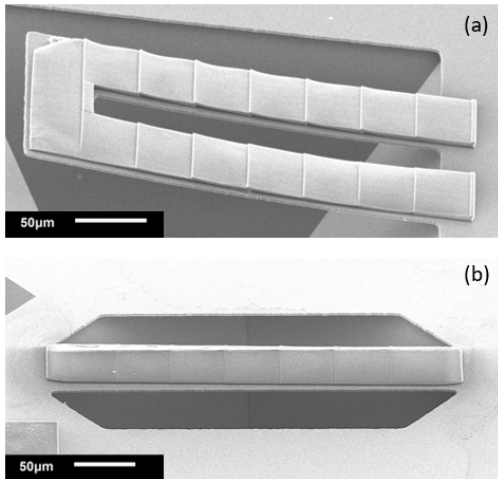


Figure 3.9. SEM pictures of IP-Dip layers printed on top of (a) cantilevers and (b) bridges with perpendicular printing direction.

A second type of structure was printed on top of the bridges to simulate the behaviour of an SMR and, at the same time, to be sure that the channel was completely free of uncured resin. This structure consists of two separated layers of 7.5 μm x 16.5 μm corresponding to the walls of the channel and no lid. The result is shown in fig. 3.10. The measured thickness of the walls is $5.7 \pm 1.2 \mu\text{m}$, which was slightly less than expected.

Lastly, a thin layer of 1.5 μm between the two walls was added to a final printed structure (see fig. 3.11). The measured thickness of the walls and the middle layer are $6.8 \pm 0.5 \mu\text{m}$ and $1.6 \pm 0.2 \mu\text{m}$ respectively, which were pretty similar to the nominal ones.

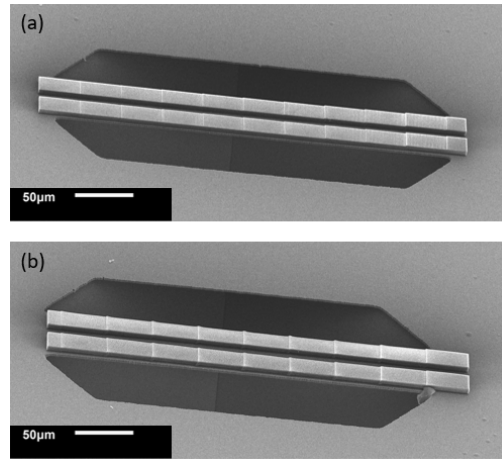


Figure 3.10. SEM pictures of IP-Dip layers printed on top of 400 μm width bridges with (a) perpendicular and (b) parallel printing direction.

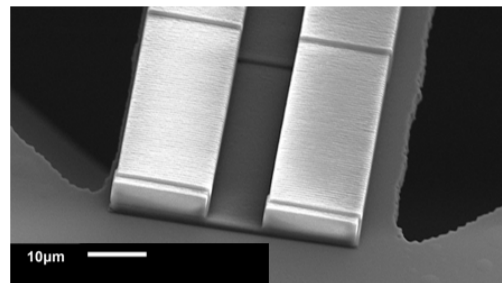


Figure 3.11. SEM pictures of IP-Dip structure with the two walls and the thin layer in between.

The additional layer allows to completely close the liquid inside an IP-Dip channel, thus reducing the possibility of leakage due to partial adhesion between IP-Dip layer and printing substrate. Indeed, it was observed that the printing process is not fully reproducible and, depending on the tilt of the substrate, the printed layer is more or less continuous.

3.3.3 Mechanical characterization of IP-Dip pillars

Young's modulus

Results of the compression measurements for one of the pillars before and after UV-light exposure are illustrated in fig. 3.12.

The average Young's modulus before the UV treatment was 2.43 ± 0.30 GPa; while the value after the UV-light exposure is 3.46 ± 0.41 GPa. Structures did not show any shrinkage due to the exposure.

The Young's modulus before the treatment was in line with the value reported in the literature and used for the FEM simulations. It increased after UV-light exposure, as expected.

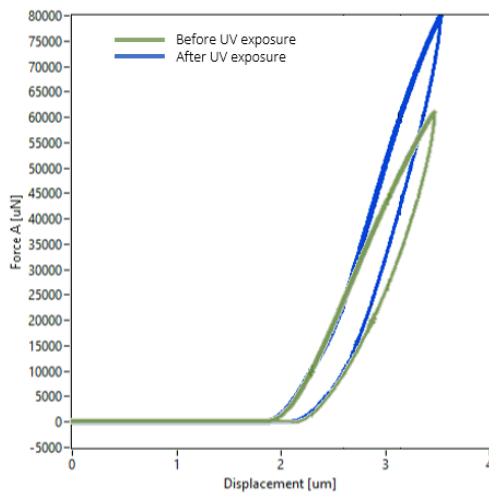


Figure 3.12. Compression force as a function of the tip displacement in the vertical direction.

Adhesion force

Adhesion strength between the AlSi(1%) substrate and the TPP-printed layer determines the maximum pressure that can be exerted by the liquid flowing inside the channel without causing the detachment of the IP-Dip lid. This value can be extracted from the adhesion force measurements illustrated in fig. 3.13.

The vertical jump in each curve represents the abrupt shift of the tip due to the complete detachment of the pillar, as demonstrated by a microscopic analysis.

The maximum adhesion forces before detachment obtained from the test are 10.7 mN for the $80 \mu\text{m} \times 80 \mu\text{m} \times 250 \mu\text{m}$ pillar and 7.6 mN for the $70 \mu\text{m} \times 70 \mu\text{m} \times 250 \mu\text{m}$ pillar. As expected, the pillar with the largest cross-section showed a higher adhesion force.

It follows that these pillars can withstand a maximum shear stress of 1.67 MPa and 1.55 MPa, respectively. These values are indicative of the maximum applicable pressure before detachment.

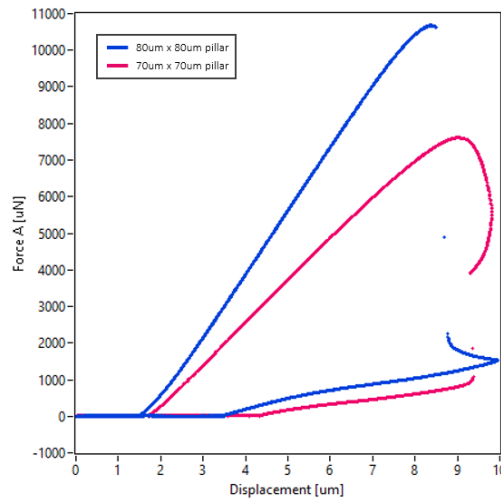


Figure 3.13. Shear force as a function of the tip displacement in the horizontal direction. The curve has been plotted for two pillars with different cross-sections.

3.3.4 Resonant frequency measurements

SiN beams

Resonance frequency of the first resonant mode was measured for all cantilevers and bridges. Tables with the results are reported in annex C.2.

The measured resonant frequencies of the bridge and cantilever with length and width of 250 μm and 30 μm respectively were compared to the simulated ones in table 3.3.

Beam	Mode	f_{sim}	f_{meas}
C	1	44.45	45.15
	2	251.59	261.82
	3	283.97	288.48
B	1	297.99	629.78
	2	821.03	1347.91
	3	1594.50	>2000

Table 3.3. Simulated (*sim*) and measured (*meas*) resonant frequencies in kHz of SiN cantilever (C) and bridge (B).

Measured values match the simulated ones in the cantilever case (error in the range 1.6% - 3.9%); while there is a discrepancy in the bridge case (more than 40% error). The significant increase in the resonant frequency of the double-clamped resonator is due to the intrinsic stress in the SiN, which was not considered in the FEM simulations.

In order to estimate the intrinsic stress effect on the first bending resonant frequency, the analytical model proposed by [12] has been used. The frequency was obtained from eq. 3.2:

$$f = 1.028 \sqrt{\frac{Y}{\rho} \frac{h}{L^2}} \sqrt{1 + 0.295 \left(\frac{L}{h}\right)^2 \varepsilon} \quad (3.2)$$

Where Y is the Young's modulus of silicon nitride, ρ is the mass density, h is the thickness of the beam, L is its length, and ε is the strain

obtained from the measured stress σ using the relation $\sigma = \varepsilon Y$.

All the parameters are listed in annexes A and B.2. The obtained frequency is 684.55 kHz, which is more in line with the measured one (less than 10% error).

Beams with AlSi(1%) layer

To study the effect of the AlSi(1%) layer on resonance frequency and quality factor of the beams, the resonant frequency of the first resonant mode was measured for all cantilevers and bridges. Since it was not possible to do measurements on the same samples before and after sputtering, a different wafer was used for this step. Tables with the results for all bridges and cantilevers are reported in annex C.2.

Table 3.4 shows the resonant frequency and the quality factor of one of the devices in the case of bare SiN and SiN with sputtered AlSi(1%).

f_{SiN}	f_{AlSi}	Q_{SiN}	Q_{AlSi}
271.2	271.4	11590	5950

Table 3.4. Measured resonant frequencies in kHz and Q-factors of 500 μm x 50 μm bridge with 30 nm AlSi(1%).

After the metal layer was added, the resonant frequency varied because of the change in effective stiffness and mass, and the quality factor turned out to be lower than the one without any metallic layer.

Before and after gold sputtering

In order to determine whether the reduction of Q-factors was due to differences between wafers or to the addition of a metal layer, a further study has been performed. The effect of a sputtered metal layer has been studied by measuring the resonance of the devices before and after sputtering a 30 nm thick gold layer. Tables with all the recorded frequencies and the respective Q-factors are reported in annex C.2.

The resonant peaks of one of the bridges measured before and after sputtering are shown in fig. 3.14.

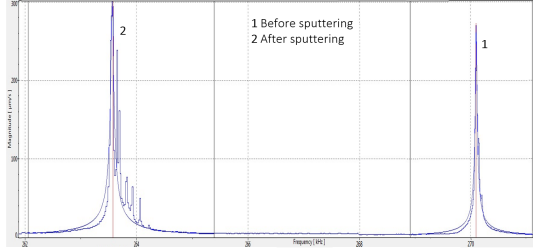


Figure 3.14. First bending resonant frequency of $500 \mu\text{m} \times 50 \mu\text{m}$ bridge before and after gold sputtering.

The measured values of resonant frequency and quality factor are listed in table 3.5.

f_{SiN}	f_{gold}	Q_{SiN}	Q_{gold}
270.10	263.56	9300	5490

Table 3.5. Measured resonant frequencies in kHz and Q-factors of $500 \mu\text{m} \times 50 \mu\text{m}$ bridge before and after gold sputtering.

The image shows the presence of multiple peaks in the case of gold sputtered sample. These peaks have similar mode shapes but different movements of the anchor points, which can be fixed (fig. 3.15(a)) or oscillate in phase or anti-phase with the center of the bridge (fig. 3.15(b)). Fundamental frequencies of the beams correspond to the peak with minimum displacement of the anchor points.

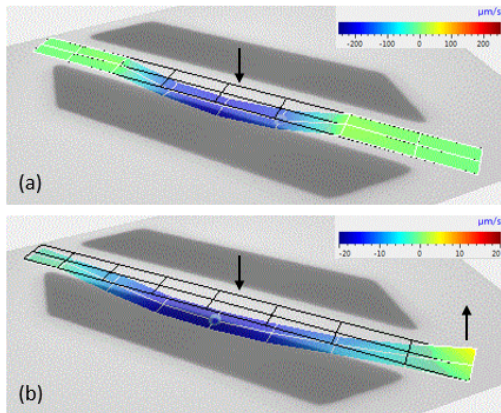


Figure 3.15. Movement of the bridge at the first bending resonant frequency.

The phenomenon of multiple peaks was only observed during experiments on bridges, while was not present in cantilevers. It follows that it is related to the anchor geometry, which is different in the case of clamped and double-clamped beams. Moreover, even when changing the excitation voltage, the relative amplitude of the multiple peaks was not affected.

As expected, after sputtering, the resonant frequency undergoes a shift due to the variation of the overall Young's modulus and mass. The Q-factor decreases significantly, as also observed in the case of AlSi(1%) sputtering.

In metals, energy loss is mainly caused by dislocation movement and is notably high in soft metals like gold and aluminum. Instead, engineering ceramics, e.g., silicon nitride, have low damping since the enormous lattice resistance pins dislocations in place at room temperature [13]. It follows that the high internal friction in gold results in increased internal loss and reduced Q-factor. This occurs for even extremely thin gold coatings [14]. In addition, the presence of a rough thin layer on SiN adversely affects the Q-factor of the beam [15].

Similarly, energy dissipation in AlSi(1%) coated devices can be traced back to the same damping sources: the internal friction in Al and Al alloys is higher than in silicon nitride and the surface of the sputtered layer is quite rough.

With IP-Dip layer

All printed structures were designed so as to have nearly the same mass of polymer on top of the bridges. It follows that the shift in the resonant frequency due to the effective mass should be negligible. However, there is some variability in the thickness of the IP-Dip layer from beam to beam and along the beam itself, which causes a mass and thus a frequency variation in bridges of the same length. In addition, depending on the printing direction, the

mass density and Young's modulus of the polymer vary [11]. This means that identical polymer structures are expected to exhibit different resonant frequencies in the case of parallel and perpendicular printed layers (see fig. 3.16).

As concerns the Q-factor, given a fixed length, significant variations are present both considering different types of structure and printing direction. Figure 3.17 shows the behaviour of the quality factor for distinct IP-Dip structures.

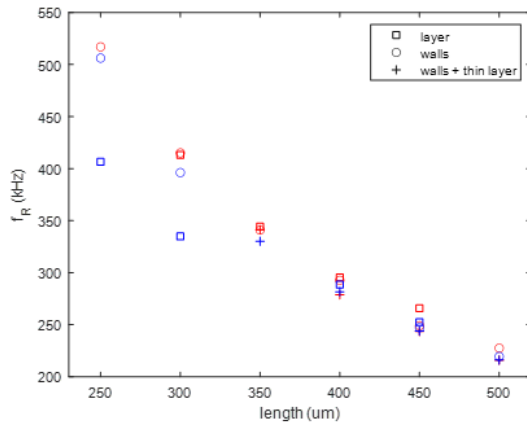


Figure 3.16. Resonant frequency vs bridge length for IP-Dip structures with parallel (red) and perpendicular (blue) printing direction. The structures are a continuous layer of $4.6 \mu\text{m}$ (layer), two layers of $7.5 \mu\text{m}$ (walls) and two walls with a thin middle layer of $1.5 \mu\text{m}$ in between (walls + thin layer).

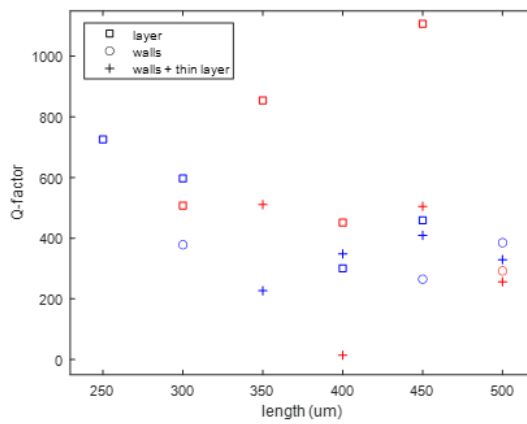


Figure 3.17. Quality factor vs bridge length for different IP-Dip structures with parallel (red) and perpendicular (blue) printing direction.

Quality factors and resonant frequencies for all devices are listed in tables in annex C.2. The highest Q-factor was measured for the $450 \mu\text{m}$ long bridge with the parallel printed continuous layer, and it is 1107 at 266 kHz. The magnitude and phase graph with the first resonating mode are given in fig. 3.18.

Considering the walls cases, the maximum value was obtained for the $350 \mu\text{m}$ long bridge with the additional thin layer with parallel printing direction. The frequency spectrum of this $350 \mu\text{m}$ long bridge is shown in fig. 3.19. The first resonating mode of the device is distinguishable both from the magnitude and phase graph of the single-point measurement. The measured Q-factor is 510 at 341 kHz. This value is lower than the highest quality factor obtained by [7] for untreated bridges, corresponding to 914 at 459 kHz. Nevertheless, the frequency spectrum has no multiple peaks and the resonance is also evident from the phase change, unlike bridges made entirely in polymer.

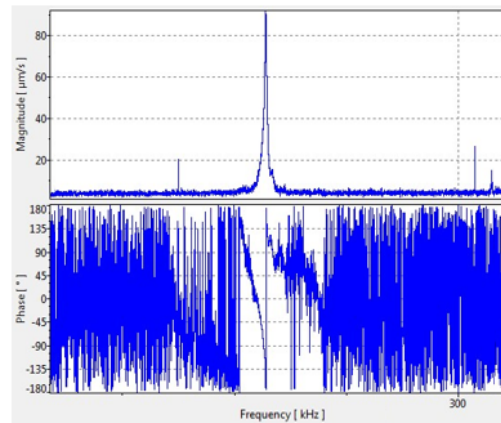


Figure 3.18. Frequency spectrum of the $450 \mu\text{m}$ long bridge with the IP-Dip continuous layer printed parallel to the beam length. The magnitude peak and the phase change correspond to the first resonating mode.

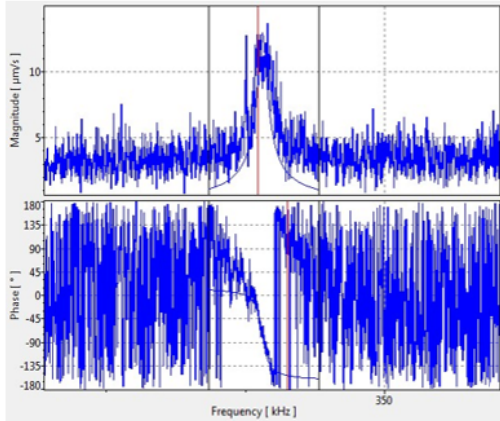


Figure 3.19. Frequency spectrum of the 350 μm long bridge with the IP-Dip walls and thin layer printed parallel to the beam length. The magnitude peak and the phase change correspond to the first resonating mode.

UV-cured structures

One last experiment has been performed by UV-curing the hybrid structures for 40 min with a wavelength ranging from 320 to 550 nm. The effect of this post-development treatment was the increase and homogenization of the cross-linking of the polymer. As a consequence, Young's modulus increased by 1.4 times and the energy dissipation was expected to decrease. In polymers, indeed, the main losses are caused by dislocation movement: chain segments slide against each other dissipating energy [13]. The easier the chain slip-page, the higher the damping.

The UV treatment was carried out only on the bridges with the highest quality factor, i.e., with two walls and a thin layer in between. Q-factors after 40 min UV-light exposure are plotted in fig. 3.20.

All treated devices had an increased resonance frequency with respect to untreated devices due to the higher Young's modulus of the IP-Dip layer. Regarding the dissipated energy, UV exposure did not always produce an increase in the Q-factor: this occurred only in the

case of 450 μm long bridges with perpendicular printed layer and 500 μm long bridges with parallel printed layer. Other devices had a Q-factor significantly lower than untreated beams of the same length. The largest increase in quality factor was for the 450 μm long bridge, which increased from 409 at 244 kHz for the untreated device to 449 at 245 kHz for the UV-cured one. However, it is still lower than the maximum Q reached by untreated devices.

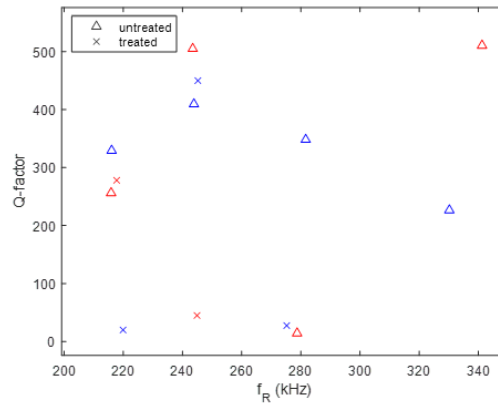


Figure 3.20. Quality factor vs bridge length for treated and untreated structures with parallel (red) and perpendicular (blue) printing direction.

3.3.5 Estimated mass responsivity and sensitivity

The mass responsivity of the device with two IP-Dip walls with the highest quality factor (510 at 341 kHz) was calculated using eq. 2.3. Considering a water-filled channel, the resulting mass responsivity is 1.84 Hz/pg.

The mass resolution of the same hybrid SMR is estimated to be $363 \frac{1}{SNR} \text{fg}$, when there is no liquid inside the channel. If water is introduced into the channel, the medium interaction damping caused by the flowing liquid must be taken into account when calculating the overall quality factor. The Q-factor related to the medium loss is expected to be 894 from COMSOL simulations (FEM model presented

in annex A.5). It follows that the total quality factor is 325 and the related mass resolution is $570 \frac{1}{\text{SNR}} \text{fg}$. These values of mass resolution are still dependent on the signal-to-noise ratio (SNR), and can only improve once this is determined.

Further analysis can be performed by considering the relationship between mass resolution and frequency resolution (Allan deviation), expressed in eq. 2.7. The best case occurs when the Allan deviation $\sigma_y(\tau)$ reaches its minimum.

To a first approximation, the frequency noise can be only related to the silicon nitride layer, dealing with the IP-Dip lid as a damping material surrounding the supporting bridge. Under these assumptions, the hybrid device is reduced to a rectangular double-clamped beam with thickness h . Taking into account the material properties, dimensions, quality factor, and temperature, the minimum Allan deviation due to geometrical non-linearity for fast sensing is given by eq. 3.3 [16]:

$$\sigma_{y|min} = \frac{\sqrt[4]{3}}{2} \sqrt{\frac{k_B T \gamma}{Q k_1}} \quad (3.3)$$

where k_B is the Boltzmann constant, T is the absolute temperature, Q is the quality factor, k_1 is the modal stiffness, and γ is the Duffing coefficient, defined as the cubic stiffness divided by the linear stiffness. The Duffing coefficient associated with the fundamental mode can be expressed as [17]:

$$\gamma = \frac{2}{h^2} \quad (3.4)$$

and the linear stiffness as:

$$k_1 = (2\pi f_R)^2 m_{eff} \quad (3.5)$$

The minimum Allan deviation at room temperature is 7.96×10^{-8} , and the resulting maximum mass sensitivity is 14.75 ag.

3.4 Discussion

3.4.1 Origins of multiple resonance peaks after metal coating

After metal coating, multiple resonance peaks appeared in the frequency spectrum because of the combined movement of the bridge and anchor point(s). These peaks were still evident in the hybrid devices, but their magnitude and relative position with respect to the main resonant peak changed depending on the type of printed polymeric structure. Furthermore, the thicker the IP-Dip layer, the lower the number of visible peaks.

It suggests that there was a mechanical coupling between the beam and other resonating parts such as the anchors or the SiN membranes created by the KOH undercut on either side of the bridge. Energy transfer through this coupling increased when the eigenmodes of these resonating parts and the beam were closer together. Moreover, since the polymer layer was printed all the way above the fixed ends, its shape also affected the resonant modes of the anchors.

3.4.2 Energy dissipation in hybrid devices

The quality factor of a system can be expressed as the sum of several contributions (eq. 2.8), each related to a specific damping source. However, it mainly depends on the maximal damping loss, i.e., the minimum Q-factor. The same assumptions apply in the case of a multilayer beam, where each layer composing the device contributes to the overall dissipation introducing distinct damping sources, e.g., thermoelastic, bulk friction, or surface damping.

Medium interaction damping in the hybrid device was the first analysed dissipation source. The quality factor of this damping is dependent on the pressure of the vacuum chamber in

which the device is placed: the lower the pressure, the lower the energy losses [18]. For sufficiently low pressure values, the air damping becomes negligible and the Q-factor reaches a plateau. In fig. 3.21, it is clear that the maximum Q value is reached around 10^{-2} mbar. All the measurements were performed at a high vacuum pressure of $\leq 5 \times 10^{-5}$ mbar, therefore medium interaction damping can be neglected.

A second potential dissipation source was the clamping damping. Theoretical models show that this is strictly related to the geometrical parameters of the beam, i.e., length and thickness (see eq.2.9). This means that a change in the geometry of the beam causes a change in Q. Since the thickness of the supporting SiN layer was fixed at $2 \mu\text{m}$, and different IP-Dip thicknesses also correspond to different shapes of the polymer structure, only the length variation can be considered for this study. Consequently, Q-factors of bridges with different lengths and same IP-Dip layer have been analysed. As shown in fig. 3.17, experimental results revealed a dependence of the quality factor on the beam length, but it was not monotonic as expected from the equation. On this basis, it cannot be affirmed that the anchor losses are the main dissipation source of the hybrid structure. However, they can still have a not negligible impact on the overall quality factor.

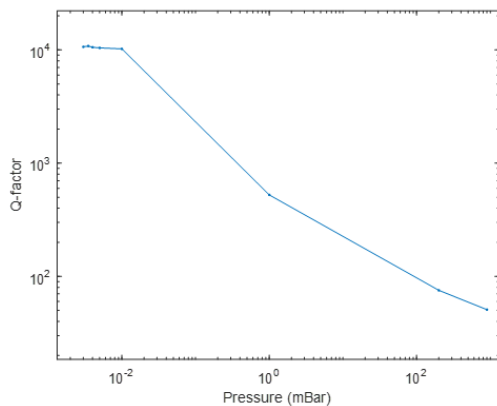


Figure 3.21. Q-factor vs chamber pressure for a $450 \mu\text{m}$ bridge with IP-Dip continuous layer.

Intrinsic damping was the last contribution to the Q-factor of the devices. It includes several damping sources such as thermoelastic damping or bulk friction damping, which are related to the geometrical, thermal and mechanical parameters of the resonator. In the case of a multilayer beam, each material composing the beam will be characterized by an intrinsic damping, expressed by its loss coefficient (η). Ceramic materials, e.g., silicon nitride, usually have a low loss coefficient, in the order of 10^{-5} ; while polymers have higher η and thus lower quality factor [13]. It follows that, in our hybrid device, intrinsic losses in the polymer were expected to be higher than in silicon nitride and to have a greater impact on the overall Q.

In order to study intrinsic damping in the hybrid resonators, Q-factor variations were analysed each time a new layer was added to the structure. An initial increase in the dissipated energy was due to the AlSi(1%) layer, which approximately halved the Q-factor of the SiN beams. As discussed in section 4.3.4, bulk friction in metals is the main source of damping, and adding even a thin metal layer strongly affects the internal losses of multilayer beams. Therefore, the quality factor of AlSi(1%) limited Q in AlSi-SiN resonators. However, the greatest impact was produced by the IP-Dip structure. The experimental results showed, indeed, that introducing a polymer layer on top of a metal-coated SiN structure decreases the quality factor even by two orders of magnitude. This implies that the quality factors related to damping in SiN and AlSi(1%) layers can be neglected, while the IP-Dip lid can be considered the main source of intrinsic losses. This assumption is also supported by the fact that an increase in the volume of printed polymer decreases Q.

A more detailed analysis of dissipation in the IP-Dip layer is carried out in chapter 4.

3.4.3 Effects of UV-light exposure

Given that IP-Dip is the main dissipation source in hybrid SMRs, reducing intrinsic losses in the polymer is the best solution to improve the quality factor of the device.

Damping in IP-Dip is usually caused by the slippage of polymeric chains against each other. The easier the chain slippage, the higher the dissipated energy. A post-development treatment of the polymer is proved to be a valid choice to reduce this phenomenon: cross-linking between chains increases and slippage reduces, thus decreasing losses [19]. Nevertheless, experimental results showed only a slight increase, or even a decrease, in the quality factors after post-development UV-light exposure. This suggests that the damping was not reduced by the supposed increase in cross-links between polymer chains. In addition, the post-development treatment lowered the quality factor for 500 and 400 μm long bridges with perpendicular printing direction and for the 450 μm long bridge with parallel printing direction.

One explanation can be the rise in surface stress at the interface between SiN and IP-Dip induced by structural changes in the polymer. Indeed, it has been noted that large surface stress can cause increases in non-linearity and energy dissipation in oscillating motion [20].

3.4.4 Comparison with the state of the art

The quality factors of the hybrid devices are significantly lower than the SiO₂ cantilever previously fabricated in the laboratory (25993 at 149.420 kHz [21]). However, they are comparable to or even exceed those of the TPP-printed polymer microbridges [7] (see fig. 3.22).

Despite the limited Q-factor, the estimated mass responsivity of the hybrid SMRs is similar to the silicon nitride device from De Pastina et al. [22] with the same channel dimensions. The maximum estimated mass sensitivity is

higher than the polymer and SiO₂ resonators fabricated by the laboratory [21, 7], but lower than the silicon devices from Manalis et al. [23]. However, temporal limitations prevented us from performing mass sensing experiments with water and demonstrating the capabilities of the device.

Further improvement could be achieved by reducing the volume of printed IP-Dip. A first solution could be to increase the channel width and decrease its height, up to the limit of manufacturing capabilities. An alternative, instead, could be to dig the channel in the SiN beam with additional cleanroom steps and cover it with a thin IP-Dip layer. These improvements will enhance the mass resolution and sensitivity by decreasing the polymer volume and increasing the quality factor.

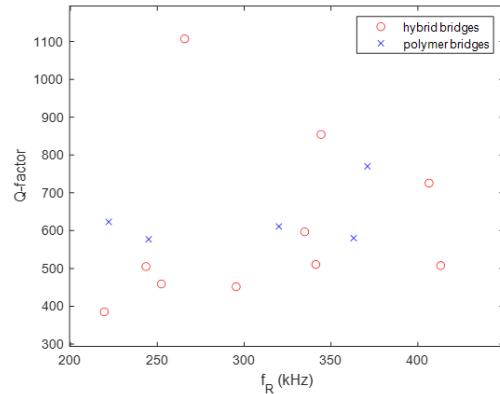


Figure 3.22. Q-factor vs resonant frequency of polymer [7] and hybrid bridges.

3.5 Conclusion

In this work, a novel fabrication method was developed for the realisation of a hybrid suspended microchannel resonator made of Si-rich SiN and IP-Dip.

The adhesion force between metal-coated silicon nitride substrate and IP-Dip was investigated, and the maximum measured pressure before delamination was found of 1.55 MPa.

The Young's modulus of IP-Dip for the chosen printing parameter was measured before and after UV-light exposure, and an increasing factor of 1.4 was calculated.

An SLA 3D-printed microfluidic interface was designed for the external fluidic connection; the design was optimized to avoid channel clogging during the printing process and to fit the fluidic interface into the AFM Nanosurf holder.

The number of cleanroom steps was minimized to a single-mask process for the fabrication of low-stress silicon nitride beams. 3D printing by two-photon polymerization was performed on suspended structures to create the IP-Dip layer of the device. Doubly clamped hybrid beams with lengths ranging from 250 to 500 μm were fabricated and their eigenfrequency and Q-factor were determined experimentally and compared to theoretical and simulated ones. The impact of printing direction, post-development treatment, and polymer volume were studied, and the optimal printed structure with separated walls was defined with a Q-factor of 510 at 341 kHz. The presence of an IP-Dip layer on top of ceramic beams proved to be the limiting factor for the performance of the device in terms of mass resolution. However, an estimated maximum mass resolution of 14.75 ag still competes with similar channel diameter SMRs made of silicon-based materials or polymers. Unfortunately, mass sensing capabilities were not proven due to temporal limitations.

The advantages of hybrid suspended microchannel resonators are the reduced manufacturing time, compared to the standard cleanroom fabrication, and the easier analysis of the frequency spectrum, compared to the all-3D-printed devices. In addition, the possibility of increasing the quality factor by reducing the volume of printed polymer offers good room for improvement for future devices.

Bibliography

- [1] In-Bok Baek et al. "Attogram mass sensing based on silicon microbeam resonators". In: *Scientific Reports* 7 (Apr. 2017). DOI: [10.1038/srep46660](https://doi.org/10.1038/srep46660) (cit. on p. 28).
- [2] Y. Kasai, Hiroshi Yabuno, T. Ishine, Y. Yamamoto, and S. Matsumoto. "Mass sensing using a virtual cantilever virtually coupled with a real cantilever". In: *Applied Physics Letters* 115 (Aug. 2019). DOI: [10.1063/1.5111202](https://doi.org/10.1063/1.5111202) (cit. on p. 28).
- [3] Joao Mouro, Bruno Tiribilli, and Paolo Paoletti. "A Versatile Mass-Sensing Platform With Tunable Nonlinear Self-Excited Microcantilevers". In: *IEEE Transactions on Nanotechnology* PP (Apr. 2018). DOI: [10.1109/TNANO.2018.2829404](https://doi.org/10.1109/TNANO.2018.2829404) (cit. on p. 28).
- [4] Thomas Burg, Amir Mirza, Nebojsa Milovic, Christine Tsau, George Popescu, John Foster, and Scott Manalis. "Vacuum-Packaged Suspended Microchannel Resonant Mass Sensor for Biomolecular Detection". In: *Microelectromechanical Systems, Journal of* 15 (Jan. 2007). DOI: [10.1109/JMEMS.2006.883568](https://doi.org/10.1109/JMEMS.2006.883568) (cit. on p. 28).
- [5] Scott Manalis. "Suspended microchannel resonators for biomolecular detection". In: (Mar. 2005), pp. 7004– (cit. on p. 28).
- [6] Thomas Burg, Michel Godin, Scott Knudsen, Wenjiang Shen, Greg Carlson, John Foster, Ken Babcock, and Scott Manalis. "Weighing of biomolecules, single cells and single nanoparticles in fluid". In: *Nature* 446 (May 2007). DOI: [10.1038/nature05741](https://doi.org/10.1038/nature05741) (cit. on p. 28).

- [7] Jikke de Winter. “Toward 3D printed suspended microchannel resonators: A study on damping and mass resolution of 3D printed microbeam resonators”. MA thesis. Delft University of Technology, 2022 (cit. on pp. 29, 38, 42).
- [8] Robert Kramer, Eleonor Verlinden, Livia Angeloni, Anita Heuvel, Lidy Fratila-Apachitei, Silvère Maarel, and Murali Ghatkesar. “Multiscale 3D-printing of Microfluidic AFM Cantilevers”. In: *Lab on a Chip* 20 (Nov. 2019). DOI: [10.1039/C9LC00668K](https://doi.org/10.1039/C9LC00668K) (cit. on p. 29).
- [9] Ada-Ioana Bunea, Nuria Iniesta, Ariadni Droumpali, Alexandre Wetzal, Einstom Engay, and Rafael Taboryski. “Micro 3D Printing by Two-Photon Polymerization: Configurations and Parameters for the Nanoscribe System”. In: *Micro* 1 (Sept. 2021). DOI: [10.3390/micro1020013](https://doi.org/10.3390/micro1020013) (cit. on p. 31).
- [10] Jens Bauer, Anna Guell Izard, Yunfei Zhang, Tommaso Baldacchini, and Lorenzo Valdevit. “Thermal Post-Curing as an Efficient Strategy to Eliminate Process Parameter Sensitivity in the Mechanical Properties of Two-Photon Polymerized Materials”. In: *Optics Express* 28 (June 2020). DOI: [10.1364/OE.395986](https://doi.org/10.1364/OE.395986) (cit. on p. 32).
- [11] Pierpaolo Belardinelli, L. Hauzer, Makars Šiškins, Murali Ghatkesar, and Farbod Alijani. “Modal analysis for density and anisotropic elasticity identification of adsorbates on microcantilevers”. In: *Applied Physics Letters* 113 (Oct. 2018). DOI: [10.1063/1.5047279](https://doi.org/10.1063/1.5047279) (cit. on pp. 33, 38).
- [12] Agustin Herrera-May, Luz Aguilera-Cortés, Pedro Garcia, Héctor Plascencia-Mora, and Miguel Torres-Cisneros. “Modeling of the intrinsic stress effect on the resonant frequency of NEMS resonators integrated by beams with variable cross-section”. In: *Microsystem Technologies* 16 (Dec. 2010). DOI: [10.1007/s00542-010-1134-5](https://doi.org/10.1007/s00542-010-1134-5) (cit. on p. 36).
- [13] M.F. Ashby. “Overview No. 80: On the engineering properties of materials”. In: *Acta Metallurgica* 37.5 (1989). DOI: [https://doi.org/10.1016/0001-6160\(89\)90158-2](https://doi.org/10.1016/0001-6160(89)90158-2) (cit. on pp. 37, 39, 41).
- [14] R Sandberg, Kristian Molhave, Anja Boisen, and Winnie Svendsen. “Effect of gold coating on the Q-factor of a resonant cantilever”. In: *Journal of Micromechanics and Microengineering* 15 (Oct. 2005). DOI: [10.1088/0960-1317/15/12/006](https://doi.org/10.1088/0960-1317/15/12/006) (cit. on p. 37).
- [15] B. Shiari and K. Najafi. “Surface effect influence on the quality factor of microresonators”. In: *2013 Transducers and Eurosensors XXVII: The 17th International Conference on Solid-State Sensors, Actuators and Microsystems (TRANSDUCERS and EUROSENSORS XXVII)*. 2013. DOI: [10.1109/Transducers.2013.6627117](https://doi.org/10.1109/Transducers.2013.6627117) (cit. on p. 37).
- [16] Tomás Manzaneque, Murali Ghatkesar, Farbod Alijani, Minxing Xu, Richard Norte, and P.G. Steeneken. “Resolution Limits of Resonant Sensors with Duffing Non-Linearity”. In: (May 2022). DOI: [10.48550/arXiv.2205.11903](https://doi.org/10.48550/arXiv.2205.11903) (cit. on p. 40).
- [17] Hidde J.R. Westra. “Nonlinear beam mechanics”. PhD thesis. Delft University of Technology, 2012 (cit. on p. 40).
- [18] Silvan Schmid, Luis Guillermo Villanueva, and Michael Roukes. *Fundamentals of Nanomechanical Resonators*.

- Jan. 2016. DOI: [10.1007/978-3-319-28691-4](https://doi.org/10.1007/978-3-319-28691-4) (cit. on p. 41).
- [19] Almut Schroer, Jens Bauer, Ruth Schwaiger, and Oliver Kraft. “Optimizing the mechanical properties of polymer resists for strong and light-weight micro-truss structures”. In: *Extreme Mechanics Letters* 8 (May 2016). DOI: [10.1016/j.eml.2016.04.014](https://doi.org/10.1016/j.eml.2016.04.014) (cit. on p. 42).
- [20] In-Bok Baek et al. “Attogram mass sensing based on silicon microbeam resonators”. In: *Scientific Reports* 7 (Apr. 2017). DOI: [10.1038/srep46660](https://doi.org/10.1038/srep46660) (cit. on p. 42).
- [21] Mehdi Daryani, Tomás Manzanque, Jia Wei, and Murali Ghatkesar. “Measuring nanoparticles in liquid with attogram resolution using a microfabricated glass suspended microchannel resonator”. In: *Microsystems and Nanoengineering* 8 (Aug. 2022). DOI: [10.1038/s41378-022-00425-8](https://doi.org/10.1038/s41378-022-00425-8) (cit. on p. 42).
- [22] Annalisa De Pastina, Damien Mailard, and Luis Guillermo Villanueva. “Fabrication of suspended microchannel resonators with integrated piezoelectric transduction”. In: *Microelectronic Engineering* 192 (Feb. 2018). DOI: [10.1016/j.mee.2018.02.011](https://doi.org/10.1016/j.mee.2018.02.011) (cit. on p. 42).
- [23] Jungchul Lee, R Chunara, W Shen, K Payer, Ken Babcock, Thomas Burg, and S Manalis. “Suspended Microchannel resonators with piezoresistive sensors”. In: *Lab on a chip* 11 (Feb. 2011). DOI: [10.1039/c0lc00447b](https://doi.org/10.1039/c0lc00447b) (cit. on p. 42).

Chapter 4

Energy dissipation analysis in hybrid multilayer double-clamped microbeams

Energy dissipation analysis in hybrid multilayer double-clamped microbeams

In this study, an analysis of the main damping mechanisms of resonant multilayer double-clamped microbeams in a frequency range from 200 kHz to 500 kHz is presented. The suspended structures consist of 2 μm thick Si-rich silicon nitride supporting beams, sputtered with 30 nm of AlSi(1%) and covered with an IP-Dip unconstrained layer realised by means of two-photon polymerization technique. The influence of clamping and intrinsic damping mechanisms in IP-Dip was investigated by varying the thickness and anchor width of the viscoelastic layer. A laser-Doppler vibrometer was used to measure the vibration of both bare SiN and multilayer resonators in high vacuum at room temperature. The measured eigenfrequencies were compared with the theoretical results and the finite element method (FEM). Through an analysis of the experimental quality factors, the intrinsic damping was proved to be the dominant dissipation source. A simplified model of the intrinsic dissipation was formulated and an evaluation of the frequency-dependent loss factor of IP-Dip was performed.

Index terms – Multilayer double-clamped microbeams, Polymer layer, Resonant frequency, Damping, Loss factor.

4.1 Introduction

Micro-electromechanical systems (MEMS) rely on the use of ceramic materials as structural materials [1]. Thanks to their significant advantages in terms of fabrication and material properties, these materials are suitable for the production of low-loss and little-fatigue sub-micrometer structures [2, 1]. Polymers, instead, have always been employed in the lithographic steps during the fabrication of MEMS, but they have not played an active role in the actuation or sensing mechanism. However, with the introduction of additive manufacturing techniques such as two-photon polymerization (TPP), polymer materials can be directly 3D-structured to be converted or integrated into MEMS devices. This is also the case of sensing resonant structures. So far, hybrid resonating beams combining polymer and ceramic materials have been employed for chemical sensing based on high Q-silicon cantilevers covered

with a functional polymer layer [3]. Furthermore, TPP-printed polymeric structures have been added to cantilevers to tune their resonance spectrum by modifying their dynamical properties [4].

In this scenario, an investigation of the dissipation in multilayer microresonators including a viscoelastic material (VEM) is of great interest. Indeed, energy losses in ceramic microbeams have been thoroughly investigated [5, 6, 7, 8]. The same applies to damping in polymer microbeams [9, 10]. On the other hand, microbeams combining ceramic and VEM still need simple methods describing their dynamics. The aspect of the understanding of the main dissipation mechanisms in multilayer microresonators and their impact on the overall quality factors is the subject of this work. In this regard, the damping mechanisms of multilayer double-clamped microbeams made of AlSi(1%) sputtered Si-rich silicon nitride and IP-Dip polymer were investigated. Different thicknesses and anchor geometries of the VEM

were chosen to study the intrinsic and clamping dissipation; while diverse beam lengths enabled the measurement of quality factors over a range of frequencies.

4.2 Fabrication

Double-clamped 2 μm thick Si-rich silicon nitride beams were fabricated by a single-mask photolithographic process followed by KOH etching for beam release. The reflectivity of the beams was increased by sputtering a 30 nm thick AlSi(1%) layer. An IP-Dip structure was patterned by TPP on top of each beam. Table 4.1 shows the dimensions of SiN and IP-Dip layers.

Parameter	Value [μm]
SiN length	250 - 500
SiN width	50
IP-Dip thickness	0.5 - 5
IP-Dip length	270 - 520
IP-Dip width	43

Table 4.1. Dimensions of the devices.

Two different IP-Dip structures have been printed on top of the SiN beams. A layer with variable width at the anchor points and fixed thickness of 1 μm (fig. 4.1) was employed to perform experiments on clamping damping; while a layer with constant width and variable thickness was used to carry out experiments on internal friction.

4.3 Experimental setup

The resonating structures were oscillated by using a piezoelectric external actuator. The vibration was monitored with an MSA-400-PM2-D Laser Doppler vibrometer equipped with an MSA-A-M20X lens operated in a frequency range from 0 to 2 MHz and with a voltage amplitude from 1 to 3 V. All measurements were

performed in high vacuum ($p < 5 \times 10^{-4}$ mbar) to eliminate air damping.

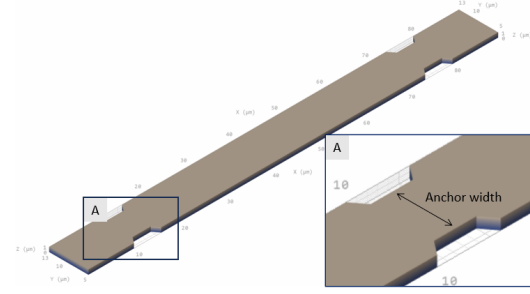


Figure 4.1. Design of the IP-Dip structure with variable width at the anchors.

4.4 Results and discussion

4.4.1 Metal coated SiN beams

Table 4.2 shows the comparison of analytical and experimental fundamental frequency for different beam lengths l . The analytical results were obtained by taking into account an intrinsic stress of 237 MPa in the silicon nitride layer [11] and excluding the contribution of the AlSi(1%) coating. The thin metal layer has indeed a negligible impact on the resonant frequency (less than 1% frequency shift). The loss factor η was calculated from the experimental quality factor Q as $\eta=1/Q$.

l [μm]	Th [kHz]	Ex [kHz]	η [10^{-4}]
250	685.0	606.0 \pm 2.6	2.0
300	554.0	486.9 \pm 1.1	1.6
350	466.1	407.1 \pm 2.3	4.2
400	402.8	348.8 \pm 3.3	2.9
450	355.0	305.1 \pm 2.6	2.0
500	317.5	271.4 \pm 2.2	1.7

Table 4.2. Comparison of analytical (Th) and experimental (Ex) frequencies of AlSi(1%) sputtered SiN beams.

The main damping source in bare silicon nitride resonators was proved to be thermoelastic

damping (TED) [12, 13]. However, the presence of a 30 nm thick AlSi(1%) layer cannot be neglected in the damping analysis. Soft metals are characterised by high internal friction and this occurs for even extremely thin coatings [14]. In addition, sub-micrometer thick layers exhibit high surface friction loss due to roughness, impurities, and adsorbates on the surface [15]. It follows that the overall damping in AlSi-SiN beams is a combination of TED in the ceramic material and friction in the metal coating.

4.4.2 Beams with IP-Dip layer

Clamping damping study

Clamping damping in resonant microbeams is strictly related to the anchor shape and beam geometry. In particular, the lower the constraint of the beams, the lower the energy dissipated [16]. This relationship, expressed by eq. 2.9, states that a change in the beam length or anchor shape will produce a variation in the quality factor. Under this assumption, the beam length and the anchor width of the VEM were ranged to investigate their impact on the quality factor of the multilayer structure.

Table 4.3 lists the resonant frequencies measured by varying the polymer width at the anchors. Effective stiffness and mass variation due to the width change have been neglected, since the related frequency errors are lower than 1%.

l [μm]	Ex [kHz]	Error
250	539.6	0.67%
300	440.8	0.39%
350	368.1	0.27%
400	318.0	0.41%
450	279.0	0.86%
500	247.5	0.97%

Table 4.3. Experimental (Ex) fundamental frequencies of multilayer beams.

The experimental quality factors are reported in fig. 4.2. The curves show no clear trend, but a random variation of Q with the anchor width and beam length. It suggests that, although anchor losses can affect the overall quality factor, they are not the dominant damping.

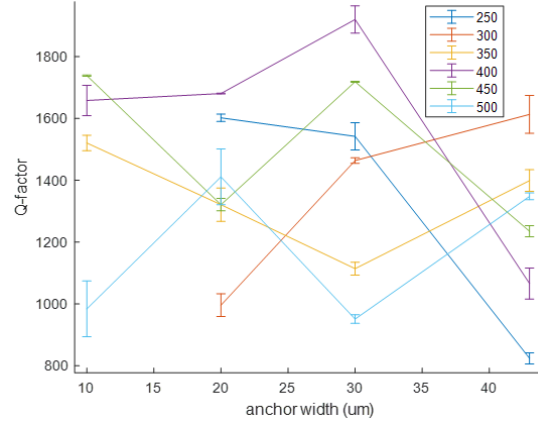


Figure 4.2. Q -factor vs IP-Dip layer width at the anchors for different beam lengths.

Intrinsic damping study

In order to study the intrinsic dissipation in the multilayer structure, the volume of the polymer layer was varied for several beam lengths by ranging its thickness.

The analytical, simulated and experimental frequencies of multilayer beams with variable IP-Dip thickness are shown in fig. 4.3. Simulation and theoretical results exhibit an error within 20% when compared to the experimental values. This is to be attributed to the manufacturing error, i.e., photolithography using foil mask, and KOH over-etching. The measured quality factors are shown in fig. 4.4. It is clear that energy loss increases with increasing IP-Dip volume. Energy dissipation in the viscoelastic structure is indeed due to the extension and compression of the layer, which causes internal friction. The greater the VEM volume, the greater the energy dissipated by friction.

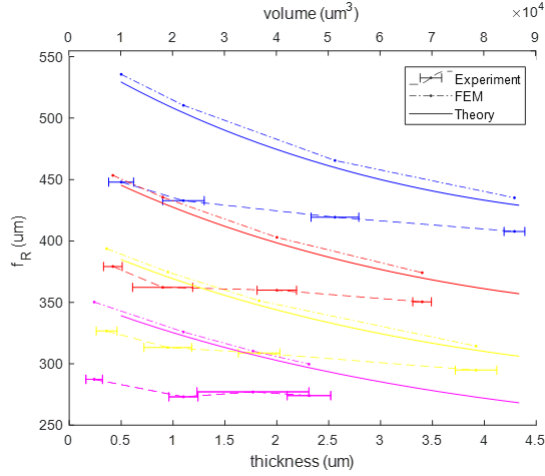


Figure 4.3. Resonant frequency vs IP-Dip thickness and volume for beam lengths of 300 μm (blue), 350 μm (red), 400 μm (yellow), and 450 μm (magenta).

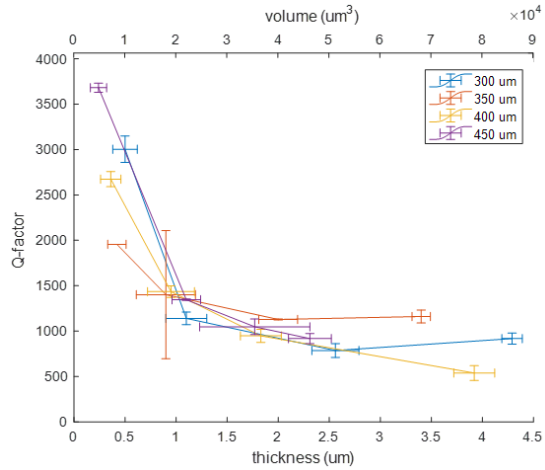


Figure 4.4. Q -factor vs polymer thickness and volume for different beam lengths.

However, predicting dissipation in a multi-layer structure with a polymer layer is a challenging task. This is because the loss factor of a VEM varies significantly as a function of the frequency. In this regard, a simplified model of the intrinsic dissipation in an unconstrained IP-Dip layer as a function of frequency and polymer volume has been formulated. It is based on experimental results and FEM simulations. The FEM model studied the eigenfrequencies

of a two-layer double-clamped beam made of IP-Dip and SiN. The mechanical parameters of the materials are listed in table A.1 and a more detailed explanation of the model is presented in annex A.7. An effective Young's modulus Y_{eff} has been calculated for silicon nitride to take into account the intrinsic stress of the layer. Its value is obtained from eq. 4.1 [11].

$$Y_{eff} = Y \left[1 + 0.295 \left(\frac{l}{t} \right)^2 \frac{\sigma}{Y} \right] \quad (4.1)$$

where l is the beam length, t is the SiN layer thickness, σ is the measured intrinsic stress, and Y is the Young's modulus of the material.

Intrinsic damping in each layer is included through the loss factor η of the material. Experimental η values, shown in table 4.2, are used for the SiN layer. The frequency dependence of η of the VEM has been studied by performing a parametric sweep on the IP-Dip loss factor for each beam length; then, a different η for each length has been selected so as to match the experimental results. The chosen loss factors as a function of frequency are shown in fig.4.5. The empirical model, derived from fitting the FEM results, is expressed by equation 4.2:

$$Q = \frac{1}{(af_R + b)(twl)^2} \quad (4.2)$$

where a and b are two constant respectively of $9.495 \times 10^{18} \text{m}^{-6} \text{Hz}^{-1}$ and $-1.464 \times 10^{24} \text{m}^{-6}$, f_R is the fundamental resonant frequency, t is the VEM thickness, w is its width, and l its length. The constants a and b incorporates the effective elastic modulus and Poisson's ratio of the multilayer beam and the polymer viscoelasticity.

Fig. 4.6 shows the comparison of Q obtained from experiments, simulations and empirical model for different beam lengths and the results match very well for IP-Dip thicknesses lower than 1.5 μm .

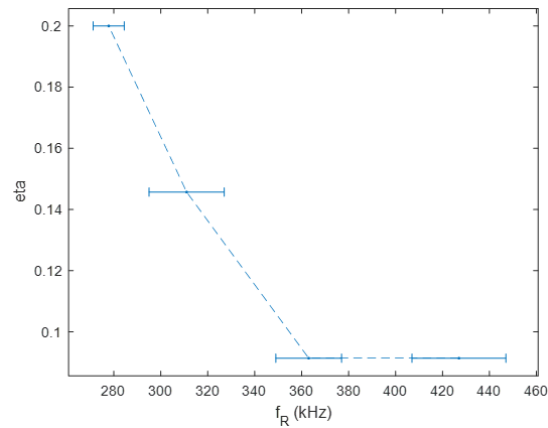


Figure 4.5. Frequency-dependent loss factor used in FEM simulations.

4.5 Conclusions

The quality factors of double-clamped microbeams with an unconstrained IP-Dip layer were measured and the corresponding damping mechanisms were investigated. After excluding clamping damping as a potential dominant damping mechanism, it was shown that dissipation is mainly related to intrinsic losses in the VEM. Plotting the experimental quality factors against the IP-Dip thickness revealed that energy loss depends on both frequency and polymer volume. This relationship can be expressed by a simplified empirical model valid for IP-Dip thicknesses lower than 1.5 μm .

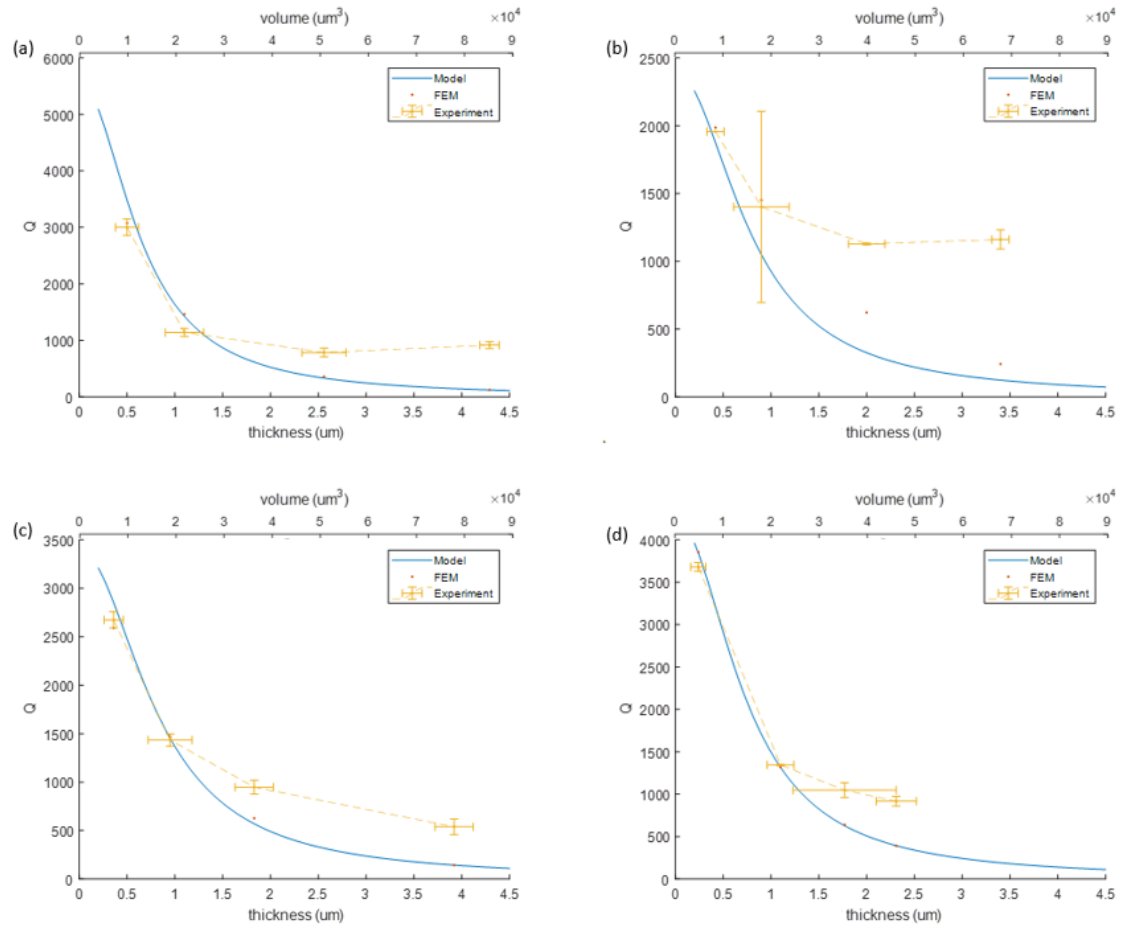


Figure 4.6. Q -factor as a function of IP-Dip thickness and volume for beam lengths of (a) 300 μm , (b) 350 μm , (c) 400 μm , and (d) 450 μm obtained from the empirical model, FEM simulations and experiments.

Bibliography

- [1] Hany Hassanin, Khamis Essa, Amr Elshaer, Mohamed Imbaby, Heba El-Mongy, and Tamer El-Sayed. “Micro-fabrication of ceramics: Additive manufacturing and conventional technologies”. In: *Journal of Advanced Ceramics* 10 (Feb. 2021). DOI: [10.1007/s40145-020-0422-5](https://doi.org/10.1007/s40145-020-0422-5) (cit. on p. 48).
- [2] Markku Tilli and Atte Haapalinna. “Chapter One - Properties of Silicon”. In: *Handbook of Silicon Based MEMS Materials and Technologies*. Ed. by Veikko Lindroos, Markku Tilli, Ari Lehto, and Teruaki Motooka. Micro and Nano Technologies. Boston: William Andrew Publishing, 2010. DOI: <https://doi.org/10.1016/B978-0-8155-1594-4.00001-2> (cit. on p. 48).
- [3] Felice Battiston, Jean-Pierre Ramseyer, Hans Lang, Marko Baller, Ch Gerber, James Gimzewski, Ernst Meyer, and H.-J Èntherodt. “A chemical sensor based on a microfabricated cantilever array with simultaneous resonance-frequency and bending readout”. In: *Sensors and Actuators B: Chemical* 77 (June 2001). DOI: [10.1016/S0925-4005\(01\)00683-9](https://doi.org/10.1016/S0925-4005(01)00683-9) (cit. on p. 48).
- [4] Gerald Göring, Philipp-Immanuel Dietrich, Matthias Blaicher, Swati Sharma, Jan Korvink, Thomas Schimmel, Christian Koos, and Hendrik Hölscher. “Tailored probes for atomic force microscopy fabricated by two-photon polymerization”. In: *Applied Physics Letters* 109 (Aug. 2016). DOI: [10.1063/1.4960386](https://doi.org/10.1063/1.4960386) (cit. on p. 48).
- [5] Luis Guillermo Villanueva and Silvan Schmid. “Evidence of Surface Loss as Ubiquitous Limiting Damping Mechanism in SiN Micro- and Nanomechanical Resonators”. In: *Physical Review Letters* 113 (Nov. 2014). DOI: [10.1103/PhysRevLett.113.227201](https://doi.org/10.1103/PhysRevLett.113.227201) (cit. on p. 48).
- [6] Rob Mihailovich and N. MacDonald. “Dissipation measurements of vacuum-operated single-crystal silicon microresonators”. In: *Sensors and Actuators A-physical - SENSOR ACTUATOR A-PHYS* 50 (Sept. 1995), pp. 199–207. DOI: [10.1016/0924-4247\(95\)01080-7](https://doi.org/10.1016/0924-4247(95)01080-7) (cit. on p. 48).
- [7] Jinling Yang, Takahito Ono, and Masayoshi Esashi. “Energy dissipation in submicrometer thick single-crystal silicon cantilevers”. In: *Microelectromechanical Systems, Journal of* 11 (Jan. 2003), pp. 775–783. DOI: [10.1109/JMEMS.2002.805208](https://doi.org/10.1109/JMEMS.2002.805208) (cit. on p. 48).
- [8] Kevin Yasumura, Timothy Stowe, E.M. Chow, Timothy Pfafman, Thomas Kenny, Barry Stipe, and Daniel Rugar. “Quality factor in micron- and submicron-thick cantilevers”. In: *Microelectromechanical Systems, Journal of* 9 (Apr. 2000), pp. 117–125. DOI: [10.1109/84.825786](https://doi.org/10.1109/84.825786) (cit. on p. 48).
- [9] Stefan Schmid and C. Hierold. “Damping mechanisms of single-clamped and prestressed double-clamped resonant polymer microbeams”. In: *Journal of Applied Physics* 104 (Dec. 2008), pp. 093516–093516. DOI: [10.1063/1.3008032](https://doi.org/10.1063/1.3008032) (cit. on p. 48).
- [10] Silvan Schmid. “Electrostatically Actuated All-Polymer Microbeam Resonators—Characterization and Application”. In: Jan. 2009 (cit. on p. 48).
- [11] Agustin Herrera-May, Luz Aguilera-Cortés, Pedro Garcia, Héctor Plascencia-Mora, and Miguel Torres-Cisneros. “Modeling of the intrinsic stress effect on the resonant frequency of NEMS resonators integrated by beams with

- variable cross-section". In: *Microsystem Technologies* 16 (Dec. 2010). DOI: [10.1007/s00542-010-1134-5](https://doi.org/10.1007/s00542-010-1134-5) (cit. on pp. 49, 51).
- [12] Jinling Yang, Takahito Ono, and Masayoshi Esashi. "Energy dissipation in submicrometer thick single-crystal silicon cantilevers". In: *Microelectromechanical Systems, Journal of* 11 (Jan. 2003). DOI: [10.1109/JMEMS.2002.805208](https://doi.org/10.1109/JMEMS.2002.805208) (cit. on p. 50).
- [13] Kevin Yasumura, Timothy Stowe, E.M. Chow, Timothy Pfafman, Thomas Kenny, Barry Stipe, and Daniel Rugar. "Quality factor in micron- and submicron-thick cantilevers". In: *Microelectromechanical Systems, Journal of* 9 (Apr. 2000). DOI: [10.1109/84.825786](https://doi.org/10.1109/84.825786) (cit. on p. 50).
- [14] R Sandberg, Kristian Molhave, Anja Boisen, and Winnie Svendsen. "Effect of gold coating on the Q-factor of a resonant cantilever". In: *Journal of Micromechanics and Microengineering* 15 (Oct. 2005). DOI: [10.1088/0960-1317/15/12/006](https://doi.org/10.1088/0960-1317/15/12/006) (cit. on p. 50).
- [15] Silvan Schmid, Luis Guillermo Villanueva, and Michael Roukes. *Fundamentals of Nanomechanical Resonators*. Jan. 2016. DOI: [10.1007/978-3-319-28691-4](https://doi.org/10.1007/978-3-319-28691-4) (cit. on p. 50).
- [16] Siavash Pourkamali, Akinori Hashimura, Reza Abdolvand, Gavin Ho, Ahmet Erbil, and Farrokh Ayazi. "High-Q single crystal silicon HARPSS capacitive beam resonators with self-aligned sub-100-nm transduction gaps". In: *Microelectromechanical Systems, Journal of* 12 (Sept. 2003). DOI: [10.1109/JMEMS.2003.811726](https://doi.org/10.1109/JMEMS.2003.811726) (cit. on p. 50).

Chapter 5

Conclusion

In this work, a novel fabrication method has been developed for the realisation of a hybrid suspended microchannel resonator made of Si-rich SiN and IP-Dip. The adhesion force between metal-coated silicon nitride substrate and IP-Dip was investigated, and the maximum measured pressure before delamination was found of 1.55 MPa. The Young's modulus of IP-Dip was measured before and after UV-light exposure, and an increasing factor of 1.4 was calculated. An SLA 3D-printed microfluidic interface was designed for the external fluidic connection; the design was optimized to avoid channel clogging during the printing process and to fit the fluidic interface into the AFM Nanosurf holder. The number of cleanroom steps was minimized to a single-mask process for the fabrication of low-stress silicon nitride beams. 3D printing by two-photon polymerization was performed on suspended structures to create the IP-Dip layer of the device. Double-clamped hybrid beams with length ranging from 250 to 500 μm were fabricated and their eigenfrequency and Q-factor was determined experimentally and compared to theoretical and simulated ones. The impact of printing direction, post-development treatment, and polymer volume has been studied, and the optimal printed structure has been defined with a Q-factor of 510 at 341 kHz.

In order to define the main damping sources in hybrid devices with an unconstrained polymer layer, the quality factors of double-clamped microbeams with different lengths were measured before and after 3D printing. After excluding clamping damping as a potential dominant damping mechanism, it was shown that dissipation is mainly related to intrinsic losses in the polymer. Plotting the experimental quality factors against the IP-Dip thickness revealed that energy loss depends on both frequency and polymer volume. This relationship has been expressed by a simplified empirical model valid for IP-Dip thicknesses lower than 1.5 μm .

An estimated maximum mass resolution of 14.75 ag was obtained for hybrid SMRs. Unfortunately, mass sensing capabilities have not been proven due to temporal limitations. The advantages of hybrid suspended microchannel resonators are the reduced manufacturing time, compared to the standard cleanroom fabrication, and the easier analysis of the frequency spectrum, compared to the all-3D-printed devices. In addition, the possibility of increasing the quality factor by reducing the volume of printed polymer offers good room for improvement for future devices.

Appendix A

FEM simulation of the hybrid device

Finite Element Method (FEM) simulations were carried out in order to define the mechanical properties of the hybrid structure and investigate the static and dynamic behaviour of the device relative to a series of parameter tweaks. In particular, a first study on the cantilever stiffness was performed, followed by a second study on the resonant frequency with and without the IP-Dip layer. Then a gold proof mass was applied to the suspended structure to calculate the mass responsivity without liquid inside the channel. Fluid was introduced inside the channel to investigate the impact of flow rate, density, and viscosity on the device, both in static and dynamic mode. Finally, the intrinsic dissipation in multilayer doubly clamped beams was studied by considering the theoretical intrinsic loss coefficient of silicon nitride and IP-Dip polymer.

All the mechanical properties of the materials used for the simulation are listed in table [A.1](#).

Material	Density [kg/m ³]	Young's modulus [GPa]	Poisson's ratio
Silicon Nitride	3100	250	0.23
IP-Dip	1200	2.5	0.35
Gold	19300	70	0.44

Table A.1. Mechanical properties of the materials used in COMSOL simulations.

A.1 Stiffness of the silicon nitride cantilever

As a first step, the stiffness of the silicon nitride cantilevers was studied. A stiffness value of a few hundred mN/m is required, so as to avoid the stiction of the beam during the cleaning procedures and to guarantee a low deformation of the support once the polymeric lid is printed.

The study was carried out by using the Solid Mechanics module in COMSOL Multiphysics. The stiffness of the silicon nitride cantilever was investigated in relation to several parameters, i.e., length, width, and thickness of the layer.

The design employed in the FEM analysis is a U-shaped microcantilever made of silicon nitride. A fixed constraint is applied at the ends of the cantilever connected to the silicon chip, to simulate the anchoring to the substrate; while a point load is placed on the free end of the beam. A stationary study allowed to calculate the deformation of the beam as a function of the applied force.

Results from simulations are given in figure A.1.

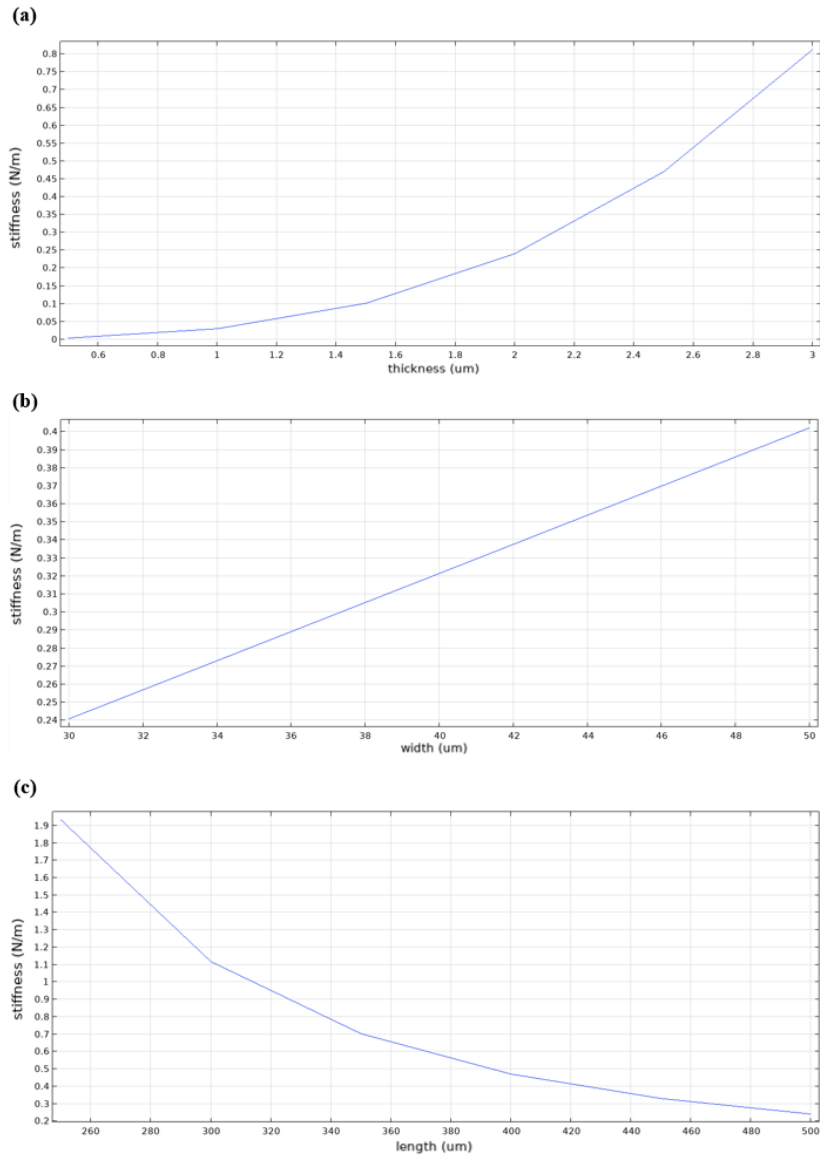


Figure A.1. Variation of the stiffness in silicon nitride cantilevers depending on (a) thickness, (b) width and (c) length. In each simulation, the invariant parameters were fixed to 500 μm for the length, 30 μm for the width, and 2 μm for the layer thickness.

Each study was performed by varying only one of the three parameters (i.e., width, length, and

thickness) and maintaining the other two fixed at a value that simulates the worst-case scenario. Displayed values are related to the maximum displacement point, placed at the free end of the cantilever.

As predicted from the theoretical Euler-Bernoulli beam equation (eq. A.1), stiffness increases quasi-linearly with width, decreases with increasing length and increases with thickness.

$$k = \frac{Ywt^3}{12l^3} \quad (\text{A.1})$$

where Y is the Young's modulus of the material, w is the width of the beam, t its thickness, and l its length.

As illustrated in the graphs, a thickness of 2 μm is sufficient to reach a stiffness higher than 0.1 N/m for all cantilever lengths. It follows that a silicon nitride layer of 2 μm is thick enough to avoid stiction during cleaning and deflection after 3D printing.

A.2 Resonant frequency of the hybrid device

Adding a second layer to the silicon nitride supporting beam results in a multi-layered resonating beam. As a consequence, the resonant frequency varies with respect to that of the silicon nitride support due to the added mass and to the variation of the overall Young's modulus and moment of inertia. The shift in frequency can be positive or negative depending on the impacts on the effective spring constant and effective mass of the beam.

A.2.1 Frequency study of multilayered clamped beams

In order to study how the polymeric layer affects the frequency behaviour, as a first approach, a simplified model of the multi-layered beam was considered. The original U-shaped device is substituted by a clamped beam of 250 μm length including two layers, made of two different materials: the top layer, in IP-Dip, is 20 μm width and 8 μm thick; the bottom layer, in silicon nitride, is 30 μm width and 2 μm thick. The presence of the embedded channel of 10 μm width is simulated by reducing the IP-Dip width by 10 μm with respect to the silicon nitride layer; while the lid of the channel is introduced by increasing the IP-Dip thickness of 1 μm .

As a first step, the shift in resonant frequency is calculated starting from the theoretical equation for a multilayer beam [1]. In order to obtain the natural frequency with the IP-Dip layer, it is necessary to calculate the new values of Young's modulus Y and moment of inertia I , which depend on the length l , width w , thickness h , and density ρ of the i th layer.

The moment of inertia of the i th layer I_i calculated with respect to the neutral axis of the beam is given by the equation A.2

$$I_i = \frac{w_i[(z_i - z_c)^3 - (z_{i-1} - z_c)^3]}{3} \quad (\text{A.2})$$

where z_i is the height of the i th layer and z_c is the height of the neutral axis, both with respect to the bottom of the beam.

The height of the i th layer z_i with respect to the bottom of the cantilever ($z_0 = 0$) is obtained from the equation A.3.

$$z_i = \sum_{k=1}^i h_k \quad (\text{A.3})$$

The distance of the neutral axis from the bottom of the beam is z_c , given by the equation A.4.

$$z_c = \frac{\sum_{i=1}^n Y_i w_i (z_i^2 - z_{i-1}^2)}{2 \sum_{i=1}^n Y_i w_i (z_i - z_{i-1})} \quad (\text{A.4})$$

The overall bending stiffness \overline{YI} and linear density $\overline{\rho A}$ of the beam are expressed in equation A.5 and A.6, respectively.

$$\overline{YI} = \sum_{k=1}^n Y_k I_k = Y_{SiN} I_{SiN} + Y_{IP-Dip} I_{IP-Dip} \quad (\text{A.5})$$

$$\overline{\rho A} = \sum_{k=1}^n \rho_k A_k = \rho_{SiN} A_{SiN} + \rho_{IP-Dip} A_{IP-Dip} \quad (\text{A.6})$$

where A is the cross-section area of the i th layer.

The natural frequency is given by equation A.7.

$$f_1 = \frac{1.875^2}{2\pi l^2} \sqrt{\frac{\overline{YI}}{\overline{\rho A}}} \quad (\text{A.7})$$

The calculated results for the single layer beam (in silicon nitride) and multilayer beam (in silicon nitride and IP-Dip) are respectively 46.416 kHz and 59.814 kHz. This means that the presence of the polymeric layer causes a positive frequency shift of 13.398 kHz.

The theoretical results are compared to simulated values, obtained from an Eigenfrequency study in COMSOL Multiphysics. The resulting resonant frequency of the silicon nitride beam is equal to 46.647 kHz; while that of the multilayer cantilever is 61.161 kHz. The calculated shift in frequency is 14.514 kHz. Both analytical and simulated results show a positive frequency shift, with a simulation error of 8.3%.

A.2.2 Frequency study of hollowed structures

The analysis of the simplified structure served as a starting point for the study of the more complex U-shaped cantilever and hollowed bridge. In this case, a simple FEM simulation is carried out to determine the frequency shift.

Investigated devices are shown in figure A.2; parameters used for the simulation are listed in table A.2.

An Eigenfrequency study is performed in COMSOL Multiphysics to obtain the eigenvalues. For the simulation without the IP-Dip lid, the polymeric structure with the embedded channel is disabled, and only the remaining silicon nitride support is studied.

The resulting values of the resonant frequencies for the first three resonant modes are illustrated in table A.3.

As predicted by the preliminary study on the simplified structure, considering a 7 μm thick lid with Young's modulus of 2.5 GPa, the frequency shift due to the addition of IP-Dip is positive.

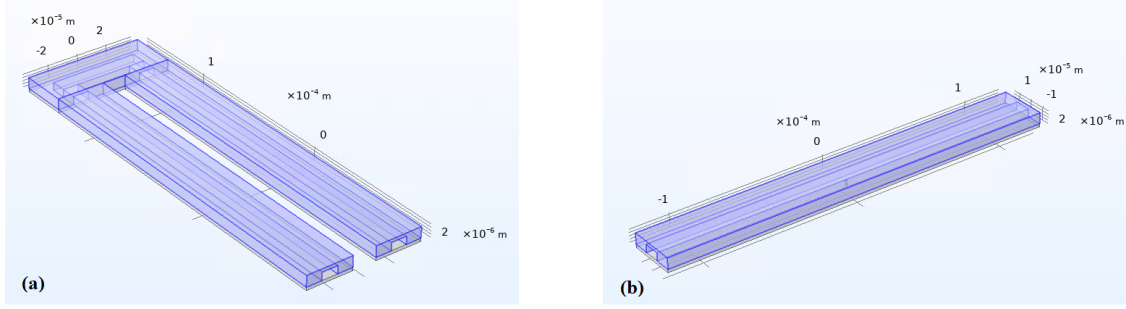


Figure A.2. Model of (a) cantilever and (b) bridge with the IP-Dip layer in blue and Silicon nitride layer in grey.

Parameter	Value
Beam length	250 μm
Beam width	30 μm
SiN thickness	2 μm
IP-Dip thickness	7 μm
Channel section	5 μm x 10 μm

Table A.2. Parameters used in the COMSOL simulation.

Mode	Cantilever		Bridge	
	SiN	SiN + IP-Dip	SiN	SiN + IP-Dip
1	44.446	50.581	297.99	376.62
2	251.59	264.51	821.03	1061.7
3	283.97	325.32	1594.5	1687.9

Table A.3. Eigenfrequencies in kHz of cantilever and bridge for the first three resonant modes.

However, a small variation of thickness or Young's modulus of the polymeric layer produces a considerable frequency variation. The impact of Young's modulus and thickness on the resonant frequency of the U-shaped cantilever for the first resonant mode is shown in figure A.3. For this simulation, the hollowed lid has been substituted by an equivalent compact IP-Dip layer 5.243 μm thick.

In conclusion, the effect of the polymeric lid placed on the silicon nitride supporting beam is defined by the effective spring constant and the effective mass of the beam. In particular, in the case of a 7 μm thick IP-Dip layer with Young's modulus of 2.5 GPa, the variation in the overall bending stiffness is greater than that in the linear mass density. This entails an increased resonant

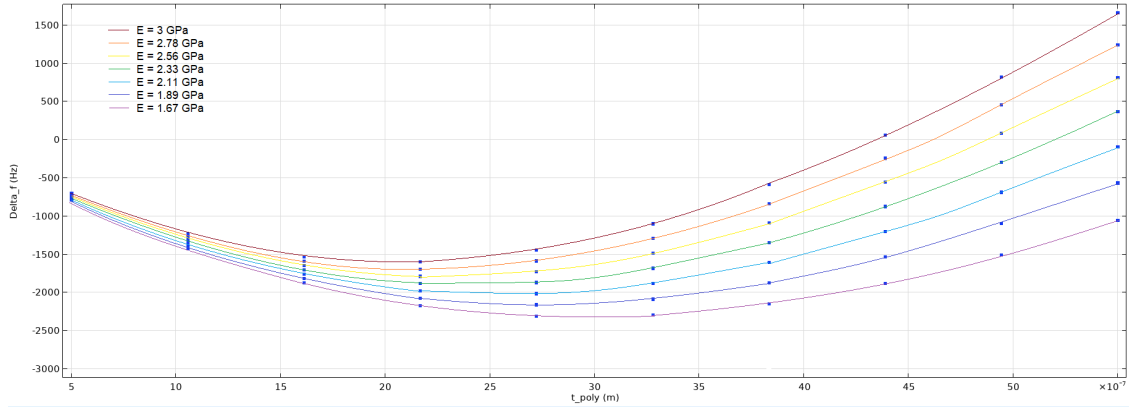


Figure A.3. Shift of the natural frequency as a function of IP-Dip thickness for different Young' modulus.

frequency when switching from a single to two-layer resonant device.

A.3 Mass responsivity of empty beams in vacuum

Mass responsivity is one of the most significant parameters that define the performance of a mass sensor. It represents the change of resonance frequency as a result of changes in mass and is an indicator of the resonator sensitivity.

In order to calculate the mass responsivity of hollowed clamped and clamped-clamped beams in vacuum environment and without any liquid inside the embedded channel, an Eigenfrequency study using Solid Mechanics in COMSOL Multiphysics was performed. The simulated structures are shown in figure A.2, and the reference parameters are listed in table A.2.

The proof mass applied to the beams is a cubic gold particle. The mass is located inside the channel: it is positioned at the free end of the beam, in the case of cantilevers, and in the middle, in the case of bridges.

To simulate the frequency variation as a function of the proof mass, a parametric sweep is performed: the cube side is swept from $0.5 \mu\text{m}$ to $1 \mu\text{m}$, which corresponds to a mass range from 19.3 fg to 2.4 ng . The mass responsivity will be the slope of the curve in the frequency vs. mass plot.

The resulting graphs for the cantilever and bridge are illustrated in figure A.4(a) and A.4(b), respectively. The calculated mass responsivity is 457.7 mHz/pg for the cantilever and 4265.5 mHz/pg for the bridge.

The mass responsivity of the bridge is one order of magnitude greater than that of the U-shaped cantilever. This is due to the higher resonant frequency of the clamped-clamped beams. In fact, assuming a constant stiffness of the resonant structure, it can be observed that the higher the frequency the better the mass responsivity (see equation 2.4).

The result obtained for the cantilever is approximately two times smaller than the measured values for SMRs with similar size but entirely made of silicon nitride [2]. These devices reach a higher mass responsivity (up to $1125 \pm 0.06 \text{ mHz/pg}$) thanks to the higher resonant frequency

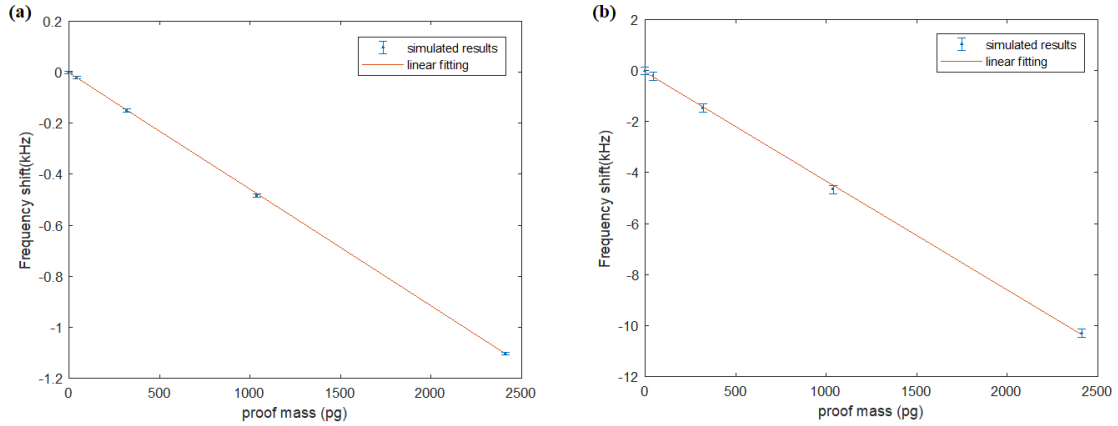


Figure A.4. Frequency shift as a function of the proof mass in empty (a) cantilever and (b) bridge.

(203.901 ± 0.02 kHz).

A.4 Flow-induced deformation

Fluids flowing inside the embedded channel of the SMR are characterised by a certain flow momentum that generates forces depending on the bending of the channel. When the microchannel is on the neutral plane of the cantilever, and the inlet and outlet are in the same plane, the flow forces act perpendicular to the preferential direction of deflection of the microcantilever (figure A.5(a)), and the produced deformation is lateral. Conversely, when the microchannel is orthogonal to the microcantilever plane and the inlet and outlet are on different planes, the forces generated by the flow act in the vertical direction (figure A.5(b) and (c)), causing the vertical deflection of the beam.

As illustrated in figure A.5(d), the direction of deflection also depends on the position of the channel with respect to the neutral axis of the beam [3]. The off-axis channel placement produces a vertical deflection that increases with the distance from the neutral axis.

As regards the magnitude of the cantilever deflection, this is related to the flow rate and liquid dynamic viscosity. In particular, deflection linearly increases with increased flow rate and dynamic viscosity.

Using the 'Fluid-Structure Interaction' (FSI) module in COMSOL Multiphysics, the deformation of the hybrid cantilever is investigated relative to a series of parameter tweaks [4]. Specifically, a flow rate analysis is carried out in order to study the effects of the flow forces generated by fluids flowing through the embedded microchannel. In addition, the flow of liquids with different densities and viscosities is simulated, so as to analyse the impact of these parameters on the cantilever's behaviour.

The design employed in the FEM analysis is shown in figure A.6(a). It is characterised by a U-shaped microcantilever made of silicon nitride with an IP-Dip polymeric lid. The suspended structures is through along its entire length by a microfluidic channel with a rectangular section. All the design parameters are listed in table A.4.

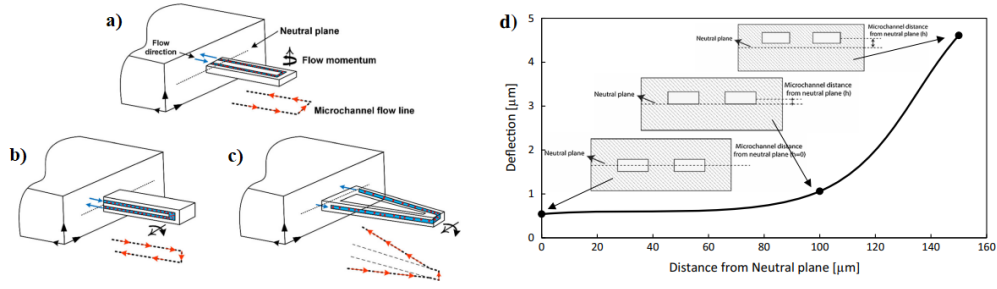


Figure A.5. Schematic of three different models of hollowed cantilever [4]: (a) microchannel with inlet and outlet on the neutral plane of the cantilever; (b) and (c) microchannel is orthogonal to the microcantilever plane. (d) Cantilever vertical deflection as a function of the off-axis displacement [3].

Parameter	Value
Cantilever length	500 μm
Cantilever width	50 μm
SiN thickness	2 μm
Channel section	5 μm x 10 μm

Table A.4. Parameters used in the COMSOL simulation.

The device includes two layers, made of two different materials: the top layer, in IP-Dip, which houses the embedded microchannel, and the bottom layer, in silicon nitride, acting as a support for the deformable polymer. The inlet and the outlet of the channel are set on the same x-y plane, in the middle of the device, but are placed off-axis with respect to the silicon nitride beam, and so with respect to the resonating structure. In fact, although the channel is perfectly centered between the two layers, it cannot be considered on the neutral axis of the cantilever. This is due to the different Young's moduli of the materials: the silicon nitride support shows a Young's modulus a hundred times larger than the IP-Dip structure.

In the simulation, fluid domain (embedded microchannel) and solid domain (cantilever body) interact influencing each other: the flow forces cause a displacement of the cantilever, and, at the same time, the deformation of the cantilever affects the flow.

As regards the Flow physics, the liquid flow was set as laminar and fully developed at the inlet, with a positive constant velocity defining the flow rate. The pressure was set with zero at the outlet, and the walls were set with no-slip/penetration conditions. As regards the Solid Mechanics physics, it deals with the deformation of the cantilever body, which is subject to the flow forces and shows stress.

A moving-mesh was applied to the 'Laminar Flow'-'Solid Mechanics' physics coupling, in order to address the polymeric walls of the channel. The IP-Dip lid, indeed, is deformable, unlike the silicon nitride support, and this causes the partial expansion and elongation of the boundaries

at the liquid-solid interface.

The element size is defined by the fine mesh chosen for the study.

Three different liquids, presented in table A.5, were used for the simulation.

Fluid	Density [kg/m ³]	Dynamic viscosity [mPa.s]
Water	998	1.0
Ethanol	789	1.1
Glycerol	1270	1490

Table A.5. Different fluid properties considered in the FSI analysis.

The resulting deflections in the vertical direction (z-axis) are illustrated in figure A.6(b). In each sample case, deflections can be seen to increase linearly with flow rate. In the same way, with a fixed flow rate, the deformation increases with the liquid viscosity. Glycerol, which has the highest viscosity, produces the largest deflection, followed by ethanol, and finally water. The deformation values obtained from the simulation are specific to a cantilever with dimension indicated in table A.2. If varying the parameters, the magnitude of deformation changes as a function of the stiffness: the stiffer the beam, the lower the deflection.

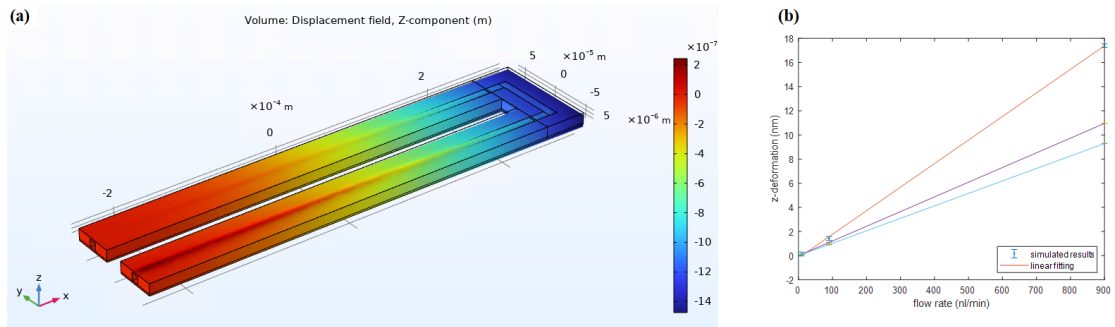


Figure A.6. Vertical deformation of the hybrid cantilever due to the liquid flowing inside the embedded channel. (a) Displacement distribution on the structure when glycerol flows inside the channel with a flow rate of 0.03 nl/min. (b) Vertical displacement of the beam as a function of the flow rate for different fluids: water, ethanol and glycerol.

The obtained lateral deformation (y-axis) is in the order of picometers, and, for this reason, can be considered negligible. In fact, the flow forces acting parallel to the flow direction are not sufficient to produce a considerable lateral deflection of the beam, due to its high stiffness.

The z-deformation of the cantilever affects the resonant behaviour of the device: an external variable stress source is applied to the beam, which behaves as a pre-stressed resonant structure. The effects will be visible on the resonant frequency, which will be shifted with respect to the zero-flow value, and on the Q-factor, which will show a dependence on the flow rate and dynamic viscosity of the liquid flowing inside the channel.

A.5 Resonant frequency dependence on liquid density

The addition of a liquid flowing through the microchannel of the SMR not only causes a static deformation of the beam, but also has an impact on the dynamic behaviour of the device. In fact, the resonant frequency of SMRs is related to the mass added by the liquid, and thus to the liquid density.

The relationship between resonant frequency and liquid density is expressed by the equation A.8.

$$\rho = k \frac{A}{f_n^2} - B \quad (\text{A.8})$$

where f_n is the eigenfrequency at the mode number n , A and B are numerical constants, k is the stiffness of the beam, and it is a function of its geometrical and mechanical properties, i.e., Young's modulus, moment of inertia, length of the beam and support conditions.

A linear relationship between liquid density and eigenfrequency occurs if cantilever stiffness is considered constant. In this case, an increase in liquid density produces a negative shift in resonant frequency.

To simulate the impact of the liquid density on the resonant frequency of the device, the Acoustics and Structural Mechanics modules from COMSOL have been used. These two modules have been linked by an Aeroacoustic-Structure Boundary Multiphysics tool, and then an Eigenfrequency study has been performed while changing the fluid properties [5].

The design employed in the FEM analysis is the same as that shown in figure A.6(a), with the only difference being that in this case only half model is simulated and symmetry conditions are exploited. By so doing, a strong reduction of the computational time is obtained.

'Linearized Navier-Stokes, Frequency Domain' interface has been selected to simulate fluid physics, thus enabling a detailed analysis of the flow influence on the acoustic field in the system. 'Solid Mechanics' interface, instead, has been applied to the cantilever body. Interaction between fluid and solid domain has been modelled by means of stresses exerted by the fluid on the channel walls. The contact surfaces between fluid and solid have been selected and a force per unit of surface has been applied on them. This force is defined in COMSOL by equation A.9 [5].

$$\left\{ \begin{array}{l} T_{stress,x} = lnsf.T_stress_tensorxx * lnsf.nxmesh + \\ \quad + lnsf.T_stress_tensoryx * lnsf.nymesh + \\ \quad + lnsf.T_stress_tensorzx * lnsf.nzmesh \\ \\ T_{stress,y} = lnsf.T_stress_tensorxy * lnsf.nxmesh + \\ \quad + lnsf.T_stress_tensoryy * lnsf.nymesh + \\ \quad + lnsf.T_stress_tensorzy * lnsf.nzmesh \\ \\ T_{stress,z} = lnsf.T_stress_tensorxz * lnsf.nxmesh + \\ \quad + lnsf.T_stress_tensoryz * lnsf.nymesh + \\ \quad + lnsf.T_stress_tensorzz * lnsf.nzmesh \end{array} \right. \quad (\text{A.9})$$

Liquids used for the calculations and their mechanical properties are listed in table A.5. The resulting values are illustrated in graph A.7.

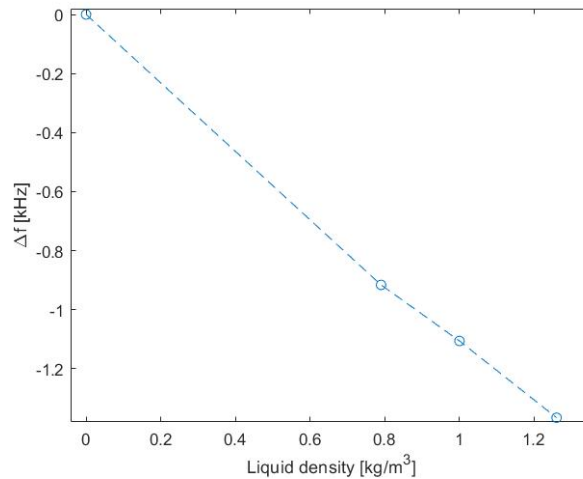


Figure A.7. Resonant frequency of the fundamental mode as a function of the liquid density.

As expected, the greatest shift in resonant frequency with respect to that of a cantilever with an empty channel corresponds to glycerol, which has the highest density; while ethanol, which is characterised by a low density, produces the least shift.

A.6 Energy dissipation in water-filled resonators

As mentioned above, the neutral axis of the beam does not coincide with the centre of the fluidic channel due to the different Young's modulus of silicon nitride and IP-Dip. This entails a pumping mechanism of the fluid into and out of the reservoirs during beam oscillation, causing an increase in energy dissipation and a decrease in the quality factor.

A preliminary theoretical analysis has been carried out to predict the behaviour of the device in the two limit cases of incompressible and compressible flow. Then, an Eigenfrequency study in COMSOL has been performed exploiting the model illustrated in section A.5. It does not take into account the structural damping of the device, but only the fluid dissipation mechanisms, thus enabling the study of the effect of the fluid on the Q-factor of the device.

A.6.1 Theoretical analysis: incompressible and compressible flow

The simplified model of the multi-layered beam described in section A.2.1 was considered in the theoretical analysis.

As a first step, the off-axis channel placement has been calculated for two different sizes corresponding to the worst (Device A) and the best case (Device B) in terms of distance from the neutral axis and resonant frequency. The parameters used for the calculations are listed in table A.6.

Parameter	Device A	Device B
L [μm]	250	500
b_{cant} [μm]	30	50
b_{fluid} [μm]	10	10
h_{cant} [μm]	9	9
h_{fluid} [μm]	5	5

Table A.6. Parameters used to study the effect of the off-axis channel placement on the energy dissipation. L is the length, b is the width and h is the height.

The position of the mid-point of the channel with respect to the bottom of the beam is $z_c = 4.5 \mu\text{m}$; while the distance of the neutral axis from the bottom of the beam can be calculated from equation A.4. The obtained results are: $z_{0,min} = 1.185$ (1.103) and $z_{0,max} = 1.220$ (1.123). From these values one can derive the normalized off-axis placement \overline{Z}_0 for the two cases: $\overline{Z}_{0,min} = 0.656$ (0.6754) and $\overline{Z}_{0,max} = 0.663$ (0.6794).

The effect of Poisson's ratio is also taken into account and translated into an equivalent off-axis channel placement for the two limit cases: $Z_{eff,min} = 0.269$ (0.251) and $Z_{eff,max} = 0.306$ (0.253). Since the cantilever is a multilayer beam, the Poisson's ratio used in calculations is an average value between silicon nitride and polymer.

Based on these results, the limiting case of incompressible flow ($\alpha \rightarrow 0$) has been examined at this early stage.

The normalized quality factor $F(\beta)$ describing the behaviour of the resonator under low-compressibility conditions is given by equation A.10 [6]:

$$F(\beta) = \begin{cases} \frac{38.73\beta}{\beta^2 + 564.6\overline{Z}_0^2(1 + \frac{\beta^2}{8400})} & \beta \rightarrow 0 \\ \frac{\sqrt{\beta}}{6.573 + 1.718\overline{Z}_0^2} & \beta \rightarrow \infty \end{cases} \quad (\text{A.10})$$

Considering water as fluid flowing inside the embedded channel, the maximum and minimum β values are respectively $\beta_{min} = 0.4$ and $\beta_{max} = 1.5$.

From the graph in figure A.8(a), it is possible to define the operating range of the device and the corresponding value of $F(\beta)$. The Q-factor obtained from $F(\beta) \approx 2.5$ is equal to 5000 for Device A and 365000 for Device B.

A second theoretical analysis has been carried out including the effects of compressibility ($\alpha > 0$) on energy dissipation.

In order to simplify the study, a qualitative analysis based on the results obtained by Sader [6] has been performed. In particular, the graph in figure A.8(b) has been taken as a reference to obtain the value of $F(\beta)$ for the two studied devices. The plot shows the behaviour of the normalized quality factor $F(\beta)$ as a function of β for $\gamma = 0.01$. The parameter γ is defined as the normalised wavenumber and is given by:

$$\gamma = \left(\frac{\omega L}{c} \right)^2 \quad (\text{A.11})$$

where ω is the angular frequency, L is the cantilever length, and c is the speed of sound of the liquid inside the channel.

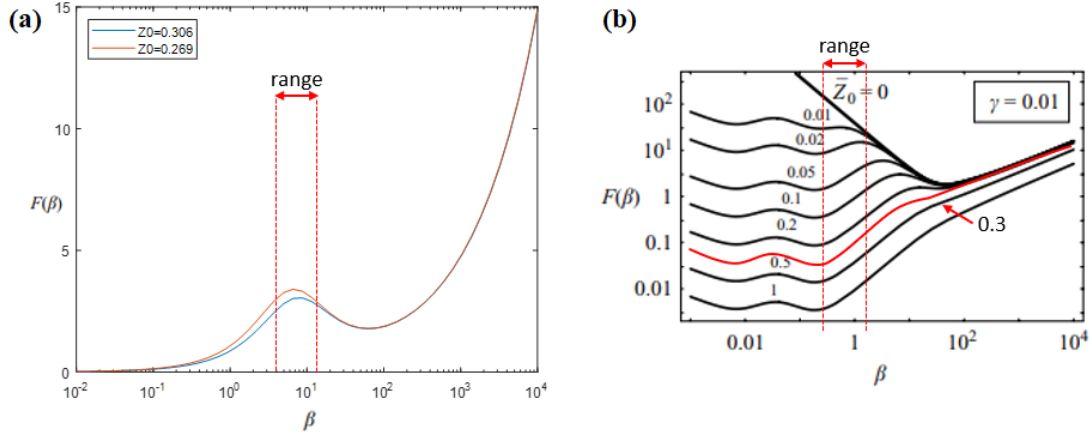


Figure A.8. Normalized frequency as a function of β for the worst and best off-axis channel placement in case of (a) incompressible and (b) compressible flow [6].

As shown in the figure, the quality factor behaves like the incompressible case for large β , while it exhibits small oscillations in magnitude as β decreases.

Within the range of interest ($0.4 < \beta < 1.5$), $F(\beta)$ has a maximum value of 0.05 and a minimum value of 0.1. However, these values refer to a γ two orders of magnitude greater than those in our case of study. In order to derive the correct values, it is necessary to shift the graph downwards, since $F(\beta)$ is directly proportional to the normalised wavenumber [6]. The resulting values for Device A and B are respectively 1.67×10^{-4} and 1×10^{-3} , and the calculated Q-factor are 21.89 and 24.37.

The results obtained in the incompressible and compressible case differ by several orders of magnitude, and this is due to the large impact that compressibility has on energy dissipation in the case of off-axis displacement. Nevertheless, considering the reduced compressibility value of the hybrid device ($\alpha = \lambda / \beta \approx 10^{-4}$), compressibility may not play a key role and a quality factor greater than that of compressible flow may be measured during experiments.

A.6.2 FEM simulations

The model presented in the previous section (A.5) allows rapid simulation of a complex device thanks to the symmetry conditions. The impact of the different mechanical properties of the materials composing the multilayer beam, i.e., Poisson's ratio and Young's modulus, is taken into account by the two-way coupling.

The result of the Eigenfrequency study is a complex eigenfrequency $\tilde{f} = -\frac{\lambda}{2\pi j}$, where the complex eigenvalue λ is defined as $-\delta + j\omega$: the imaginary part ω represents the eigenfrequency

and the real part δ is responsible for damping.

From this numerical result, it is possible to derive the quality factor as:

$$Q = \frac{\omega}{2\delta} \quad (\text{A.12})$$

It should be noted that this definition of Q is slightly different from the one proposed by Sader [6] and takes into account all the dissipative mechanisms within the fluid, e.g., temperature dependence. Moreover, a distinction between compressible and incompressible cases can no longer be made, since the two flows are now assessed as one; therefore, a comparison between numerical and theoretical results should be done carefully [5].

For the Eigenfrequency study, the two limit cases already theoretically analysed (Device A and Device B) are simulated (see table A.6). The embedded channel of the SMR is filled with water, since it is the liquid that will be used for most of the experiments.

The resonant frequency of the device with an empty channel and the numerical results for a water-filled channel are shown in table A.7.

	Device A	Device B
f_{empty} [kHz]	60.55	16.10
f_{water} [kHz]	59.90	15.61
$F(\beta)$	0.008	0.013
Q	460.74	774.87

Table A.7. Numerical results for the fundamental mode.

As predicted by the theoretical analysis, the impact of the liquid on the Q-factor is considerable and strongly limits the performance of the device in terms of sensitivity. However, the results are better than those predicted by the theoretical analysis with compressible flow and quality factor of around 500 can still be achieved.

A.7 Intrinsic dissipation in multilayer resonators

Intrinsic damping is one of the most relevant contributions to the Q-factor of resonant devices. It is related to the geometrical, thermal and mechanical parameters of the beam. In the case of a multilayer structure, each material composing the beam will be characterized by its intrinsic damping. In COMSOL, intrinsic damping of a material can be expressed by the loss coefficient (η). Silicon nitride, like other ceramic materials, has a low loss coefficient, in the order of 10^{-5} ; IP-Dip polymer, instead, has higher η . In polymers, energy dissipation is mainly due to the slippage of the polymeric chains; this entails that the fewer the cross-links between the chains, the greater the losses. Cross-linking is in turn related to the Young's modulus (Y) of the material. It follows that, to a first approximation, the loss coefficient can be traced back to Y by equation A.13 [7].

$$\eta = \frac{4 \times 10^{-2}}{Y} \quad \text{with } Y \text{ in GPa} \quad (\text{A.13})$$

The calculated η for IP-Dip is 0.016.

The huge difference between the loss coefficients of the two materials also indicates a substantial gap between the energy dissipated in each layer. The intrinsic damping in IP-Dip is expected to be three order of magnitude higher than that in silicon nitride.

A two-layered doubly clamped beam with an IP-Dip variable thickness has been simulated. The thickness and the width of the silicon nitride layer were fixed at $2 \mu\text{m}$ and $50 \mu\text{m}$, respectively; while its length ranged from $250 \mu\text{m}$ to $500 \mu\text{m}$. The thickness of the IP-Dip layer, which fully covered the supporting beam, was varied in the range $1 - 10 \mu\text{m}$.

An Eigenfrequency study has been performed to investigate the impact of the polymer layer printed on top of the ceramic resonator. A constant loss factor of 0.016 was included through the Damping subnode under the IP-Dip material model. Although the loss factor usually has some frequency dependency, this dependence was not incorporated in this frequency-response analysis to reduce the complexity of the study. Intrinsic losses were also considered for the SiN layer by introducing a loss factor in the SiN material model. It has been calculated as $1/Q$ from the measured quality factors listed in table C.3.

The behaviour of Q as a function of the thickness of the polymer layer for various beam lengths is illustrated in figure A.9.

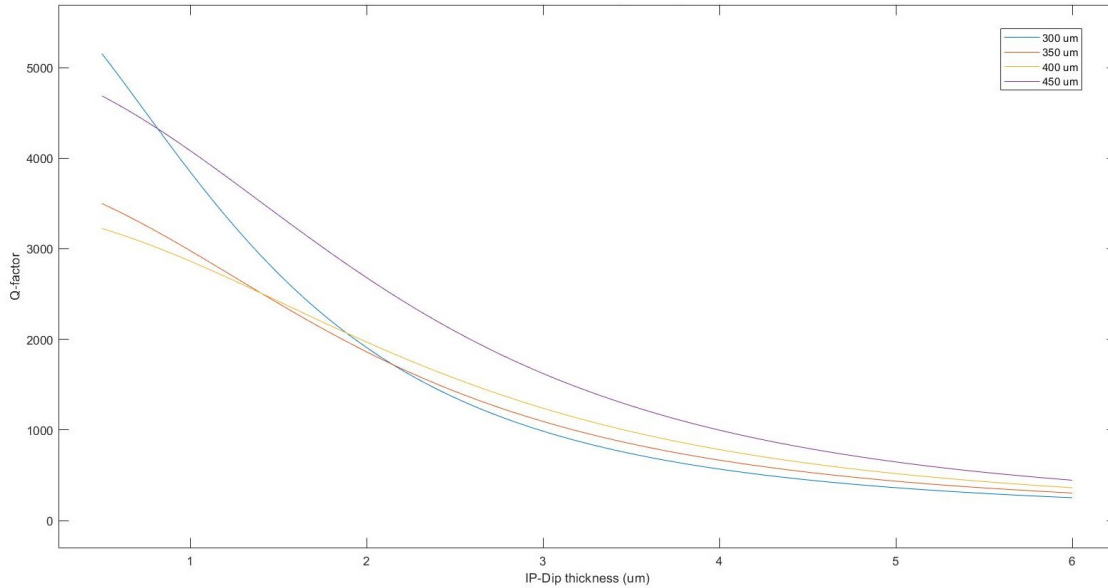


Figure A.9. Quality factor vs IP-Dip thickness for different beam lengths.

As expected, intrinsic dissipation in the polymer layer causes a reduction of the overall quality factor of the hybrid resonator, which decreases with increasing IP-Dip thickness. For small thicknesses, intrinsic losses in silicon nitride also affect the Q -factor; as the IP-Dip thickness increases, the SiN impact becomes negligible and the effect of intrinsic losses in the polymer turns out to be more consistent.

Appendix B

Fabrication process

The objective of the microfabrication process was to realise suspended microchannel resonators so as to enable the study of the frequency behaviour of clamped and clamped-clamped beams and the adhesion of the polymeric printed lid. In this regard, several suspended structures with different length and width have been created.

The fabrication of the hybrid structures has been carried out in two different laboratories:

- **Else Kooi Lab (EKL):** all the semiconductor manufacturing steps on silicon-based materials have been performed in the EKL cleanroom. The supporting cantilevers and bridges in silicon nitride have been realised with typical semiconductor processes, including photolithography, low-pressure chemical vapor deposition (LPCVD), and KOH etching.
- **Precision and Microsystems Engineering (PME) laboratory:** the 3D printing of the embedded channels made of IP-Dip has been performed in the PME lab, where the machine for the two-photon polymerization is located. The printing of the fluidic interface has been done in the same lab.

B.1 Photolithographic masks

As a preliminary step, the photolithographic mask has been designed and printed. Foil mask was preferred to traditional chromium masks, more expensive and with higher resolution, in order to reduce delivery times and costs. This flexible film photomask consists of a 0.18 mm polyester PET base with a soft photographic emulsion gel, which turns black when exposed and developed. The use of a foil mask was possible since the minimum feature size (10 μm) is greater than the maximum mask resolution (5 μm lines). The darkfield mask design is shown in figure B.1.

The lateral features are the alignment marks: they are pink for the zero-layer and blue for the first layer.

The upper part of the wafer is filled with cantilevers, while the bottom part with bridges. The dies have a dimension of 3 mm x 3 mm and are surrounded by wide trenches to enable the manual release of the chips from the wafer. Each die contains one suspended beam, i.e., cantilever or bridge, with a specific width. There are three different widths on the wafer: 30 μm , 40 μm and 50 μm . The length of the structure varies from 250 μm to 500 μm , with a step of 50 μm .

A detailed image of the dies with cantilevers and bridges is shown in figure B.2.

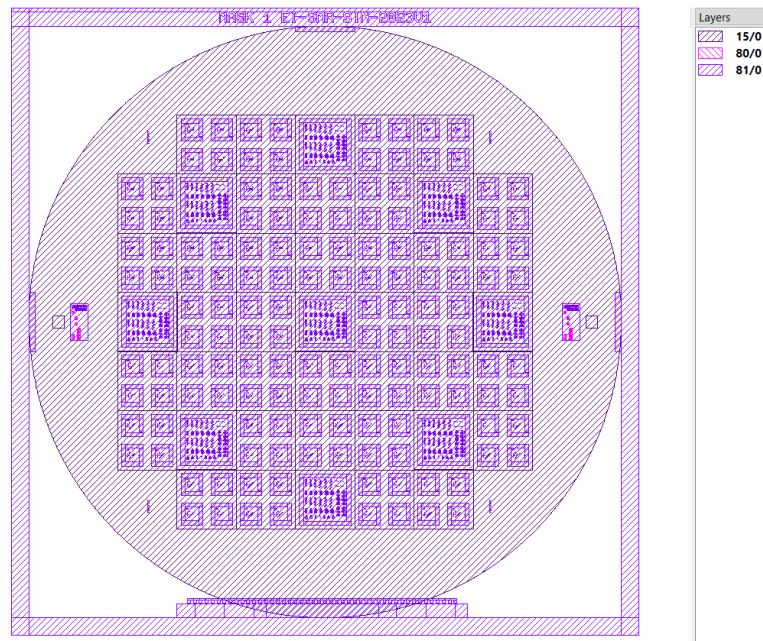


Figure B.1. Mask design showing location and area of the chips containing the structures to be patterned in the silicon nitride layer. Image from k-layout.

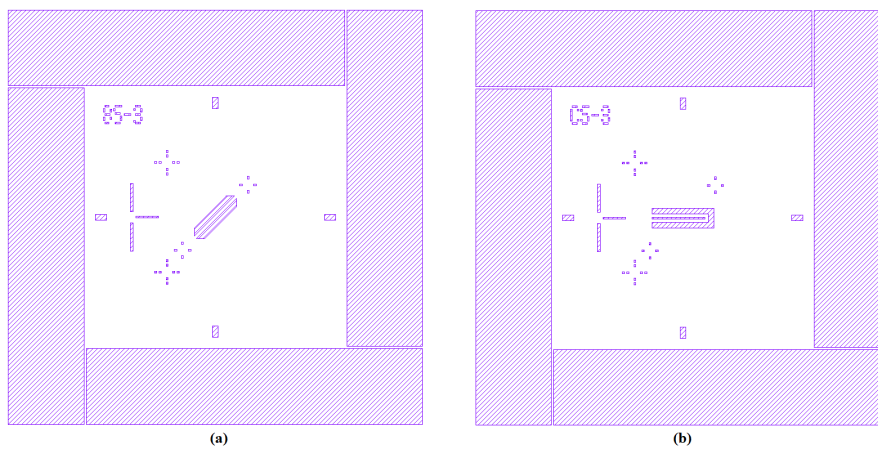


Figure B.2. Darkfield mask design showing (a) bridges and (b) cantilevers of $500\ \mu\text{m}$ length and $30\ \mu\text{m}$ width. Image from k-layout.

From the figure, it is clear that the suspended structure is patterned in the central area of the die. On the upper left corner, a label is placed to indicate the type of beam, bridge or cantilever, and its size in terms of length and width. Alignment marks are designed on the four sides of the frame to easily locate the centre of the beam during the printing step. Four crosses, two larger ones placed vertically for cantilevers and two smaller ones placed diagonally for bridges, are

designed as alignment marks to create the connection with the fluidic interface: two holes with a diameter of 50 μm will be drilled in each die at crosses to connect the chip to the external supply on the wafer backside, and two large domes will be printed on the wafer frontside to flow the liquid from the inlet to the outlet through the embedded microchannel.

In addition to these standard dies, nine dies with test structures have been designed (figure B.3).

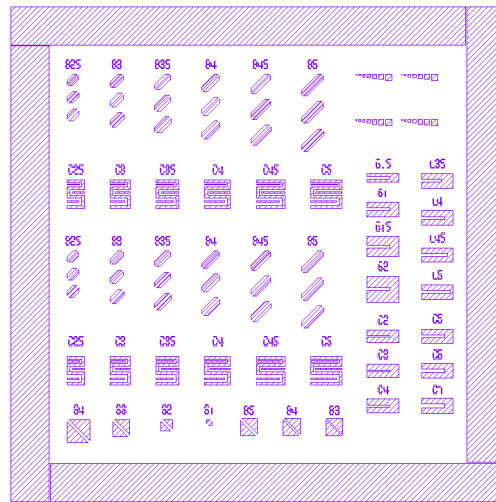


Figure B.3. Darkfield mask design showing test structures. Image from k-layout.

Test dies contain the following features:

- bridges and cantilevers with several widths and lengths to be used for printing tests on suspended beams;
- test structures to measure the selectivity of the RIE, the vertical etch rate of silicon nitride and the horizontal etch rate of silicon;
- empty space for any adhesion test on the silicon nitride substrate.

B.2 Cleanroom steps for silicon nitride structures

The process flow executed in the EKL cleanroom is shown in figure B.4.

The substrate is a n-doped single-side polished silicon (100) wafer of 10 cm diameter and $525 \pm 15 \mu\text{m}$ thickness (fig. B.4(a)). A 2 μm thick Si-rich silicon nitride layer has been deposited by low-stress LPCVD on the silicon substrate (fig. B.4(b)). The intrinsic stress of the deposited layer was measured on a test wafer before patterning the suspended structures: the deformation of the bare Si substrate was measured before LPCVD, then the backside silicon nitride layer deposited by LPCVD was removed by RIE, and finally, the deformation of the substrate has been measured again to derive the stress value. A value of 237 GPa confirmed the low-stress deposition and allowed the realisation of straight beams as supporting structures for the polymeric channels. Anisotropic RIE has been performed to etch the silicon nitride layer (fig. B.4(c)). Subsequent KOH etching step enabled the release of the structured and defined the final devices (fig. B.4(d)).

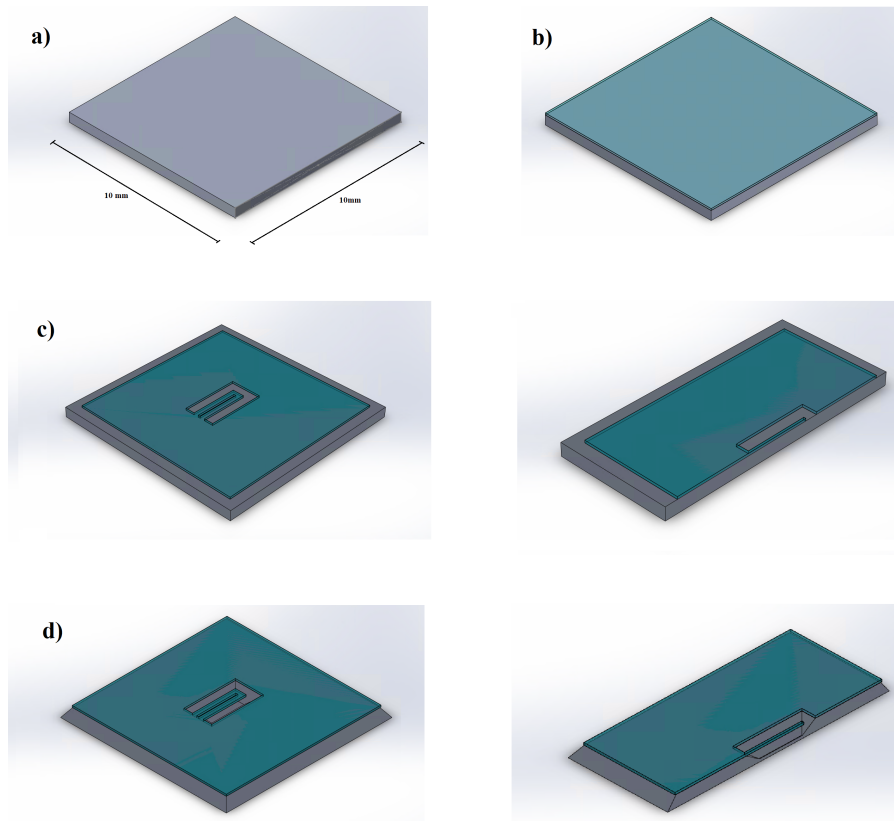


Figure B.4. Flow chart of the cleanroom fabrication process: (a) cleaning of Si<100> substrate, (b) deposition of low-stress silicon nitride by LPCVD, (c) RIE of silicon nitride to create the suspended structures and scribelines, (d) release of the bridges and cantilevers by KOH etching and wafer cleaning.

In the following sections, the steps and the related issues will be explained in detail.

B.2.1 Low-stress LPCVD of silicon nitride

In order to obtain stiff and straight beams as supporting structures for the polymeric channels, low-stress LPCVD has been performed to deposit 2 μm thick silicon nitride layer on the silicon substrate (fig. B.4(b)).

LPCVD is a type of chemical vapor deposition (CVD), a process that allows to deposit thin films starting from gaseous precursors. An energy source breaks reactant gases into reactive species that react on a surface producing a solid phase material. The resulting deposited film will be metallic, semiconducting, or insulating depending on the precursors. There are several types of CVD differing by operating conditions, i.e., temperature and pressure, precursor type, and energy source. Each and every CVD process consists of the same following steps:

- generation of vapor or providing of vapor sources;
- diffusion of precursor molecules to the solid surface;

- adsorption of precursors and diffusion through the surface;
- decomposition and incorporation into solid films (nucleation);
- desorption of volatile products.

The main used CVD are low-pressure CVDs (LPCVD) and plasma-enhanced CVD (PECVD).

The low pressure distinguishes LPCVD from other CVD processes: reactions occur in moderate vacuum conditions (5-250 Pa) at high temperatures with a low deposition rate. As a result, the deposited films exhibit high uniformity and homogeneity. Moreover, it also guarantees high purity of the deposited layer and improves its internal structure.

On the other hand, PECVD occurs at low temperatures and is characterised by the use of plasma. The plasma is created in the deposition chamber by radio frequency (RF) or direct current (DC) discharge between two electrodes and induces the dissociation of precursor molecules. This dissociation deposits the desired molecules onto the substrate with a high deposition rate. The low temperature that distinguishes the process makes it suitable for the last fabrication steps, where the high temperature would result in unwanted diffusion of dopants and/or metal melting. However, the quality of films obtained through PECVD is lower than that of LPCVD due to chemical contamination, and the non-uniformity in thickness and composition is fairly large [8]. This latter condition has a considerable impact on the specific application field of mechanical sensors like resonators, in which a poor uniformity in thickness as well as in composition of the deposited layer will result in an unacceptable non-uniformity in sensor sensitivity across a wafer. Added to this is the non-uniformity in the residual stress across the wafer, which results in sensors with variable mechanical properties. Furthermore, taking into account the material to be deposited, i.e., silicon nitride, the Young's modulus of Si-rich Si_xN_y films deposited by PECVD is lower than the one formed by LPCVD [9].

All these considerations make the LPCVD a more suitable CVD process for the realisation of resonant beams.

Once the type of CVD to be used has been defined, a crucial parameter that must be taken into account is the residual stress of the deposited silicon nitride film: it should be low and uniform enough not to deform the cantilever or even break the bridges. This residual stress is caused by the dissociation of Si-H and N-H bonds and the subsequent rearranging of the dangling bonds into Si-N bonds that induce shrinkage of the bulk of the layer during and after deposition [10].

The parameters that control the stress are temperature, pressure and DCS: NH_3 gas flow ratio [8]. In particular, stress decreases with increasing temperature or decreasing of pressure, and increases with decreasing DCS: NH_3 gas flow ratio [11] (fig. B.5(a)).

Moreover, depending on the gas flow ratio NH_3/DCS , the stress changes from compressive to tensile. As the flow ratio NH_3/DCS decreases, the N/Si ratio of the deposited film also decreases and silicon-rich silicon nitride is formed. This means that fewer Si-N bonds are created and stress is less tensile (more compressive) [11]. However, continuing to reduce the ratio, the structure is gradually turned into nitrogen-doped silicon. This entails the transition from compressive to tensile stress.

The gas flow ratio NH_3/DCS has also an impact on the deposition rate: a decrease in the gaseous ratio produces an increase in the deposition rate (fig. B.5(b)).

Taking into account the effect of the deposition parameters, i.e., temperature, pressure, and gas flow rate, on the deposition rate and intrinsic stress, specific process conditions have been selected for the low-stress LPCVD. Their values are listed in table B.1.

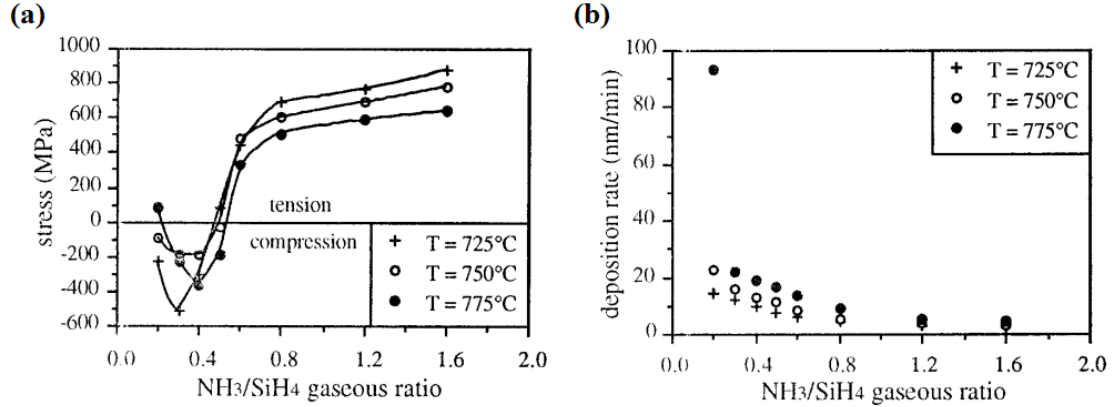


Figure B.5. (a) Residual stress and (a) deposition rate as functions of the gaseous ratio for different temperatures [8]. In this case NH₃/DCS gaseous mixture has been substituted by NH₃/SiH₄.

Gasses and flows	Pressure [mTorr]	Temperature [°C]
NH ₃ /SiH ₂ Cl ₂ = 85/315 sccm = 0.27	150	846

Table B.1. Process conditions for low-stress LPCVD of silicon-rich silicon nitride film.

The obtained silicon nitride layer has a thickness of $1998 \text{ nm} \pm 8 \text{ nm}$ and a refractive index n of 2.21 assessed at a 633 nm wavelength. Both film thickness and refractive index have been measured by ellipsometry. It has been proved that the index of refraction is a valid indicator of the Si content in Si_xN_y films [12]: a value of 0.75 (for a wavelength of 633 nm) is attributed to stoichiometric Si₃N₄, while an increase in the refractive index starting from that value corresponds to an increase in the Si/N ratio [12, 13]. This means that the obtained refractive index of 2.21 ($\lambda = 633 \text{ nm}$) can be associated with a silicon-rich silicon nitride film, as expected.

The measured value of the index of refraction also ensures low intrinsic stress of the deposited layer, since the refractive index for optimal uniformity and minimum stress is in the region of 2.20-2.25 [13].

An average tensile stress of 237 MPa has been obtained by measurement of the wafer curvature ($1/R$) before and after the LPCVD deposition. The measurement of the substrate curvature after LPCVD has been performed after backside etching of the SiN layer. The average stress σ of the deposited films has been derived from Stoney's formula (eq. B.1).

$$\sigma = -\frac{1}{6R} \frac{E}{(1-\nu)} \frac{D^2}{d} \quad (\text{B.1})$$

where E is the Young's modulus, ν is the Poisson's ratio, D is the substrate thickness, and d is the film thickness.

An intrinsic stress value in the range 0-200 MPa can be considered low enough to enable the fabrication of straight beams. This means that the measured value is at the limit of the acceptable

stress range and can be suitable for the supporting SiN beams to be realised in this project.

B.2.2 Reactive ion etching of silicon nitride

The deposited silicon nitride layer has been patterned via photolithography and a subsequent dry etching step, in order to obtain the beams and the scribelines separating individual chips (fig. B.4(c)). The result of RIE is visible in figure B.6.

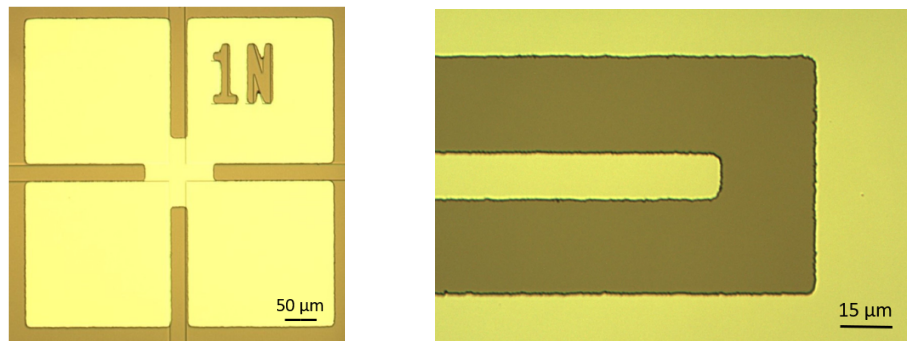


Figure B.6. Alignment marks (left) and detail of a cantilever (right) etched into SiN.

As shown in the image, the corners are rounded and the profiles have a certain roughness due to the low resolution of the foil mask and the proximity exposure during the lithographic step. The proximity exposure method was preferred over soft or hard contact exposure to avoid damaging the foil mask. Even though these latter allow to reach better resolution, the contact between the lithography mask and wafer could damage the black emulsion and make the mask unusable for future exposure. With proximity exposure, instead, a micrometric gap is brought between the mask and wafer, which reduces the resolution, but increases the mask's lifetime.

B.2.3 KOH etching for beam release

The release of the cantilever has been performed through convex corner etching in 30% aqueous KOH etchant at 85°C (fig. B.4(d)). To also allow the release of the bridges through undercutting, they were designed on the mask rotated by 45° with respect to the primary flat of the wafer.

The lateral undercut etch process is self-limiting; nevertheless, the etching was stopped once the longest cantilevers, i.e., 500 μm length, were fully undercut in order to reduce the lateral over-etching of the cavity.

The lateral over-etching is about 4.3 μm, which corresponds to 1.72% of the length of the shortest beam. As a consequence, we can neglect the effect of over-etching on the resonant frequency.

The released beams are shown in figure B.7. As illustrated in the images, the obtained beams are straight. This means that the intrinsic stress of the Si-rich silicon nitride layer is low and uniform enough not to deform the devices.

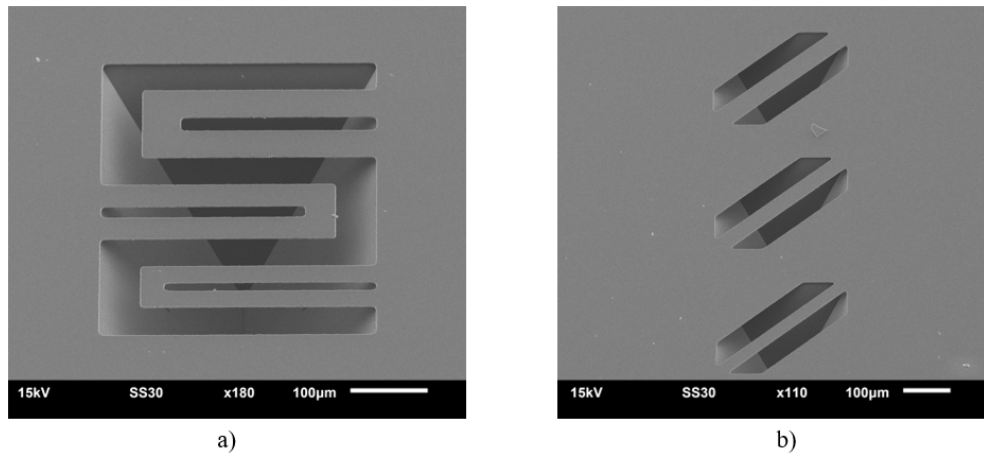


Figure B.7. SEM picture of released (a) cantilevers and (b) bridges with a tilting angle of 45° .

B.2.4 Aluminum-Silicon(1%) sputtering and wafer cleaving

In order to increase the reflectivity of the suspended structure a 30 nm thick layer of AlSi(1%) has been sputtered on the whole wafer. This layer has no significant impact on the performance of the devices in terms of resonant frequency and allows the TPP-printer to correctly find the interface while printing on the transparent silicon nitride beams.

The last step performed in the EKL cleanroom is wafer dicing: the wafer has been divided into 3 mm x 3 mm dies, each of them containing a resonating beam. The dicing process involved breaking the wafer along the previously etched scribelines. Scribelines, indeed, created an intentional weak point in the substrate in order to force it to break at only that location.

Since the used substrate is silicon, which is a crystalline material, when cleaving force is applied to the edge of a die or of the wafer, it will break following the crystal plane. This allows to release more dies at the same time.

The cleaving method is not extremely precise, especially when the die size is a few millimeters, and could cause the breaking of some dies if the cleaving force is not exerted at the right place. But it is very simple and fast and does not necessarily require the use of special tools: sharp tweezers and a diamond wafer-cutting pen are sufficient.

B.3 3D printing of IP-Dip channels via two-photon polymerization

The process flow executed in the PME cleanroom is shown in figure B.8.

The fluidic connection between the embedded channel and the fluidic interface is realised by laser hole drilling of the substrate: two holes for the inlet and outlet of the microchannel are created on both sides of the bridge or at the fixed end of the cantilever (fig. B.8(a)). Then the polymeric lid with the buried channel is printed by two-photon polymerization on top of the beam, as illustrated in figure B.8(b).

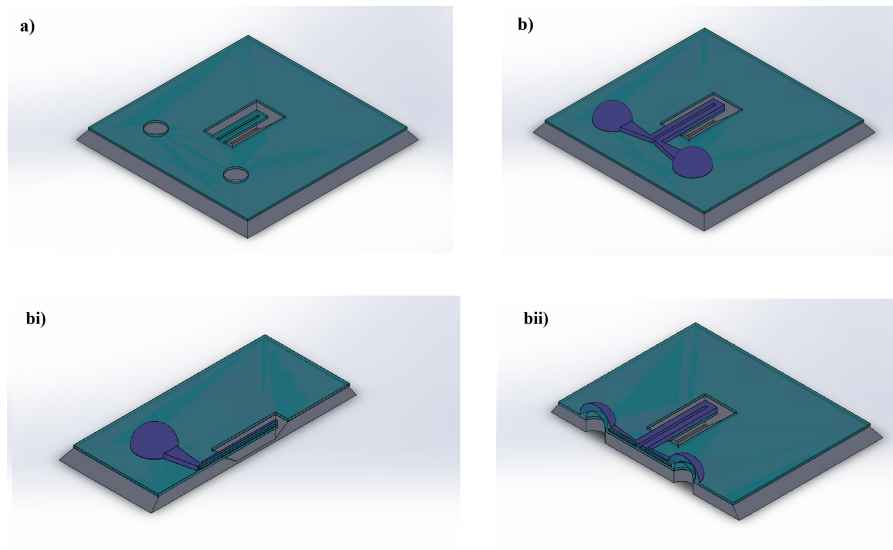


Figure B.8. Flow chart of the fabrication process: (a) laser drilling of holes in the silicon wafer for the connection with the fluidic interface, (b) 3D printing by two-photon polymerization of the polymeric lid with the embedded channel, (ci) and (cii) sections of the chip showing the hollowed structure.

In order to reduce the fluidic resistance, the connection from the dome to the beam is realised by gradually decreasing the channel cross-section (fig. B.8(bi) and (bii)).

B.3.1 TPP-printing on SiN beams

The dies containing SiN resonators need to be fixed to the TPP-holder for printing. It has been fabricated so as to hold 25 mm x 25 mm dies, which have to be taped to the edges. Since the size of Si dies is smaller than the holes in the TPP-holder, 3D-printed adapters have been fabricated to clamp the small dies and fix them to the TPP-holder. The CAD design of the support is shown in figure B.9. DLP 3D printing process is performed to realise the adapters made of 3DM TOUGH clear resin using Micro Plus Hi-Res (EnvisionTEC US LLC, United States).

Once the die is clamped, the IP-Dip liquid resin is carefully placed onto the substrate and the holder is inserted into the Nanoscribe. Before starting the printing process, the interface has to be found manually. The XY stage is moved to the area with the most reflected light, corresponding to the position of the Si die, then the lens is moved down in the Z-direction. When the surface of the die is on focus, the XY stage is moved to find the supporting SiN beam to be printed on. The printing starts from one of the clamped edges of the beam.

The printing of the layer on suspended beams has a duration that ranges from 2 to 10 minutes, depending on bridge length and structure shape; while the printing of the entire structure, including fixed channels and fluidic connections, has an estimated printing time of around 2 hours.

After printing, devices are cleaned from the residues of non-polymerised resin with a developing step. The dies are separated from the adapter and submerged in $\geq 99.5\%$ Propylene glycol monomethyl ether acetate (MilliporeSigma, United States) for 25 minutes, then they are

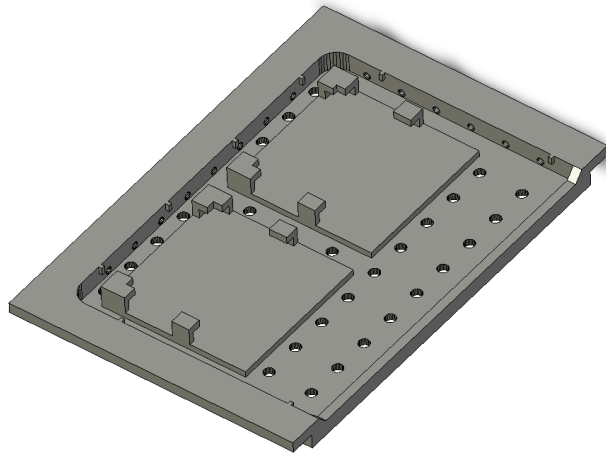


Figure B.9. *Chip holder for the TPP. Two 8x8 mm² dies can be placed into the two dedicated spaces. Then, the holder itself is taped to the Nanoscribe multi-DiLL sample holder.*

submersed into isopropanol for 5 minutes. Drying is carried out using a nitrogen gun with low airflow to prevent resonators from breaking.

Appendix C

Characterisation

C.1 Mechanical characterization

C.1.1 Young's modulus of IP-Dip

In order to measure the Young's modulus of the IP-Dip polymer, a compression test has been performed. An array of twelve pillars has been printed on an AlSi(1%) sputtered substrate (see figure C.1(a)) and a force-displacement curve has been obtained for each structure. The force has been applied in a direction perpendicular to the substrate, as shown in figure C.1(b).

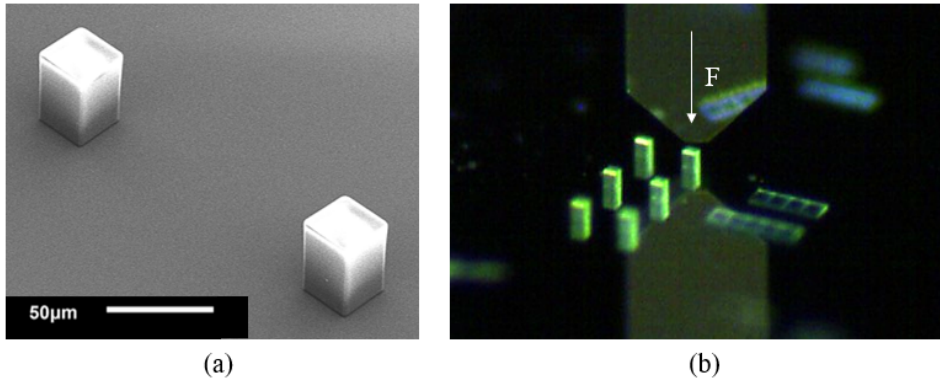


Figure C.1. (a) SEM picture of $35 \mu\text{m} \times 35 \mu\text{m} \times 45 \mu\text{m}$ IP-Dip pillars with a tilting angle of 45° ; (b) compression test.

The Young's modulus has been extracted from the linear region of the curve by using equation C.1.

$$E = \frac{\sigma(\varepsilon)}{\varepsilon} = \frac{FL_0}{A\Delta L} \sigma \quad (\text{C.1})$$

where σ is the stress, ε is the strain, F is the compressive force, L_0 is the initial height of the pillar, ΔL is the height variation and A is the area of the section perpendicular to the applied force.

The same experiment has been carried out on a second array of twelve pillars subjected to 40 min UV-light exposure.

The size of the pillars with and without UV-light exposure has been characterized using a Keyence Digital Microscope VHX-6000. The measured values are listed in table C.1.

Parameter	Nominal value	No exposure	Exposure
Height [μm]	45	43.1 ± 3.0	42.0 ± 2.2
Cross-section [μm^2]	900	849.8 ± 1.9	850.7 ± 2.9

Table C.1. Size of the pillars printed for the compression test.

C.1.2 Adhesion force between polymer and AlSi(1%) surface

The adhesion force of the IP-Dip polymer to the AlSi(1%) substrate has been obtained from a compression test. Two pillars with a different square cross-section have been printed on an AlSi(1%) sputtered substrate (see figure C.2(a)) and a force-displacement curve has been obtained for each structure. The force has been applied in a direction parallel to the substrate, as shown in figure C.2(b).

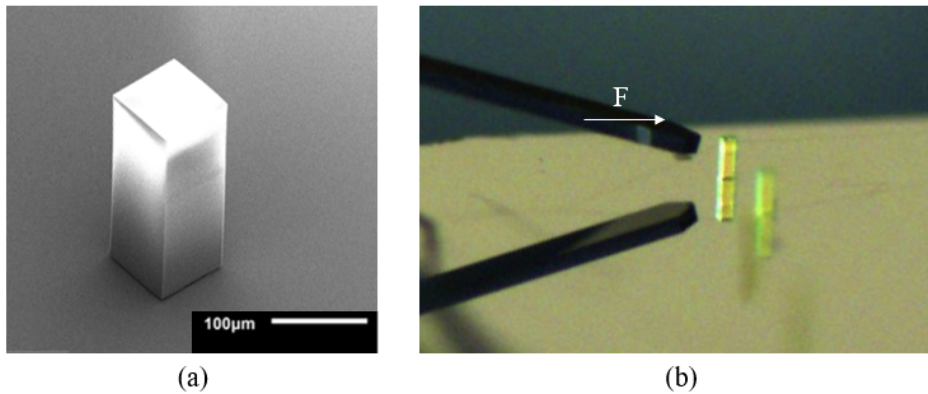


Figure C.2. SEM picture of $80 \mu\text{m} \times 80 \mu\text{m} \times 250 \mu\text{m}$ IP-Dip pillar with a tilting angle of 45° .

The size of the two pillars has been measured using JSM-6010LA SEM (JEOL Ltd.,The Netherlands). The measured values are listed in table C.2.

C.2 Frequency study: resonant frequency and Q-factor measurements

	Parameter	Nominal value	Measured value
Pillar 1	Height [μm]	250	232
	Cross-section [μm^2]	4900	4784
Pillar 2	Height [μm]	250	239
	Cross-section [μm^2]	6400	6141

Table C.2. Size of the pillars printed for the compression test.

Length [μm]	Width [μm]	f_R [kHz]	Q-factor [10^3]
250	30	626.6 ± 3.2	12.2 ± 1.9
	40	617.5 ± 3.2	11.50 ± 0.20
	50	606.8 ± 3.6	11.60 ± 0.21
300	30	498.1 ± 3.4	12.0 ± 1.0
	40	490.5 ± 2.4	12.57 ± 0.11
	50	483.6 ± 3.4	14.77 ± 0.27
350	30	416.2 ± 3.1	9.5 ± 1.6
	40	411.6 ± 2.7	11.17 ± 0.51
	50	405.9 ± 2.9	11.47 ± 0.98
400	30	356.45 ± 0.55	10.8 ± 1.4
	40	353.1 ± 1.9	12.94 ± 0.37
	50	351.69 ± 0.45	14.01 ± 0.67
450	30	309.9 ± 1.7	12.35 ± 0.21
	40	308.5 ± 1.6	9.3 ± 1.2
	50	305.4 ± 2.0	12.34 ± 0.65
500	30	277.4 ± 1.2	11.1 ± 2.4
	40	274.5 ± 1.9	10.3 ± 1.3
	50	271.2 ± 2.2	11.59 ± 0.88

Table C.3. Resonance frequency and Q-factor of the first resonant mode of SiN bridges.

Length [μm]	Width [μm]	f_R [kHz]	Q-factor [10^3]
250	30	45.42 ± 0.18	14.65 ± 0.76
	40	44.48 ± 0.52	19.1 ± 2.8
	50	44.53 ± 0.17	21.47 ± 0.49
300	30	31.86 ± 0.13	22.58 ± 0.10
	40	31.62 ± 0.10	20.3 ± 1.7
	50	31.13 ± 0.15	22.23 ± 0.31
350	30	23.60 ± 0.10	22.72 ± 0.46
	40	24.5 ± 1.1	23.03 ± 0.20
	50	23.13 ± 0.10	23.88 ± 0.46
400	30	18.285 ± 0.035	23.22 ± 0.58
	40	18.150 ± 0.040	20.9 ± 4.1
	50	17.910 ± 0.070	23.990 ± 0.050
450	30	14.525 ± 0.035	23.900 ± 0.020
	40	14.435 ± 0.025	22.9 ± 2.9
	50	14.12 ± 0.12	24.44 ± 0.54
500	30	11.80 ± 0.02	24.62 ± 0.23
	40	11.760 ± 0.010	24.61 ± 0.11
	50	11.620 ± 0.020	24.690 ± 0.010

Table C.4. Resonance frequency and Q-factor of the first resonant mode of SiN cantilevers.

Length [μm]	Width [μm]	f_R [kHz]	Q-factor [10^3]
250	30	618.3 ± 4.0	4.1 ± 1.7
250	40	610.4 ± 3.8	4.9 ± 1.4
250	50	605.98 ± 2.6	5.00 ± 0.88
300	50	486.9 ± 1.1	6.34 ± 0.76
350	50	407.1 ± 2.3	3.9 ± 1.5
400	50	348.8 ± 3.3	3.40 ± 0.70
450	50	305.1 ± 2.6	5.08 ± 0.82
500	50	271.4 ± 2.2	5.95 ± 0.44

Table C.5. Resonance frequency and Q-factor of the first resonant mode of bridges after AlSi(1%) sputtering.

Length [μm]	Width [μm]	f_R [kHz]	Q-factor [10^3]
250	30	45.31 ± 0.11	6.42 ± 0.35
250	40	44.800 ± 0.030	6.30 ± 0.50
250	50	44.12 ± 0.16	6.69 ± 0.43
300	50	31.18 ± 0.14	6.25 ± 0.54
350	50	23.185 ± 0.055	5.79 ± 0.42
400	50	17.950 ± 0.070	5.47 ± 0.67
450	50	14.310 ± 0.060	4.8 ± 1.1
500	50	11.650 ± 0.030	4.48 ± 0.96

Table C.6. Resonance frequency and Q-factor of the first resonant mode of cantilevers after AlSi(1%) sputtering.

Length [μm]	f_{SiN} [kHz]	f_{gold} [kHz]	Q_{SiN} [10^3]	Q_{gold} [10^3]
250	597.4 ± 1.9	589.5 ± 6.5	6.2 ± 2.1	2.66 ± 0.55
300	483.0 ± 2.8	471.9 ± 2.3	17.5 ± 3.0	4.6 ± 1.9
350	403.1 ± 2.0	393.20 ± 0.94	10.5 ± 1.7	0.70 ± 0.12
400	356.45 ± 0.55	-	10.8 ± 1.4	-
450	302.59 ± 0.83	295.22 ± 0.84	9.6 ± 2.1	4.4 ± 1.0
500	269.52 ± 0.58	262.96 ± 0.60	10.9 ± 1.6	6.22 ± 0.73

Table C.7. Resonance frequency and Q-factor of the first resonant mode of bridges of 50 μm width before (*SiN*) and after (*gold*) gold sputtering.

Length [μm]	f_{SiN} [kHz]	f_{gold} [kHz]	Q_{SiN} [10^3]	Q_{gold} [10^3]
250	44.00 ± 0.36	43.02 ± 0.01	20.06 ± 0.82	14.10 ± 0.20

Table C.8. Resonance frequency and Q-factor of the first resonant mode of cantilevers of 50 μm width before (*SiN*) and after (*gold*) gold sputtering.

Length [μm]	f_{par} [kHz]	f_{per} [kHz]	Q_{par} [10^3]	Q_{per} [10^3]
250	-	406.43	-	725.75
300	413.15	334.84	507.40	596.93
350	344.26	-	854.32	-
400	295.41	288.47	451.63	300.81
450	265.75	252.33	1107.20	458.90

Table C.9. Resonance frequency and Q-factor of the first resonant mode of 50 μm width bridges with a continuous IP-Dip layer with parallel (*par*) and perpendicular (*per*) printing direction.

Length [μm]	f_{par} [kHz]	f_{per} [kHz]	Q_{par} [10^3]	Q_{per} [10^3]
250	517.02	506.20	-	-
300	415.09	396.20	-	378.28
350	340.98	-	-	-
400	292.69	-	-	-
450	249.03	247.08	-	265.02
500	227.45	219.42	292.13	385.3

Table C.10. Resonance frequency and Q-factor of the first resonant mode of 50 μm width bridges of two IP-Dip walls with parallel (*par*) and perpendicular (*per*) printing direction.

Length [μm]	f_{par} [kHz]	f_{per} [kHz]	Q_{par} [10^3]	Q_{per} [10^3]
350	341.22	330.18	510.52	226.63
400	278.73	281.64	14.40	348.10
450	243.47	243.86	504.90	409.34
500	215.88	216.06	256.26	329.27

Table C.11. Resonance frequency and Q-factor of the first resonant mode of 50 μm width bridges with two IP-Dip walls and a thin middle layer with parallel (*par*) and perpendicular (*per*) printing direction.

Bibliography

- [1] Xin-Ge Guo, Zai-Fa Zhou, Chao Sun, Wei-Hua Li, and Qing-An Huang. “A Simple Extraction Method of Young’s Modulus for Multilayer Films in MEMS Applications”. In: *Micromachines* 8 (June 2017). DOI: [10.3390/mi8070201](https://doi.org/10.3390/mi8070201) (cit. on p. 61).
- [2] Annalisa De Pastina, Damien Maillard, and Luis Guillermo Villanueva. “Fabrication of suspended microchannel resonators with integrated piezoelectric transduction”. In: *Microelectronic Engineering* 192 (Feb. 2018). DOI: [10.1016/j.mee.2018.02.011](https://doi.org/10.1016/j.mee.2018.02.011) (cit. on p. 64).
- [3] Mostapha Marzban, Muthukumaran Packirisamy, and Javad Dargahi. “Parametric study on fluid structure interaction of a 3D suspended polymeric microfluidics (SPMF3)”. In: *Microsystem Technologies* 24 (June 2018). DOI: [10.1007/s00542-018-3741-5](https://doi.org/10.1007/s00542-018-3741-5) (cit. on pp. 65, 66).
- [4] Ayobami Oseyemi, Ion Stiharu, and Muthukumaran Packirisamy. “Design and parametric study of a tapered polymer-based suspended microfluidic channel for enhanced detection of biofluids and bioparticles”. In: *Microsystem Technologies* (Apr. 2023). DOI: [10.1007/s00542-023-05439-4](https://doi.org/10.1007/s00542-023-05439-4) (cit. on pp. 65, 66).
- [5] Andrea Gerbino. “Energy Dissipation in Suspended Microchannel Resonators: theoretical, numerical and experimental validation”. MA thesis. Sapienza Università di Roma, 2018 (cit. on pp. 68, 72).
- [6] John E. Sader, Thomas P. Burg, and Scott R. Manalis. “Energy dissipation in microfluidic beam resonators”. In: *Journal of Fluid Mechanics* 650 (2010). DOI: [10.1017/S0022112009993521](https://doi.org/10.1017/S0022112009993521) (cit. on pp. 70–72).
- [7] M.F. Ashby. “Overview No. 80: On the engineering properties of materials”. In: *Acta Metallurgica* 37.5 (1989). DOI: [https://doi.org/10.1016/0001-6160\(89\)90158-2](https://doi.org/10.1016/0001-6160(89)90158-2) (cit. on p. 72).
- [8] Han Gardeniers, H.A.C. Tilmans, and C. Visser. “LPCVD silicon-rich silicon nitride films for applications in micromechanics, studied with statistical experimental design*”. In: *Journal of Vacuum Science and Technology A: Vacuum, Surfaces, and Films* 14 (Oct. 1996). DOI: [10.1116/1.580239](https://doi.org/10.1116/1.580239) (cit. on pp. 79, 80).
- [9] Zhenghao Gan, Changzheng Wang, and Zhong Chen. “Material Structure and Mechanical Properties of Silicon Nitride and Silicon Oxynitride Thin Films Deposited by Plasma Enhanced Chemical Vapor Deposition”. In: *Surfaces* 1 (Aug. 2018). DOI: [10.3390/surfaces1010006](https://doi.org/10.3390/surfaces1010006) (cit. on p. 79).

- [10] A.G. Noskov, Evgenii Gorokhov, G.A. Sokolova, E.M. Trukhanov, and S.I. Stenin. "Correlation between stress and structure in chemically vapour deposited silicon nitride films". In: *Thin Solid Films* 162 (Aug. 1988). DOI: [10.1016/0040-6090\(88\)90201-5](https://doi.org/10.1016/0040-6090(88)90201-5) (cit. on p. 79).
- [11] P. Temple-Boyer, Carole Rossi, E. Saint-Etienne, and E. Scheid. "Residual stress in low pressure chemical vapor deposition SiNx films deposited from silane and ammonia". In: *Journal of Vacuum Science and Technology A: Vacuum, Surfaces, and Films* 16 (Aug. 1998). DOI: [10.1116/1.581302](https://doi.org/10.1116/1.581302) (cit. on p. 79).
- [12] Takahiro Makino. "Composition and Structure Control by Source Gas Ratio in LPCVD SiNx". In: *Journal of The Electrochemical Society* 130.2 (Feb. 1983). DOI: [10.1149/1.2119729](https://doi.org/10.1149/1.2119729) (cit. on p. 80).
- [13] James Olson. "Analysis of LPCVD process conditions for the deposition of low stress silicon nitride. Part I: Preliminary LPCVD experiments". In: *Materials Science in Semiconductor Processing - MATER SCI SEMICOND PROCESS* 5 (Feb. 2002). DOI: [10.1016/S1369-8001\(02\)00058-6](https://doi.org/10.1016/S1369-8001(02)00058-6) (cit. on p. 80).